


ADVANCED MASTERS IN STRUCTURAL ANALYSIS
OF MONUMENTS AND HISTORICAL CONSTRUCTIONS

Master's Thesis

John Adamek

Stochastic Micro-modelling of Historic Masonry

University of Minho

Czech Republic | 2019



ADVANCED MASTERS IN STRUCTURAL ANALYSIS
OF MONUMENTS AND HISTORICAL CONSTRUCTIONS

Master's Thesis

John Adamek

Stochastic Micro-modelling of Historic Masonry

Czech Republic | 2019

CZECH TECHNICAL UNIVERSITY IN PRAGUE
Faculty of Civil Engineering
Thákurova 7, 166 29 Prague 6, Czech Republic

MASTER'S THESIS PROPOSAL

study programme: Civil Engineering

study branch: Advanced Masters in Structural Analysis of Monuments and Historical Constructions

academic year: 2018/2019

Student's name and surname: John Adamek

Department: Department of Mechanics

Thesis supervisor: Petr Kabele

Thesis title: Stochastic Micro-modelling of Historic Masonry

Thesis title in English see above

Framework content: The objective of this thesis was to determine the overall compressive strength of St. Ann's Church, part of the Broumov Group of Churches in the Czech Republic. Based on a statistical analysis of the geometry of the irregular masonry walls, a multi-scale modelling approach will be utilized to determine the homogenized strength and stiffness of the walls to be used in a structural-scale analysis of the church.

Assignment date: 1/04/2019 Submission date: 8/09/2019

If the student fails to submit the Master's thesis on time, they are obliged to justify this fact in advance in writing, if this request (submitted through the Student Registrar) is granted by the Dean, the Dean will assign the student a substitute date for holding the final graduation examination (2 attempts for FGE remain). If this fact is not appropriately excused or if the request is not granted by the Dean, the Dean will assign the student a date for retaking the final graduation examination, FGE can be retaken only once. (Study and Examination Code, Art 22, Par 3, 4.)

The student takes notice of the obligation of working out the Master's thesis on their own, without any outside help, except for consultation. The list of references, other sources and names of consultants must be included in the Master's thesis.

....
Master's thesis supervisor Head of department

Date of Master's thesis proposal take over: July 2019

.....
Student

DECLARATION

Name:	John Adamek
Email:	Adamek2192@gmail.com
Title of the Msc Dissertation:	Stochastic Micro-modelling of Historic Masonry
Supervisors(s):	Prof. Ing. Petr Kabele, Ph.D.
Year:	2018/2019

I hereby declare that all information in this document has been obtained and presented in accordance with academic rules and ethical conduct. I also declare that, as required by these rules and conduct, I have fully cited and referenced all material and results that are not original to this work.

I hereby declare that the MSc Consortium responsible for the Advanced Masters in Structural Analysis of Monuments and Historical Constructions is allowed to store and make available electronically the present MSc. Dissertation.

University:	Czech Technical University in Prague
Date:	08/07/2019
Signature:	

This page is left blank on purpose.

To my friends, family and faculty.

This page is left blank on purpose.

ACKNOWLEDGEMENTS

First and foremost, I would like to thank my supervisor, Prof. Ing. Petr Kabele Ph.D., whose expertise, commitment, guidance, and enthusiasm was integral to the development of the work here at the Czech Technical University in Prague.

Furthermore, I would like to thank the following people, without which the completion of this work was not possible:

- Prof. Ing. Pavel Kuklík CSc for his organization of the wonderful site visit and his knowledge on the Broumov Group of Churches that sparked the further development of the work.
- Ing. Zuzana Slížková Ph.D., Ing. Lucie Jurkovska, and Dana Janotová for the guidance and time dedicated to the testing of the material samples at the Institute of Theoretical and Applied Mechanics of the Academy of Sciences of the Czech Republic (ITAM) laboratory.
- Červenka Consulting for the software and consultation to make the analyses in this study possible.
- All professors, contributors, and staff members of the SAHC programme for their guidance, dedication, and support.
- My family, friends, and SAHC colleagues for their constant support, inspiration and encouragement.

This page is left blank on purpose.

ABSTRACT

Historic structures are an important cultural aspect of societies as they tie the present day to the past. To preserve these historic structures, understanding of the structural behavior is necessary to help determine the safety level and verify if strengthening is required. In most cases, the non-linear structural analysis of these structures is difficult to perform due to the highly irregular geometric features, the inherent variability within the materials, as well as the limited amount of experimental data available. This is especially true in the case of masonry churches such as St. Ann's Church, which was constructed in the 18th century in the Czech Republic and belongs to the so-called Broumov group of churches. The state-of-art review encompassed within the work focuses on current methodologies for analyzing the strength of masonry structures and the viability of stochastic analysis along with the utilization of random fields. The present work details a specific methodology, subsequent application, and a presentation and discussion of the results for the overall compressive strength of the masonry walls of St. Ann's Church.

A multi-scale 2D finite element modelling approach was adopted. Based on the statistical analysis of the walls, in a mesoscale-level representation of masonry, small stones were grouped in with the mortar and treated as a matrix component with homogenized properties, while large stones were treated as discrete inhomogeneities. To characterize this matrix component, microscale-level models were used, in which only the small stones and mortar were represented as inhomogeneity and matrix phases, respectively. These models were built using test-windows placed in randomly generated, statistically equivalent microstructure morphologies. By simulating uniaxial compression and tension tests, statistical distributions for compressive and tensile strength, stiffness, and fracture energy were determined. On the mesoscale-level, overall stiffness and compressive strength were determined by simulating uniaxial compression tests on models considering only the large stones embedded in the homogenized matrix. An initial calculation was run with uniform properties for the matrix using mean values obtained from the micro-scale models. Secondly, random fields were utilized to describe the matrix properties to account for the inherent variability and inhomogeneity of the matrix. Furthermore, the multi-scale study was performed for two different threshold sizes defining the "small" stones to compare differences.

Based on the analyses completed for the meso-scale models with uniform matrix, the average compressive strength was calculated to be 0.95-0.9 MPa, with the lower bound values coming from models with decreased projected stone area. Overall, the compressive strength decreased from the mortar to micro-scale to mesoscale-levels due to high stress concentrations in the mortar/matrix material caused by the irregular topology of the stones. The models where matrix variability was represented with random fields exhibited similar failure mechanisms but with strengths 5-6% lower than the models with a uniform matrix. Considering such low changes in strength with little to no influence on the development of the failure mechanisms, the effect of the spatial variability of the matrix properties was considered insignificant. Lastly, qualitative methods were utilized to validate the results to be used in equivalent continuum-based modelling and further analysis of St. Ann's Church.

Keywords: historical structures, structural analysis, nonlinear finite element analysis, masonry walls, micro-modelling, spatial variability of material parameters, random fields

This page is left blank on purpose.

ABSTRAKT

Historické konstrukce jsou pro společnost významným kulturním aspektem, neboť spojují současnost s minulostí. Pro zachování historických konstrukcí je nutné porozumět jejich mechanickému chování, což následně umožní posoudit úroveň jejich bezpečnosti a určit, zda je nutné jejich zesilování. Provádění nelineární analýzy těchto konstrukcí je obvykle složité vzhledem k jejich velmi nepravidelným geometrickým tvarům, přirozené variabilitě materiálů i nedostatku experimentálních dat. Toto konstatování zejména platí pro zděné kostely, jakým je například Kostel sv. Anny, který byl postaven v 18. století v České Republice a patří do tzv. skupiny broumovských kostelů. Rešeršní část této diplomové práce je zaměřena na moderní metody analýzy únosnosti zděných konstrukcí a na možnosti stochastické analýzy s využitím náhodných polí. Předložená práce detailně popisuje specifickou metodiku pro určení tlakové pevnosti zdiva a prezentuje její využití, výsledky a diskusi na příkladu Kostela sv. Anny.

V práci je použit přístup založený na víceúrovňovém 2D modelování pomocí metody konečných prvků. Na mezoskopické úrovni byly na základě statistické analýzy zdiva malé kameny zahrnuty společně s maltou do fáze zhomogenizované matrice, zatímco velké kameny byly uvažovány jako diskrétní nehomogenity. Materiálové charakteristiky zmíněné matrice pak byly určeny pomocí modelů na mikroúrovni, ve kterých byly jako jednotlivé fáze uvažovány pouze malta (matrice) a malé kameny (nehomogenity). Mikromodely byly vytvořeny na základě pozorovacích oken, která byla umístěna do náhodně generované statisticky ekvivalentní morfologie mikrostruktury. Simulací zkoušek v jednoosém tlaku a tahu byla získána statistická rozdělení tlakové a tahové pevnosti, tuhosti a lomové energie. Na mezoúrovni pak byly celková tuhost a tlaková pevnost určeny simulacemi testů v jednoosém tlaku na modelech sestávajících z velkých kamenů zasazených do zhomogenizované matrice. Při prvním způsobu výpočtu byly vlastnosti matrice uvažovány jako konstantní v celém jejím objemu, přičemž byly použity střední hodnoty parametrů vypočtených z mikroúrovňových modelů. Při druhém způsobu pak byla použita pro parametry náhodná pole, čímž byla zohledněna přirozená variabilita a nehomogenita matrice. Popsaná víceúrovňová studie byla navíc provedena pro dvě různé prahové hodnoty velikosti definující „malé“ kameny, aby byl určen vliv této hodnoty.

Na základě výpočtů provedených na mezoúrovňových modelech s matricí s konstantními vlastnostmi byla určena průměrná tlaková pevnost zdiva v rozsahu 0,95-0,9 MPa, přičemž nižší hodnota odpovídá modelům, kde matrice měla větší objemové zastoupení. Byl pozorován obecný trend, že tlaková pevnost klesala od hodnoty pro samotnou maltu, přes hodnoty získané z mikroúrovňových modelů, až k hodnotám z mezoúrovňových modelů. Tento jev je přisuzován vysokým koncentracím napětí ve fázi malty/matrice, které byly vyvolány nepravidelnou topologií kamenů. Modely, kde byla variabilita matrice zohledněna pomocí náhodných polí, vykazovaly podobné mechanismy porušení jako modely s konstantní matricí a jejich pevnosti byly o 5-6 % nižší. S ohledem na takto malý vliv na pevnost i režim porušení je vliv prostorové variability vlastností matrice považován za nevýznamný. Na závěr byly výsledky studie ověřeny pomocí kvalitativních

metod. Tyto výsledky mohou být použity pro modelování pomocí ekvivalentního kontinua a další analýzu kostela sv. Anny.

Klíčová slova: historické konstrukce, analýza konstrukcí, nelineární analýza metodou konečných prvků, zděné stěny, mikromodelování, prostorová variabilita materiálových parametrů, náhodná pole

This page is left blank on purpose.

TABLE OF CONTENTS

LIST OF FIGURES

LIST OF TABLES

LIST OF APPENDICES

1. INTRODUCTION

Masonry has been around for thousands of years and is still relatively common around the world in today's building industry due to the simple fact that it can be easily constructed with materials that are sourced and manufactured locally. Typical masonry consists of brick or stone units bonded together with or without mortar and can take the form of a variety of different textures and topologies creating heterogeneous mixtures with periodic, quasi-periodic, or non-periodic arrangements. Historic masonry structures are characterized by the material manufacturing and construction technologies and processes available at the time and are highly complex to analyze due to numerous geometric and material variabilities. There is a high demand for the proper analysis of historic structures to allow for the complete understanding of the structural behavior, leading to the determination of the safety of the structure as well as whether strengthening is required, which is often an expensive and invasive undertaking.

With the increased power of computing along with numerical tools such as the finite element method, discrete element method, limit analysis, and the applied element method, the complex geometry and behavior of masonry can be suitably modelled (Abdulla, Cunningham, & Gillie, 2017). In the finite element method, masonry has been idealized into macro-models, meso-models and micro-models (Lorenço, 1996; Mojsilović, 2011), to reliably mimic the complex behavior of the global structure as well as the units, mortar and joints with the goal of fully understanding masonry behavior in various applications and load cases. Since experimental methods can be expensive to fabricate and provide relatively limited results, the use of numerical methods is crucial. In recent times, multiple computer programs have been created to randomly create geometry that stochastically represents a masonry wall panel and a few studies have been done reviewing the importance of the spatial variation of micro-parameters of masonry (Zhang, Hofmann, & Beyer, 2018; Zhang, Taheri Mousavi, Richart, Molinari, & Beyer, 2017). Among the research done, there has been a proven significance of the pairing of statistical analysis with structural analysis and has been shown to often be very helpful when dealing with unknown materials or materials with highly variable properties such as masonry (Zhang et al., 2017).

The aim of the thesis is to review current state-of-the-art techniques applied to the 2D analysis of non-periodic masonry and to develop methodology used to perform a systematic stochastic non-linear analysis of the historic masonry walls. The methodology will be demonstrated on a case study of the Broumov Group of Churches located in the Czech Republic, specifically St. Ann's Church, and will utilize a multi-scale micro-modelling approach to obtain an overall compressive strength and stiffness of the masonry wall that can be eventually used in a structural-scale analysis of the structure.

2. STATE-OF-ART REVIEW

Masonry is difficult to analyze because of its inhomogeneity on a local and global scale due to the use of multiple components with varying properties. Specifically, the use of mortar in combination with units produces highly anisotropic behavior, showcasing specific directional properties, which lead to various failure modes and mechanics such as cracking in tension, crushing in compression, and sliding in shear. Thus, it is imperative that main mechanical actions such as bonding, cohesion and friction along the unit-mortar interface are accounted for within analyses as they provide insight into overall structural capacity and the various failure mechanisms (Lorenço, 1996).

While experiments offer a good way to calculate strength and deformation capacities of masonry structures, they are very limited in scope when compared to the possible formations and variations of built masonry that exist in the world today (Zhang et al., 2018). Therefore, the value of proper numerical modeling and stochastic analysis cannot be understated and the state-of-art techniques that have been developed will be discussed in this section.

2.1 MODELLING TYPES

In general, there are three main modelling types to consider when analyzing masonry structures and the choice of model used highly depends on the overall goal of the analysis. The three main types of modelling are macro-modelling, meso-modelling, and micro-modelling and are briefly described within this section.

Macro-modelling of masonry considers the interaction of units and mortar to be negligible and instead lumps together the separate components into one continuous element with smeared values based on the micro-properties of the constituents (Lorenço, 1996; Mojsilović, 2011). The model focuses on the global structural behavior while still accounting for the anisotropic properties intrinsic to masonry and is typically used for large and complex masonry structures where loads and stresses can be averaged across the whole structure. While macro-modelling can provide relatively good results regarding the overall behavior of the structure, it cannot model detailed failure mechanisms (Roca, Cervera, Gariup, & Pela', 2010).

Meso-modelling, otherwise known as simplified micro-modelling, is a process in which the units are extended over the mortar and the mortar is simply reduced to an interface. Units are made up of continuous elements with the mortar and interface being made up of discontinuous elements. This model can account for the properties of cohesion, bonding and friction which are the main mechanical actions leading to failure, typically occurring along the joints (Lorenço, 1996).

Micro-modelling consists of modelling fully detailed units, mortar and the unit to mortar interface and allows for the analysis of the structure on a more thorough level. It is particularly useful when it comes to evaluation of heterogeneous topologies as it closely represents the behavior of individual components of the masonry and its behavior when acting together as a composite (Lorenço, 1996). While it is limited to relatively small elements due to computational power required, the advantage is that it can depict the local response of the material.

While both the complexity of the model as well as computational requirements increase moving from macro-modelling to micro-modelling, the accuracy of the results improve, but a balance must be struck between cost and accuracy as available time and computing power is finite. Also, the amount and availability of input information must be considered, as the level of detail required increases when using micro-models in comparison to macro-models. For all model types, boundary conditions must be carefully chosen as they directly influence results obtained from the analysis (Lorenço, 1996).

In summary, using strength-deformation behavior from macro-models and detailed failure modes and crack growth in micro-models, masonry structures can be effectively analyzed to provide greater knowledge and understanding of historic masonry damages and failure mechanisms to ensure proper measures for conservation, repair and strengthening can be performed to avoid catastrophic failures (Lorenço, 1996).

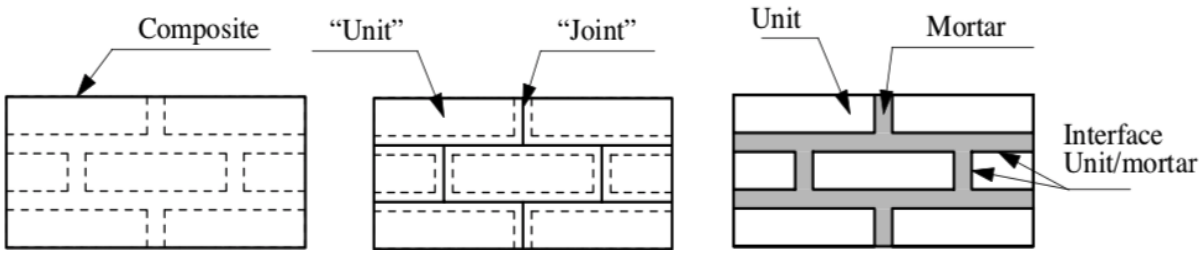

Figure 1 - Macro-model, Meso-model, Micro-model (Lorenço, 1996).

2.2 HOMOGENIZATION

The homogenization technique is the process in which a material with a complex substructure, such as masonry, is simplified into an equivalent continuum that represents the overall properties of the material. The simplified equivalent continuum does not include specific details on the units and mortar and therefore can be easily meshed within a finite element analysis and avoids complications produced by the modelling of a unit-mortar interface (Roca et al., 2010). The technique can be used to evaluate the linear and non-linear behavior of masonry with low computational effort and produces comparable results to that of experimental data (Cluni & Gusella, 2004). Homogenization is the link between macro and micro-modelling of masonry and the different methods developed will be briefly discussed within this section.

2.2.1 REPRESENTATIVE VOLUME ELEMENT

A representative volume element (RVE) includes a section of the masonry with enough material phases to fully represent the whole structure and can be used to determine the average values of stresses and strains using a variety of methods. In other words, the size of an RVE should be large enough to contain numerous material inhomogeneities but also small enough so that stress and strain variations within it are negligible (Kabele, 2018).

It should be noted that for any areas smaller than the size of the RVE analyzed, the RVE method cannot be used and the actual arrangement of the units and mortar need to be considered. The RVE method can be applied multiple times in various locations to quasi-periodic and non-periodic masonry structures to account for the variability in geometry (Cluni & Gusella, 2004).

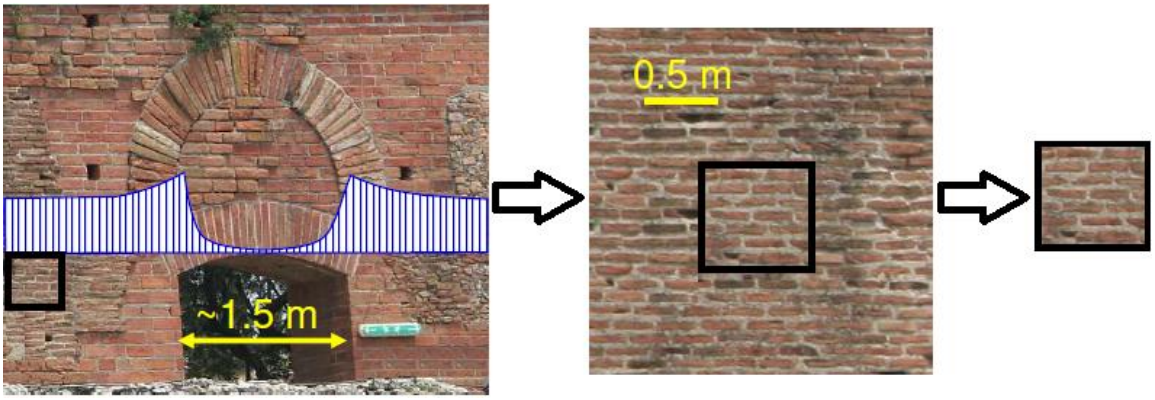

Figure 2 - Representative Volume Element for Masonry (Kabele, 2018).

2.2.2 PERIODIC MASONRY

Periodic masonry is defined by units and mortar head and bed joints that have equivalent dimensions; therefore, geometry as well as material properties are arranged in a repeated fashion. Homogenization of periodic masonry is done by means of a periodic unit cell (PUC), which allows for the calculation of mean values for material properties and behaviors, and obtaining equivalent mechanical properties can be done in various ways such as discrete modelling, interface modelling, and micro-polar material models (Cavalagli, Cluni, & Gusella, 2018). A model of the PUC is shown in Figure 3. PUC models include many simplifications and essentially can only be used for periodic masonry, therefore its application to historical structures is quite limited (Cluni & Gusella, 2004).

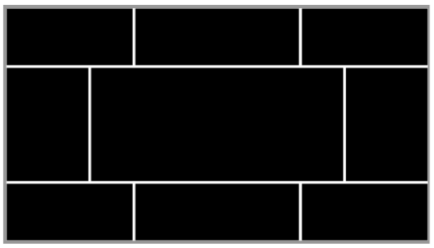

Figure 3 - Periodic Unit Cell for Masonry (Šejnoha, Šejnoha, Zeman, Sýkora, & Vorel, 2008).

2.2.3 QUASI-PERIODIC MASONRY

Quasi-periodic masonry is defined by units in a row having the same height with recurring bed (horizontal) joints with varying widths, creating offset and scattered head joints (vertical joints). See Figure 4 for a detail on quasi-periodic masonry.

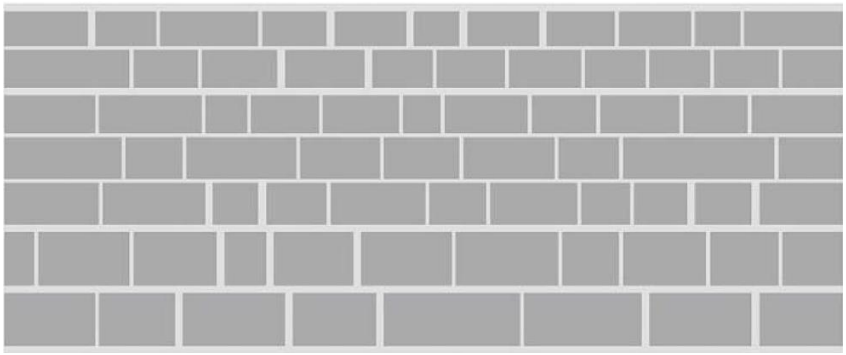

Figure 4 - Quasi-Periodic Masonry (Cluni & Gusella, 2004).

For this type of masonry, the simple approach of the PUC cannot be applied, and instead the method of a statistically equivalent periodic unit cell (SEPUC) is applied as shown in (Cavalagli, Cluni, & Gusella, 2013; Cavalagli et al., 2018; Zeman & Šejnoha, 2007). A SEPUC utilizes a probabilistic approach to develop a PUC with statistically similar geometric properties as the structure analyzed (Zeman & Šejnoha, 2007). Digital imaging can be used to statistically analyze geometric parameters such as length and height of stones as well as bed and head mortar joints and create probability density functions. Using these functions, several SEPUCs can be randomly generated and analyzed using a Monte Carlo analysis to define criteria that identifies the best suitable SEPUC among the ones generated to model the behavior. The criteria accounts for both geometrical dimensions of the masonry components and the concentration ratio of each constituent making up the masonry component. Critical states for a homogenized continuum can then be determined using a mean stresses approach that provides an overall failure criterion based on the mean stress state of each constituent. Overall, the SEPUC is proven to be an efficient method to define homogenized properties for a quasi-periodic masonry structure from stochastic meso-modelling analysis, which can then be applied in a macro-modelling analysis (Cavalagli et al., 2013, 2018).

2.2.4 NON-PERIODIC MASONRY

Non-periodic masonry is defined as masonry containing irregular shapes and dimensions for units as well as mortar, with the spatial distribution of units and mortar being random. Since many historical structures include non-periodic masonry, many authors such as (Cluni & Gusella, 2004; Falsone & Lombardo, 2007; Gusella & Federico, 2006; Milani, Esquivel, Lourenço, Riveiro, & Oliveira, 2013; Šejnoha et al., 2008), have utilized stochastic continuum micro-mechanics in unison with RVEs to analyze quasi-periodic as well as non-periodic masonry to determine a homogenized equivalent continuum. In (Milani et al., 2013), data gained from laser scanning technology and digital image processing of a historical masonry structure was used to create a geometric model in full detail and allowed for the creation of finite element model of heterogeneous structure. Numerous RVEs with varying sizes were then arbitrarily chosen and analyses were completed considering the heterogenous structure. Afterwards, a homogenized model was created using a rigid-plastic homogenization

procedure that accounted for the geometric properties and texture irregularity. The models were then compared to show the acceptable reliability of the homogenized model (Milani et al., 2013).

Similarly, in (Cluni & Gusella, 2004), the elastic stiffness tensor of an RVE of a non-periodic masonry structure was estimated by averaging results obtained from various arbitrarily chosen RVEs with randomized essential and natural boundary conditions, also known as the mechanical convergence criterion. This allowed for a relatively accurate view on the global behavior of the structure while still accounting for heterogeneity of the masonry. In a further study done by (Gusella & Federico, 2006), a multitude of finite-sized test windows were made inside of a chosen RVE and an enhanced two-step convergence criterion was utilized, one being probabilistic and another mechanical, to determine if the test windows statistically match the RVE. From the analysis it was determined that a test-window size of 130 cm was sufficient to statistically limit the geometric difference from the RVE (Gusella & Federico, 2006). See Figure 5 for an illustration of the finite-sized test window method.

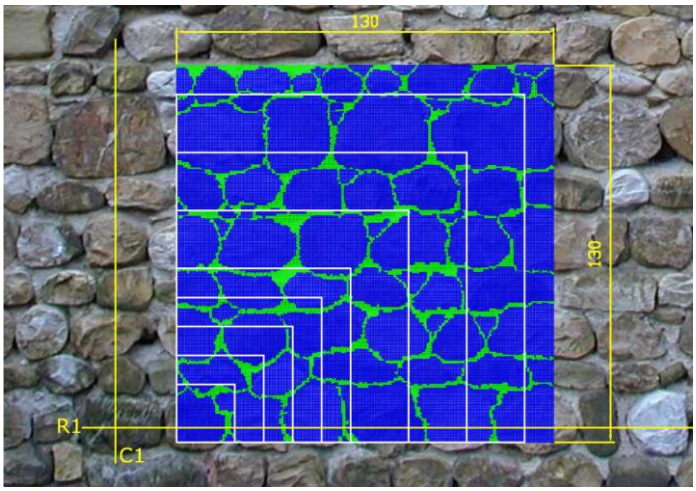

Figure 5 - Test-Window Method within an RVE (Gusella & Federico, 2006).

2.3 STOCHASTIC CHARACTERIZATION OF IRREGULAR GEOMETRY & TOPOLOGY GENERATORS

When dealing with irregular geometry, stochastic characterization of the masonry can be utilized to account for the irregularities through suitable definition of the random properties. As discussed in the previous sections, in (Šejnoha et al., 2008), a SEPUC based on probabilistic properties was created to produce a reasonable approximation and in (Gusella & Federico, 2006), the test-window method was used in unison with coupling probabilistic and mechanical convergence methods together. While these two methods provide relatively accurate results, they do not work in unison with the theory of random fields (Falsone & Lombardo, 2007). Therefore, (Falsone & Lombardo, 2007) detail a procedure that gives the suitable representation of the properties of irregular masonry through the theory of random fields, starting with the digital image processing of an image of the masonry to automatically evaluate the characteristics of the geometry and provide statistical information in both the space and frequency domains. MATLAB code, called STONES, was created to automatically generate statistical data

based on a colored picture of the masonry and correlation functions are then used to generate random fields to describe the geometric properties of masonry based on the deterministic properties of each constituent (Falsone & Lombardo, 2007). An output of the analysis completed in STONES can be seen in Figure 6.

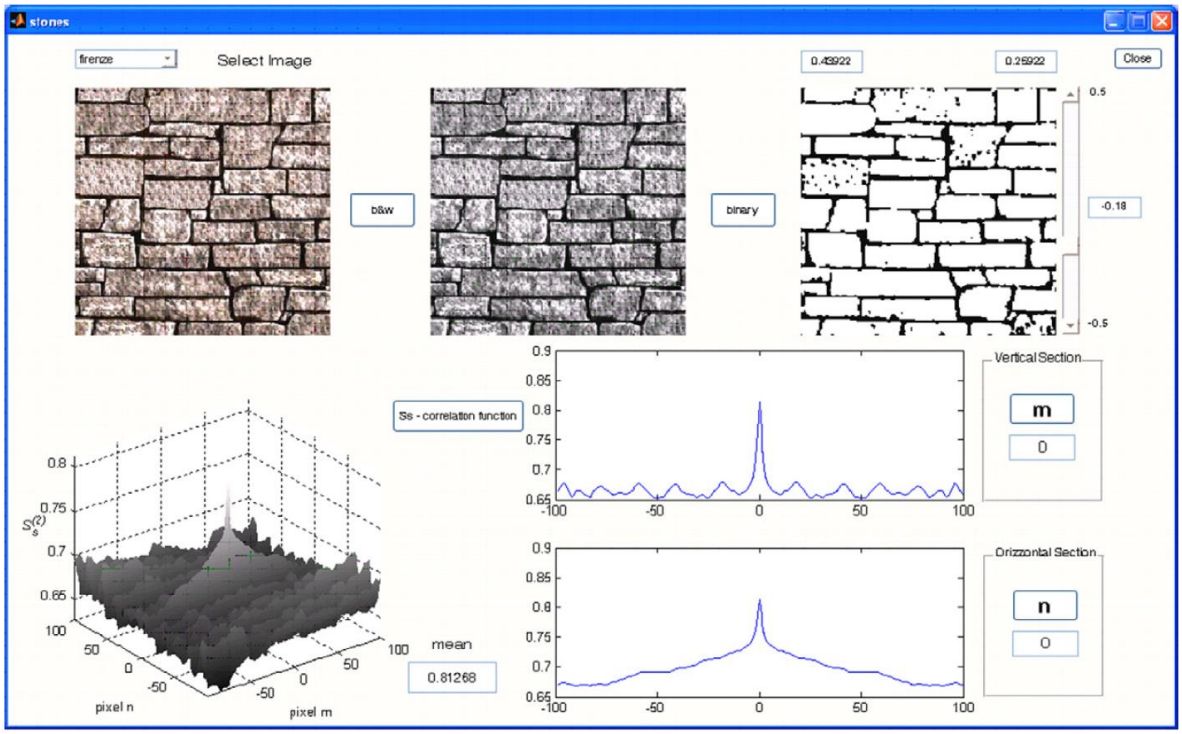

Figure 6 - Irregular Masonry analyzed using STONES (Falsone & Lombardo, 2007).

Statistically similar virtual samples of irregular masonry walls were generated in (Spence, Gioffrè, & Grigoriu, 2008), by characterizing the geometry with a random field model to form units which are then randomly packaged together by Poisson fields with a sieving curve to match the real-world specimen. The random fields utilized are then transferred into a Monte-Carlo simulation to create virtual specimens based on unit geometry and global morphology of the real-structure (Spence et al., 2008). An illustration of the real-world masonry topology and randomly generated topology is shown in Figure 7.

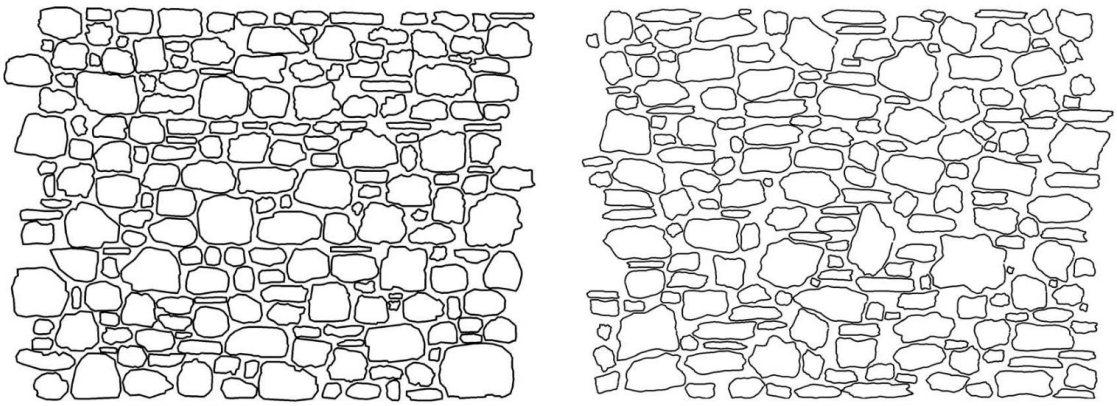

Figure 7 - Real-World Topology (Left) Randomly Generated Topology (Right) (Spence et al., 2008).

Another 2D topology generator for historical masonry has been developed by (Zhang et al., 2018), which can create random topologies based on numerous input parameters. While the generator can create a large variety of topologies closely related to the typical ones found in the Italian code, a trial-and-error procedure must be used to represent and obtain the specific topology required.

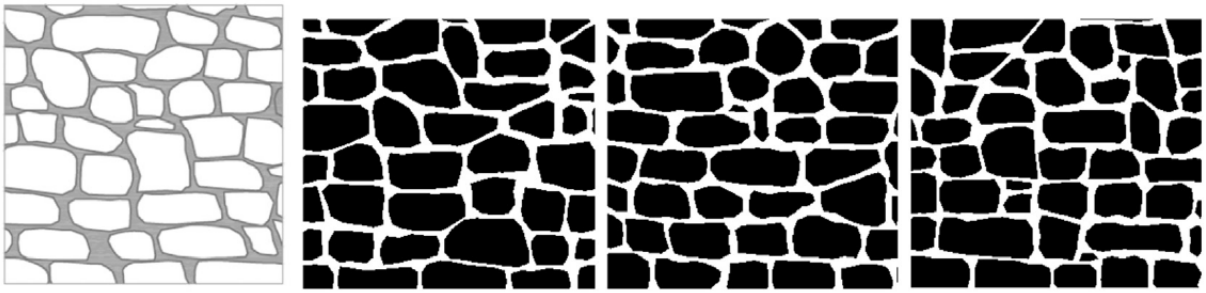

Figure 8 - Real-World Topology (Left) and Randomly Generated Topologies (Zhang et al., 2018).

2.4 STOCHASTIC CHARACTERIZATION OF MATERIAL PROPERTIES

When modelling masonry, the description of mechanical properties is crucial to provide accuracy, regardless of model used. In many cases for macro-models, the main homogenized properties include Young's modulus, compressive strength, Poisson's ratio, peak compressive strain, tensile strength, and fracture energy in tension, defined as the amount of energy required for the formation of a unit crack area. In the absence of experimental tests for historic masonry, the homogenized properties can be qualitatively estimated using the Masonry Quality Index (MQI) method, which accounts for certain parameters when considering the "rule of art" for masonry construction to determine the overall behaviour, compactness and monolithicity of the masonry (Borri, Corradi, Castori, & De Maria, 2015). Often for micro-models, each of the materials must be identified with unique values for Young's modulus, compressive strength, Poisson's ratio, peak compressive strain, tensile strength, and fracture energy in tension. Unit-mortar interfaces can be developed from the values of cohesion, friction and bonding of the units to mortar usually taken from experimental tests (Lorenço, 1996; Šejnoha et al., 2008).

Typically, both macro and micro-models have elements with uniform material properties, which is considered an idealization of the material and does not realistically represent the possible distribution of values throughout the material. This is quite normal when modelling masonry structures as the models do not account for the variation in specific materials. Due to workmanship factors such as the batching of mortar, filling of joints, level of preparation prior to execution of work, and factors effecting the curing of mortar, the spatial variation of material properties should be considered when modelling masonry.

The use of random fields and stochastic analysis can help account for these variations to provide for a reliable analysis when investigating historical structures. A random field can be considered as a randomized set of values representing a heterogeneous spatial field that are assigned

to each point within the field, with the correlation length determining the variability of the values or in other words, the extent of randomness found within the spatial field (Ostoja-Starzewski, 2006; Speer, 2012; Zhang et al., 2017). The mathematics behind random fields are not discussed within this report, but for more information on random fields see (Novák, Teplý, Keršner, & Vořechovský, 2002).

In (Speer, 2012), deterministic finite element macro-models of a masonry structure were created in ATENA software using material constitutive models of isotropic quasi-brittle fracture-plastic model with smeared cracks to characterize the masonry. Using SARA and FREET software, both random variables and random fields were generated for the material properties using a Latin Hypercube sampling method and several analyses were run among the differing models in ATENA to determine the effect of spatial variation of properties on the overall structural behaviour. Histograms and graphs of the structural behaviour were then generated in FREET to show the significance of the spatial variability of material parameters on structural behaviour and the increased vulnerability due to concentrated weak areas generated by random fields. Overall, the stochastic models exhibited a reduction in strength when compared to the deterministic models (Speer, 2012).

Random fields were utilized in unison with micro-models by (Zhang et al., 2017), to generate the strength of mortar and the unit-mortar interface within a masonry structure. Critical stress, fracture energy and the coefficient of friction were taken to be correlated properties following a Gaussian random field, with a correlation length varying between 0.0 m and 0.2 m for the friction coefficient. From the results in Figure 9, (Zhang et al., 2017) determined that the overall force capacity decreased with the increase in correlation length, therefore the effect of random fields and correlation of material properties on the post-peak behavior cannot be neglected lead as it may lead to an overestimation of strength (Zhang et al., 2017).

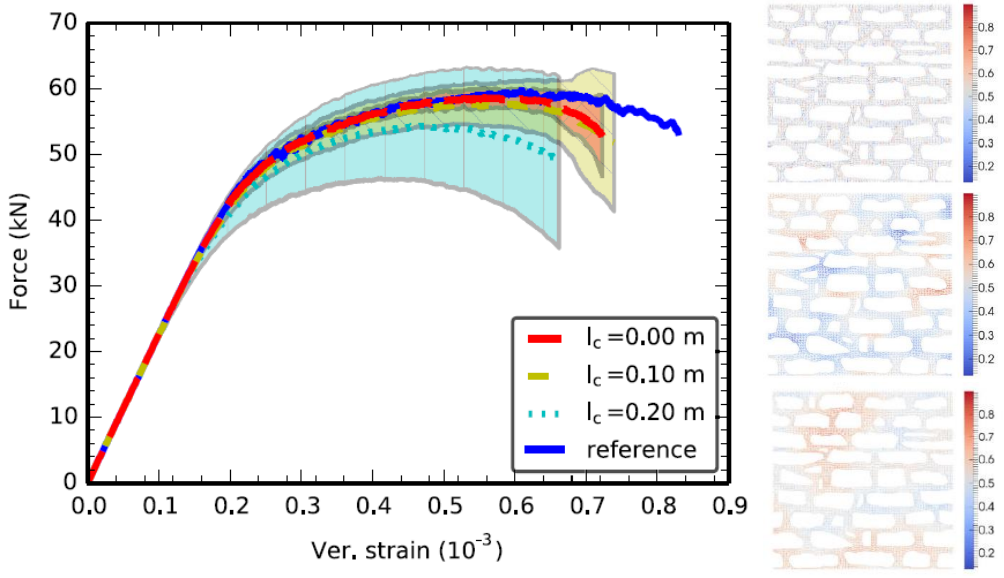

Figure 9 - Force-Deformation Envelopes with Various Friction Coefficient Correlation Lengths (Left) and Random Field Samples for 0.0 m, 0.1 m, and 0.2 m Friction Coefficient Correlation Lengths (Right) (Zhang et al., 2017).

2.5 SUMMARY OF FINDINGS

In summary, historic masonry structures can be effectively analyzed with the use of micro-modelling in combination with macro-modelling. The RVE method is proven to be a good approximation for the homogenization of masonry but the determination of a proper RVE is complex especially when analyzing masonry that is non-periodic. The importance of statistically analyzing the geometry of the structure before modelling to determine the proper window size for the RVE cannot be understated, and with these statistical properties, random geometries can be developed to assist in the analysis of the true strength of non-periodic masonry. Furthermore, the spatial variability in material properties were shown to be significant and should be considered during non-linear structural analyses.

3. METHODOLOGY & APPLICATION

The structure under study and methodology utilized for the determination of material and modelling parameters is discussed within this section.

3.1 HISTORY

Historic masonry structures with highly irregular geometry can be found throughout the world and many are under study to ensure structural safety and proper conservation. As previously stated, this thesis will focus on a historic masonry structure part of the Broumov Group of Churches located within the Czech Republic. The Broumov Group of Churches contains multiple three-leaf masonry wall churches built in the early 18th century. Due to the external plaster covering on most of the churches, St. Ann's Church was chosen to be analyzed as it had the most exposed stone and mortar surface area of the group. St. Ann's Church consists of locally sourced stone rubble masonry containing irregularly shaped units of highly varying sizes with mainly 5 different stone topologies identified as ignimbrite, yellow sandstone, red sandstone, fine grained red sandstone, and light sandstone. The masonry wall units are bonded together with natural hydraulic lime mortar and the internal leaf is thought to be filled with rubble infill. The walls are assumed to be 1.2 m thick, with the external and internal walls assumed to be 0.5 m wide and the infill being 0.2 m. An image of St. Ann's Church can be seen in Figure 10. For a review on the history of the Broumov Group of Churches refer to (Gajjar, 2018) and (Scacco, 2018).

Figure 10 - St. Ann's Church in Vižňov, Czech Republic.

3.2 GEOMETRIC STATISTICAL ANALYSIS

Due to the irregularity in stone size, shape, and placement, the external masonry leaf of St. Ann's Church was statistically analyzed to determine the geometric detail for models to be used for the analysis. The evaluation was completed by analyzing 6 sample wall panels with a size of 1 m², approximately 3 times larger than the area of the largest stone observed within the structure. Locations were chosen based on available size of exposed surface near the ground level. Sample locations and images of the wall panels can be seen in Figures 11-14.

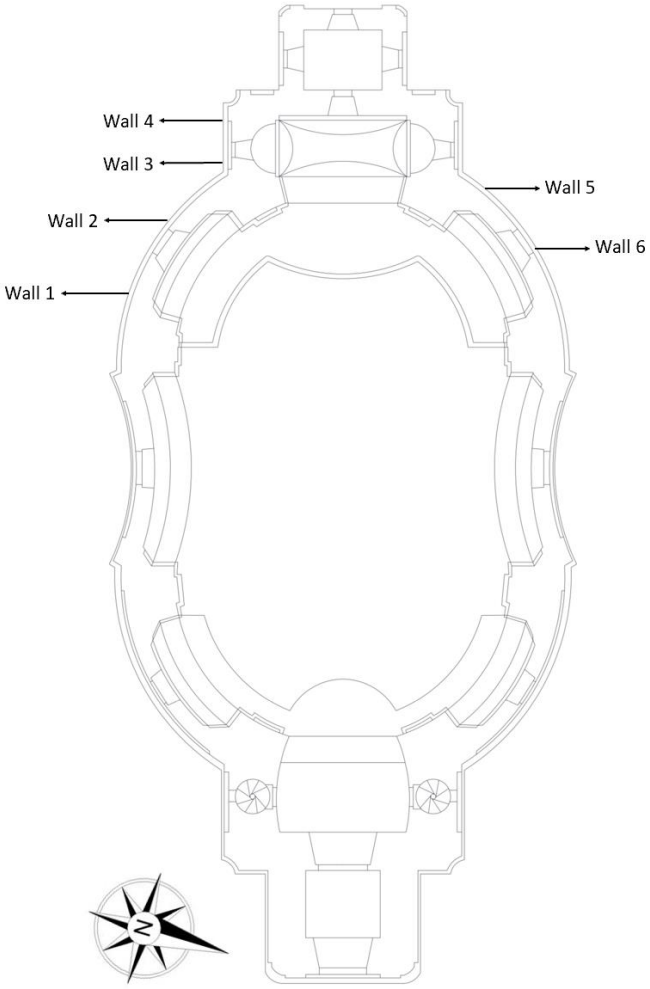

Figure 11 - Locations of Masonry Wall Sections Sampled at St. Ann's Church.

Figure 12 - Wall Section Samples 1 and 2.

Figure 13 - Wall Section Samples 3 and 4.

Figure 14 - Wall Section Samples 5 and 6.

Based on the analysis completed, 80% of the area on average is stone, with the remaining 20% taken up by mortar. Utilizing a cumulative density function, it was seen that approximately 50% of stone elements are less than 0.001 m², and approximately 68% of stones are less than 0.002 m². The summarized results of the statistical analysis are illustrated in Figure 15 and 16, with the full set of calculations found in Appendix A.

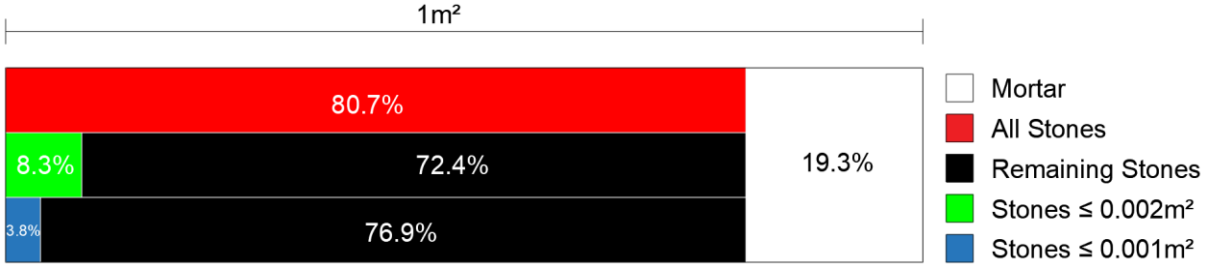

Figure 15 - Statistical Analysis of Masonry Wall Sections.

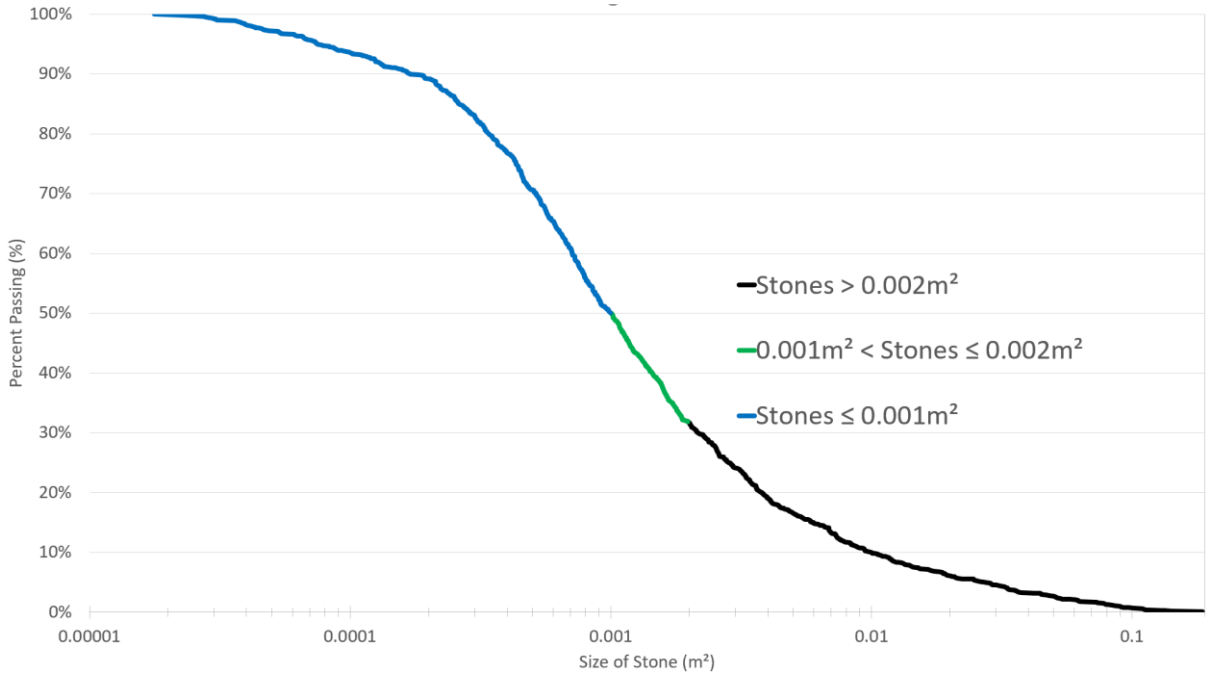

Figure 16 - Cumulative Distribution of Stone Size Using Log-Normal Scale.

3.3 MATERIAL PROPERTIES OF MASONRY CONSTITUENTS

Since micro-modelling will be applied within this study, material properties of the units and mortar were required. Therefore, a combination of non-destructive and minor-destructive test methods were utilized to assist in the determination of reliable material properties. The test methods and results that will be incorporated into models are described within this section.

3.3.1 STONE PROPERTIES

3.3.1.1 SCHMIDT HAMMER TESTING

A Schmidt hammer, known as a non-destructive test method, was used to determine the surface hardness, or approximate compressive strength of the various stone units found in the masonry walls at St. Ann's Church. At the time of the test, three different Schmidt hammers were available for use; a Proceq Type L rock hammer, Proceq Type N rock hammer, and a ZC 3 Schmidt hammer, and all 3 were used to compare results for 1 section of wall. The Proceq Type L Rock Hammer was chosen to continue with further testing due to the initial high results of the stone compressive strengths with low coefficient of variance. Three of the six masonry wall panels were arbitrarily chosen and each of the 5 various stone units were tested in each. The test included 15 hits for each of the differing stones, and the mean value, standard deviation and compressive strength were automatically calculated with the internal software of the hammer. An example of one the masonry wall sections analyzed can be seen in Figure 17 and the summarized results can be seen in Table 1.

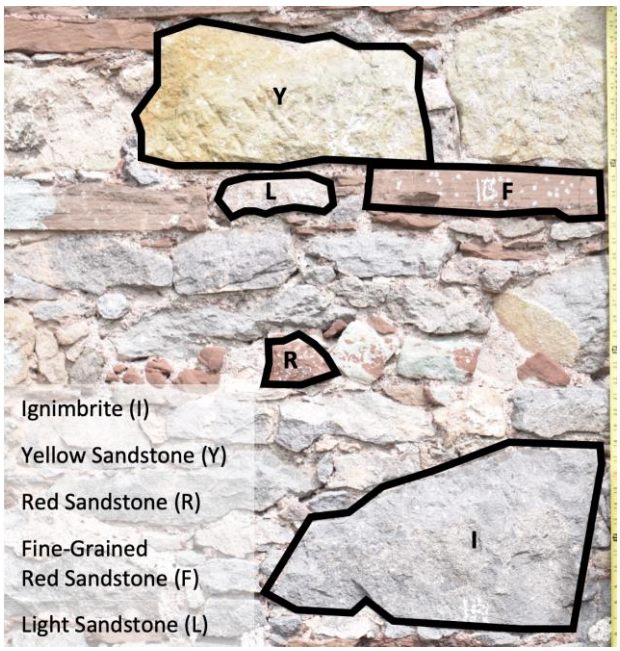

Figure 17 - Typical Wall Section Analyzed Using Schmidt Hammer.

Table 1 - Schmidt Hammer Results.

Stone	Ignimbrite (I)			Yellow Sandstone (Y)			Red Sandstone (R)			Light Sandstone (L)			Fine-Grained Red Sandstone (F)		
Wall Section	1	3	6	1	3	6	1	3	6	1	3	6	1	3	6
Average Value	51	51	44	42	42	36	46	49	51	27	46	39	47	42	46
St. Dev	7	8	6	4	5	7	4	13	5	4	3	4	7	7	2
COV (%)	14	16	15	11	11	19	8	27	10	15	7	11	16	16	5
Compressive Strength, f_c (MPa)	49	51	33	28	28	20	37	43	50	11	36	24	39	29	35
Average f_c (MPa)	44			25			43			21			34		

3.3.1.2 CORING

Coring of the masonry walls at St. Ann's Church was completed by a team from the Czech Technical University, led by Professor Pavel Kuklík in 2018. The findings and results of the compression tests were compared to the Schmidt Hammer results and shown to be relatively similar, other than the results for the light sandstone. The coring results are considered more reliable as the coefficient of variance for the Schmidt hammer results are relatively high, which can be associated with an error when testing small, irregular surfaces (*Proceq Rock Schmidt Hammer Operating Instructions*, 2017). Furthermore, the secant stiffness of each of the stones was tested and calculated. Figure 18 details the core locations and Table 2 summarizes the key results from the tests completed by Professor Pavel Kuklík. The full test results can be found in (Kuklík, 2018).

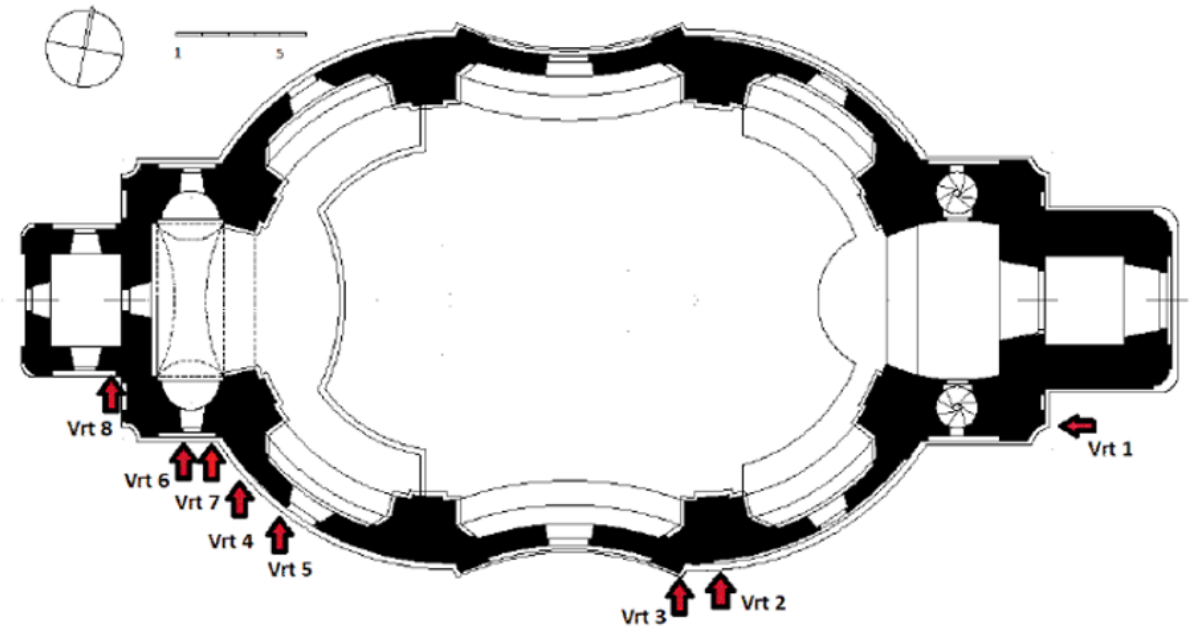

Figure 18 - Coring Locations at St. Ann's Church (Kuklík, 2018).

Table 2 - Coring Test Results (Kuklík, 2018).

Stone Typology	Core #	Compressive Strength, f_c (MPa)	Young's Modulus, E_{sec} (GPa)
Yellow Sandstone	Vr1	28.99	7.51
Ignimbrite	Vr2	34.96	9.49
Ignimbrite	Vr3	49.27	9.30
Red Sandstone	Vr4	38.15	5.41
Fine-Grained Red Sandstone	Vr5	47.8	9.21
Light Sandstone	Vr6	44.94	6.53
Light Sandstone	Vr7	44.94	10.31
Light Sandstone	Vr8	38.8	8.48

3.3.2 MORTAR PROPERTIES

Three samples of mortar were taken from the Brumov Group of Churches, two from St. Ann's Church and another from St. Barbara's Church. Exact locations of the gathered samples for St. Ann's Church can be seen in Figure 19.

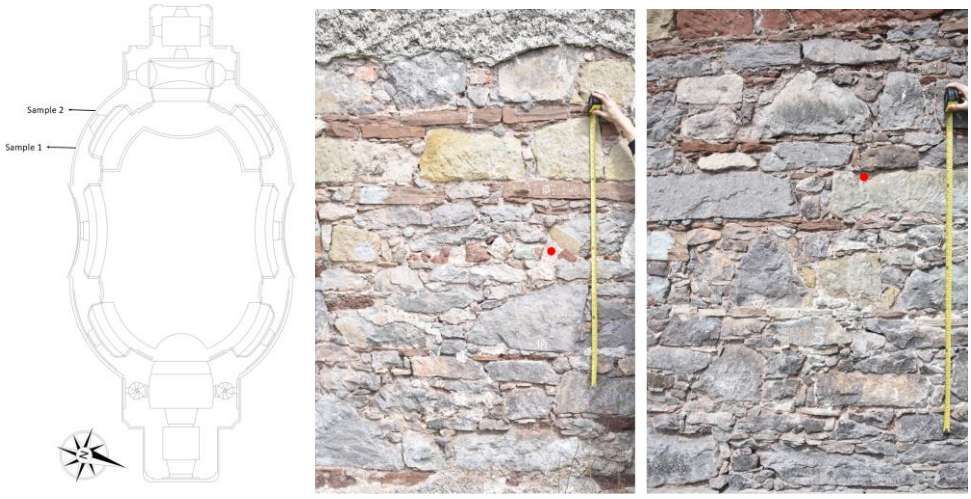

Figure 19 - Sample locations at St. Ann's Church (Left). Sample 1 Wall 1 (Middle). Sample 2 Wall 3 (Right)

Unfortunately, due to the advanced state of degradation of the mortar at each location, only small pieces and fractions were able to be sampled. Due to the irregular geometry and small size of the samples collected, the available testing methods were limited and therefore only scanning electron microscopy (SEM) analysis and porosity test were determined to be feasible to complete for the samples. The purpose of the SEM analysis was to gain information on the elemental composition of the mortar samples to allow for a better characterization of the material properties and thus gain a more accurate representation within the virtual models. The preparation of samples and analysis was completed at the Institute of Theoretical and Applied Mechanics of the Academy of Sciences of the Czech Republic (ITAM) laboratory under the direction and assistance of Ing. Zuzana Slížková and Ing. Lucie Jurkovska, and the results are discussed within this section.

3.3.2.1 SEM ANALYSIS

Instead of using light, SEM machines use a beam of charged particles and electromagnetic lenses to focus on the particles and the configuration of the machine can be described with the following components: electron source, lens system, scan unit, and detection unit. With the detection unit, three basics types of signal can be received: secondary electrons, backscatter electrons, and X-rays which can provide insight into 3 main areas of a sample: topographic information, composite information, and elemental information. An energy dispersive x-ray detector (EDS) was used to produce a qualitative and quantitative microanalysis of the elements present in the samples. Figure 20 details the components of a typical SEM (Avila, 2019).

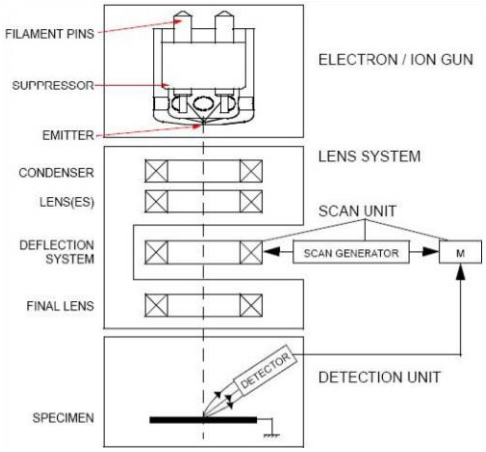

Figure 20 - SEM Configuration (Avila, 2019).

To prepare the field samples they were first randomly chosen, sanded down to produce a flat surface, and placed in a 70-degree Celsius oven for 10 minutes. A plastic mold is covered in silicon gel and filled with an epoxy in which the sample is placed and left to dry for 24hrs. Once set, the samples are removed from the mold and sanded down and cleaned with distilled water to remove all excess epoxy and reveal the flat surface of the samples. The samples are then polished with silica oxides and diamond clothes to ensure a highly reflective surface that is required for the analysis (Goins, 2004). See Figure 21 showing the polishing of the sample as well as the finished product.

Figure 21 - Silica Oxide Polishing of Sample (Left). Prepared Sample (Right).

For the purposes of this report, the SEM results are only briefly discussed, with a special focus on the mortar binder. Microscopic images and images from the SEM analysis of sample 1 can be seen in Figures 22-23. The complete SEM analysis of each of the samples can be seen in Appendix B.

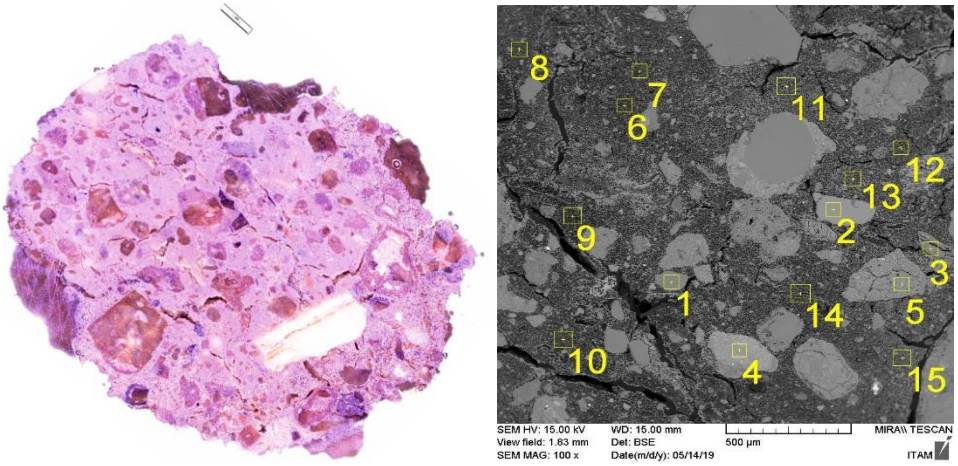

Figure 22 - Microscopic Imaging (Left). SEM Analysis Areas for Sample 2 (Right).

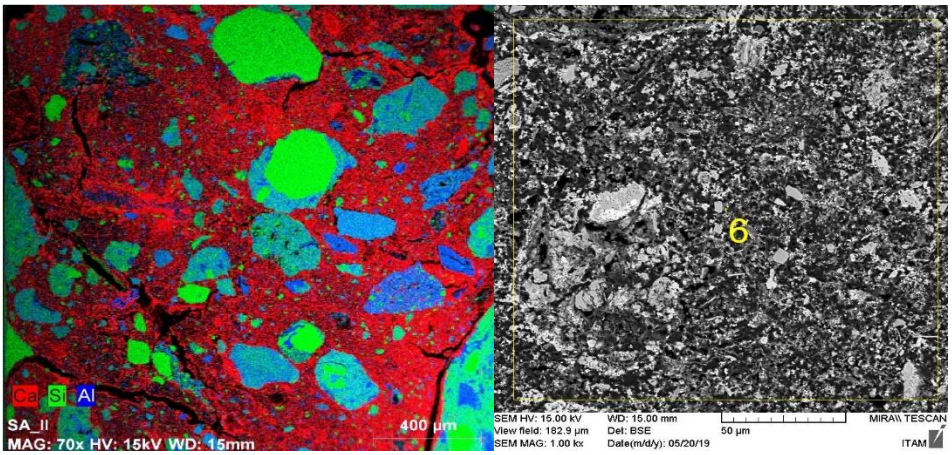

Figure 23 - Overall Elemental Analysis (Left). Area 6 Binder Elemental Analysis (Right).

From the analysis, the aggregates are shown to be feldspar and quartz which was determined by the presence of silica and alumina (SiO_2). This is quite common to find in historical mortar mixtures as it is known to be the world's most abundant mineral group ("Minerals Database - Feldspar," 2019). As can be seen in Figure 24, the aggregates within the mixture can be considered as course and vary in size from 2mm to 20 µm, likely coming from crushed rock during the production process.

Figure 24 - Typical Aggregate Sizes within Mortar.

The binder is shown to be made up of the element Calcium (Ca), formed as calcium carbonate ($CaCO_3$), a significant component of hardened natural hydraulic lime. It is interesting to note the reddish-brown colour of the binder, which could be due to the presence of carbonate bauxite within the mortar mixture. Typically, bauxite ore is very dull and looks like clay or soil since it was formed by the accumulation of clay layers and weathering of limestone and dolomite rocks ("Minerals Database - Aluminum," 2019). This hypothesis aligns with the fact that there is a presence of carbonate bauxites throughout Europe, and specifically in the Czech Republic, where there is a mine located in the centre of the country ('Bauxite - Czechoslovakia' in Czech Republic, Aluminum Occurrence," 2003). Another result of the reddish-brown colour could be due to the use of pozzolana brick within the mixture (Goins, 2004). Overall, further investigation is required to determine the exact cause of the pigment within the mortar binder. The elemental analysis of one area of the binder for the three samples can be seen below in Table 3.

Table 3 - Elemental Analysis of One Area of Binder for Samples 1, 2 and 3.

Elements	Sample 1	Sample 2	Sample 3
CaO	67.99	51.44	51.95
SiO_2	19.66	31.96	32.59
Al_2O_3	7.60	7.58	10.24
MgO	1.29	1.02	0.97
Na_2O	0.14	0.18	0.68
K_2O	1.03	2.68	0.85
SO_3	0.37	0.79	0.59
Cl	0.70	0.21	0.65
TiO_2	0.12	0.30	0.42
FeO	1.09	3.84	1.05
Total	99.99	100.00	99.99

With these results, the mortar was classified using the cementation index equation taken from (Oates, 1998) as shown below with results detailed in Table 4.

$$CI = \frac{(2.8\ x\ \%SiO_2) + (1.1\ x\ \%Al_2O_3) + (0.7\ x\ \%Fe_2O_3)}{\%\ CaO + (1.4\ x\ \%MgO)} \quad \text{(Equation 1)}$$

Table 4 - Cementation Index for Mortar Samples.

	Sample 1	Sample 2	Sample 3
Cementation Index	0.94	1.12	1.10

This can then be related to the characteristics of hydraulic lime tables found within the book "Lime and Limestone" by J.A.H. Oates. Table 5 details the information provided from (Oates, 1998),

Table 5 - Characteristics of Hydraulic Limes (Oates, 1998).

Parameter		Type / Classification of Hydraulic Lime		
		2	3.5	5
		Feebly	Moderately	Eminently
Compressive Strength (MPa)	28 day	2-7	3.5-10	5-15
Active Clay Minerals (% m/m)		< 12	12-18	18-25
Cementation Index		0.3-0.5	0.5-0.7	0.7-1.1
Setting Time in Water (Days)		< 20	15-20	2-4
Slaking Time		slow	slow	very slow
Expansion		slight	slight	slight

Comparing the cementation index of the samples with the table, the mortar can be classified as eminently hydraulic, which is also known as Roman Lime (Oates, 1998). Although the compressive strength after 28 days is shown to be 5-15 MPa within the table for eminently hydraulic mortars, it is known that the compressive strength of the existing mortar on site is much less due to the severe degradation of the mortar over the last 300 years. The level of degradation can be seen from the SEM images which show many voids and areas where crystals are not formed and fully connected throughout the binder. Constant weathering and freeze-thaw cycles forced the crystals within the mortar at the surface to constantly dissolve and recrystallize with time, leading to weak bonds and significantly lower strength properties of the mortar. This insight provides a reasonable explanation on why the mortar is very brittle and can be scratched off at the surface with a fingernail. Figure 25 provides a comparison between a fully crystallized area of the binder versus a sparsely crystallized area, due to the cumulative weathering of the material.

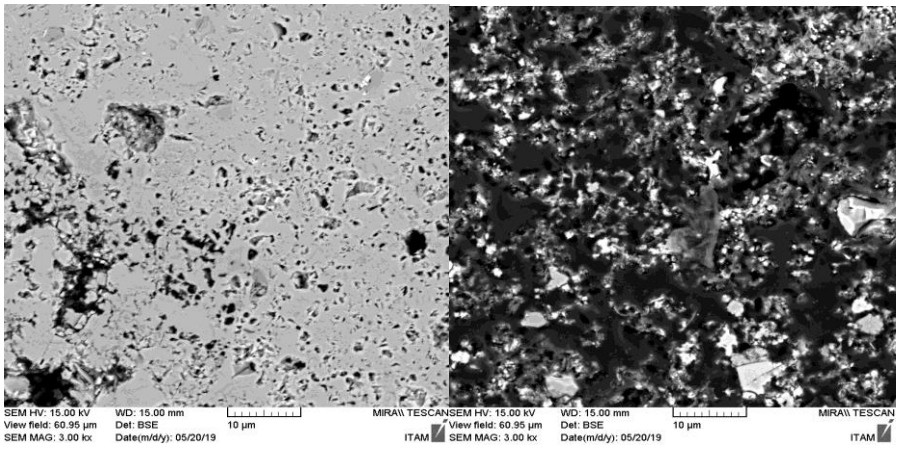

Figure 25 - Crystallized Binder Area (Left). Sparsely Crystallized Binder Area (Right).

Comparing to the research completed for various historic lime mortars found in (Válek & Veiga, 2005) and (Drdácký & Slížková, 2008), the SEM results for the mortar in this study do not provide a direct match, and cannot be used to provide an accurate estimate for the strength properties of the mortar.

3.3.2.2 POROSITY TEST

A porosity test was completed only on the sample from St. Barbara's Church as it was the only sample large enough to use for the test. Open porosity and pore size distribution were determined utilizing the mercury intrusion porosimetry technique with a porosimeter AutoPore IV 9500. Table 6 details the test results.

Table 6 - Porosity Test Results.

Parameter	Value	Units
Bulk Density (@ 0.51psi)	1.708	g/mL
Apparent (Skeletal) Density	2.514	g/mL
Porosity	32.067	%

3.3.2.3 SUMMARY OF MORTAR PROPERTIES

Due to the extremely limited number of samples collected, the results attained within this work may lead to inaccuracies in the overall properties. The inaccuracies could be further enlarged especially since the locations of the samples were from exposed surfaces on the external wall, an area directly effected by weathering, whereas the internal structure is not directly exposed to the elements. Therefore, using the data based a previous study completed for St. Ann's Church, see (Gajjar, 2018) and recommended material property values from (Lourenço, 2018), the properties for the mortar are proposed in Table 7.

Table 7 - Properties of Natural Hydraulic Lime Mortar.

Material	Unit Weight (kN/m3)	Youngs Modulus, E (GPa)	Poissons Ratio, v	Compressive Strength, f_c (MPa)	Tensile Strength, f_t (MPa)	Tensile Fracture Energy, G_f (N/m)	Peak Comp. Strain, ε (‰)
Lime Mortar	17.0	0.126	0.17	1.5	0.1	10	1.2

In the future, it is recommended that the SEM results be investigated further and if possible, a greater number of larger, more coherent pieces of mortar samples are collected to allow for a more accurate determination of properties with tests such as wet chemical analysis, water absorption, X-ray diffraction, sieving, apparent density test, porosity test, hardness test, and possibly even a compressive strength test (Válek & Veiga, 2005), (Goins, 2004).

3.3.3 SUMMARY OF MATERIAL PROPERTIES

The material properties that will be used in the upcoming micro-modelling analyses can be found in Table 8.

Table 8 - Summary of Material Properties.

Material	Unit Weight (kN/m3)	Youngs Modulus, E (GPa)	Poissons Ratio, v	Compressive Strength, f_c (MPa)	Tensile Strength, f_t (MPa)	Tensile Fracture Energy, G_f (N/m)	Peak Compressive Strain, ε (‰)
Lime Mortar	17.0	0.126	0.17	1.5	0.10	10	1.2
Ignimbrite	21	9.49	0.2	42	4.2	60	1.5
Yellow Sandstone	21	7.51	0.2	29	2.9	35	1.5
Fine-Grained Red Sandstone	21	9.21	0.2	48	4.8	40	1.5
Light Sandstone	21	8.50	0.2	45	4.5	40	1.5
Red Sandstone	21	5.41	0.2	38	3.8	40	1.5

3.4 MULTI-SCALE MODELLING APPROACH

Due to the highly irregular geometry and varying size of stones within the structure, it was determined that the finite element meshing of the complete geometry of the 1 m x 1 m wall panels under study was unfeasible due to the limited computational power and available time. Recalling the results from the statistical analysis, the cumulative density function constructed showed over 50% of the stone elements were less than 0.001 m² in size, and this value increased to 68% when looking at stones sized less than 0.002 m². Furthermore, these stone elements are also thought to be small enough in size that they would not continue into the wall along the full depth of the first leaf (0.5 m) and can be classified as small stones found throughout the mortar.

Thus, to increase efficiency of the analysis, a multi-scale modelling approach was used, where the small stones were grouped in with the mortar and treated as a matrix component with homogenized properties within 1 m x 1 m models on a mesoscale-level. Separate models were built on a microscale-level to characterize the matrix, using test-windows placed in randomly generated, statistically equivalent morphologies in which only the small stones and mortar were represented. For clarity moving forward, the 1 m x 1 m models of masonry with large stones embedded in the matrix component will be referred to as the meso-scale models, and the models representing the matrix consisting only of small stones and mortar will be referred to as micro-scale models.

The overall properties of both the micro-scale and meso-scale models were obtained by adopting an engineering approach to simulate experimental testing, meaning the models were simply supported and prescribed uniform displacements were applied along one of the edges. The micro-scale models were tested in uniaxial compression and uniaxial tension to obtain statistical distributions for four main properties, namely Young's modulus (E), compressive strength (f_c), tensile strength (f_t),

and fracture energy (G_f). For the meso-scale models, only the overall stiffness (E) and compressive strength were determined by simulating uniaxial compression tests.

For the analysis of the meso-scale models, two types of calculations were done. First, the matrix was assigned uniform properties using the mean values obtained from the micro-scale models. Secondly, considering the high variability and inhomogeneity of the matrix component, random fields were utilized in the meso-models to describe this variability. The parameters for the random fields were taken from the statistical distributions of the properties gained from the micro-scale models and the autocorrelation length was set to match the micro-scale model sizes. Furthermore, the multi-scale study was performed for two different threshold sizes defining the small stones: either stones with projected area less than 0.001 m² or 0.002 m² were represented in the micro-scale model. An overview of the different levels envisioned for the multi-scale modelling procedure can be seen in Figure 26 and Figure 27.

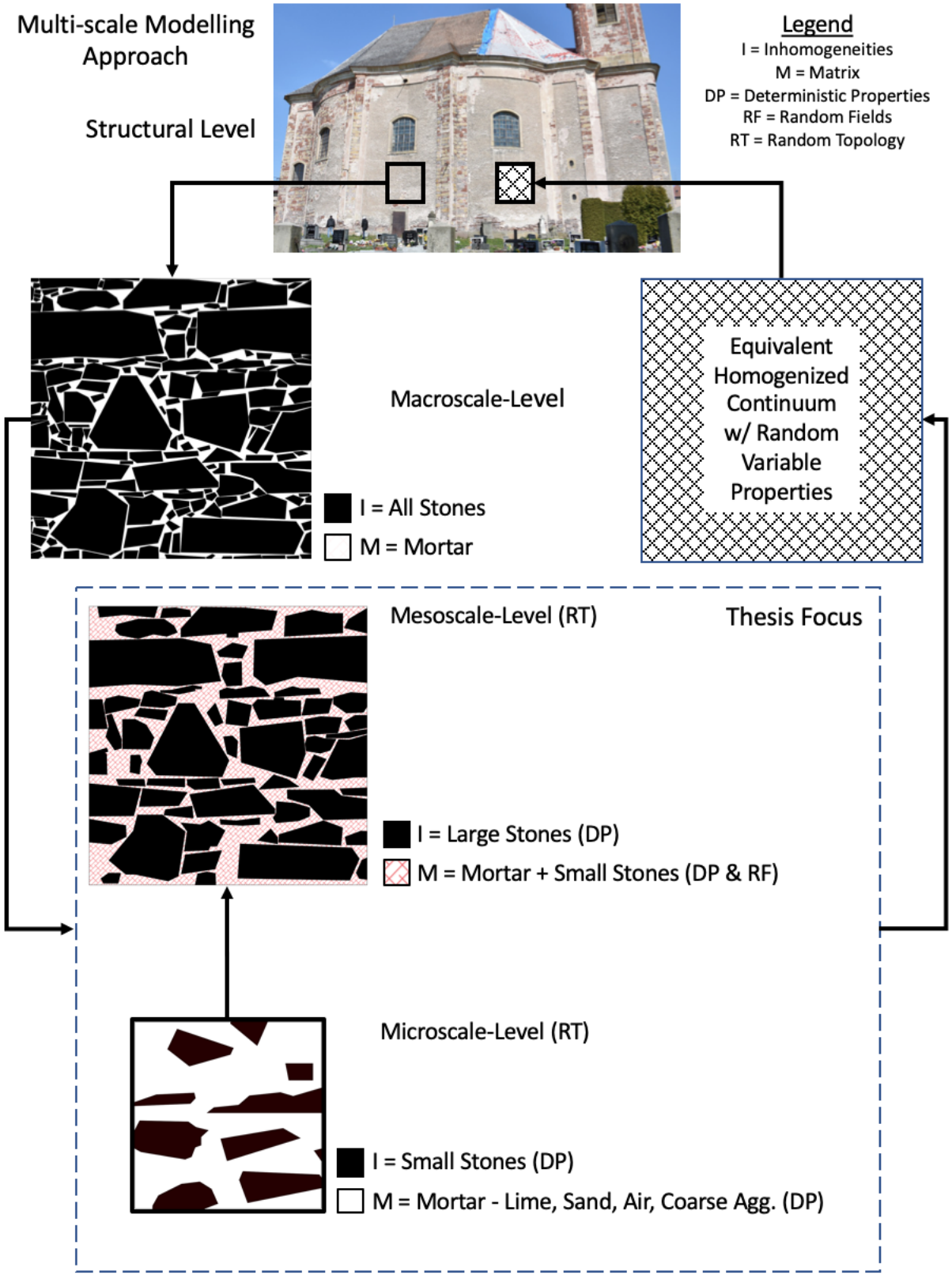

Figure 26 - Overview of Modelling Procedure (1/2)

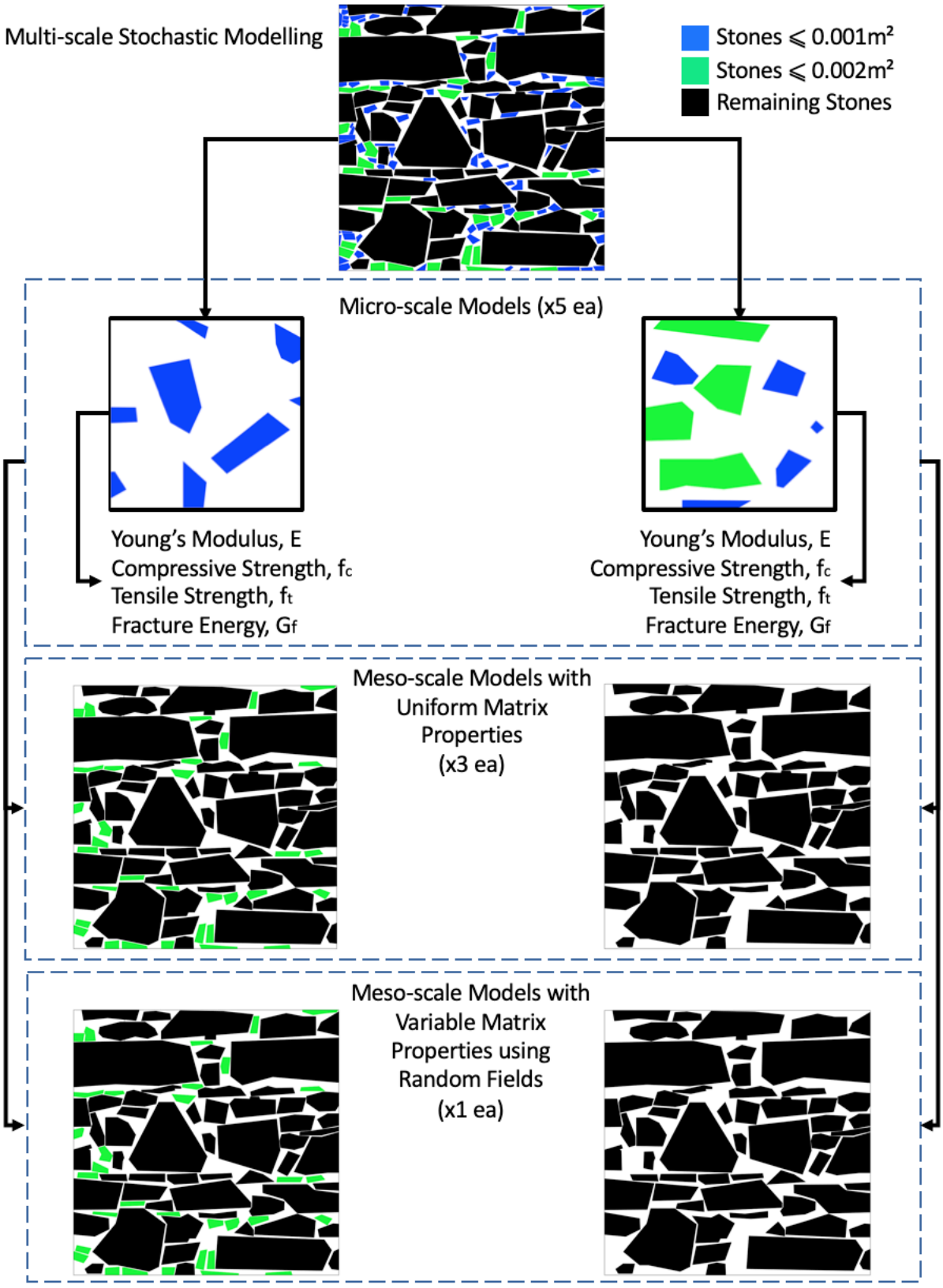

Figure 27 - Overview of Modelling Procedure (2/2)

3.4.1 MODELLING PARAMETERS & MATERIAL CONSTITUTIVE MODELS

Modelling and non-linear analysis of the 2D sections were completed utilizing ATENA Science Finite Element Software in addition to GiD, a user-friendly graphical interface used for the preparation of input data for the analysis in ATENA. Idealized 2D plane stress models were used to automatically redistribute internal forces based on the formation of cracks to represent true behavior of the structure. Material non-linearity was considered by incorporating the low tensile strength as well as the crushing compressive strength of the materials, and geometrical non-linearity was considered by incorporating the non-linear effects due to deformed geometry after each iteration. To simulate experimental testing and assess the uniaxial compressive and tensile behaviour of the masonry, the models were simply supported with only one corner node pinned to avoid any translations. Additionally, loads were applied in steps of prescribed displacement to develop the non-linear behavior of the material. The size of the steps solely depended on the ability to achieve numerical convergence, and thus varied for each model. Although there is finite amount of friction between the unit-mortar interface that would enable sliding, the interfaces are expected to be quite rough and were therefore rigidly modelled to ensure simplicity and enhance the probability of numerical convergence.

The solution parameters remained on the default settings for ATENA Science, although the Newton-Raphson method was enhanced with the arc-line and line search methods to complete the analysis along with an energy error convergence tolerance of 10^{-4}. Triangular elements were utilized for the mesh generation as they are much more flexible during finite element calculations and can lead to a higher probability of convergence.

Since masonry is a quasi-brittle material, a fracture-plastic constitutive model was utilized in ATENA Science called “3D Non-linear Cementitious 2”. The idealized model combines tensile and compressive behavior of the material and can be used to simulate material cracking, crushing under confinement, and crack closing due to crushing. The fracture model is based on the smeared crack method and crack band model which averages the strain over an element. The model uses the Rankine failure surface with exponential softening in tension and the Menétry-William failure surface for hardening and softening in compression. The material model allows for calculations to continue when failure surfaces of both models are active and when events such as crack closure occur (Červenka, Jendele, & Červenka, 2018). Figure 28 details the biaxial failure function and uniaxial stress-strain model incorporated into the model.

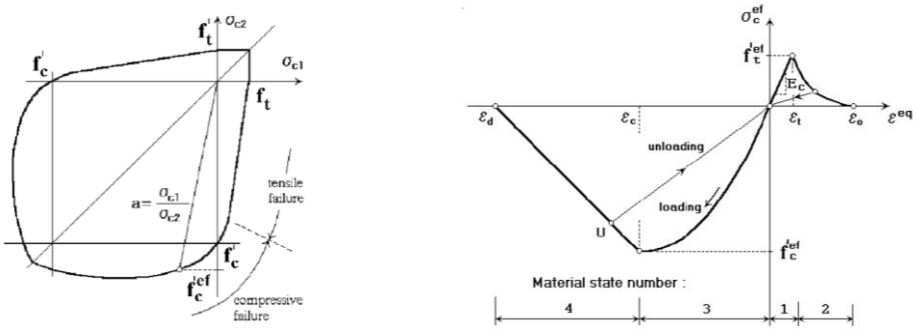

Figure 28 - Biaxial Failure Function (Left). Uniaxial stress-strain law (Right). (Červenka et al., 2018).

A fixed crack model will be used for all models, which couples the direction of the crack with the direction of principal stress at crack initiation and will be fixed during further loading. Figure 29 illustrates the fixed crack model taken from the ATENA manual.

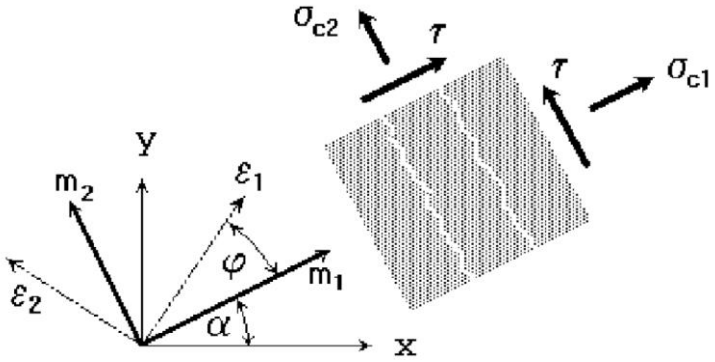

Figure 29 - Fixed Crack Model (Červenka et al., 2018).

For cracking after tension, a fictitious crack model based on a crack-opening law and fracture energy used in combination with the crack band is incorporated to suitably model crack propagation. In the formula used, w is the crack opening, w_c is the crack opening at the complete release of stress, G_f is the fracture energy needed to create a unit area of stress-free crack and f_t is the effective tensile strength. Figure 30 details the crack opening law taken from the ATENA theory manual (Červenka et al., 2018).

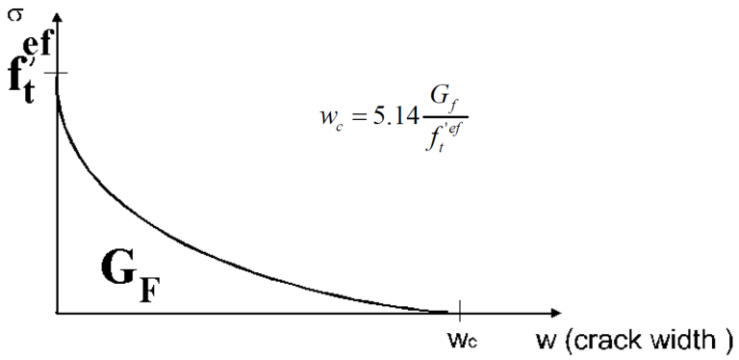

Figure 30 - Exponential Crack Opening Law (Červenka et al., 2018).

To ensure this constitutive model was suitable for the materials, a quick check was done using the tensile strength and fracture energy of the mortar. The max crack opening was calculated to be 0.5 mm, approximately half of the size of the largest coarse aggregate found in the mortar, which is thought to be sufficient for the modelling the mortar.

3.4.2 MICRO-SCALE MODELS

The matrix component consists exclusively of mortar and small stones and therefore represents an area that could not be directly extracted using an RVE method. Therefore, micro-scale models were constructed using a randomly generated, statistically equivalent morphology of mortar and small stones. This morphology was created by taking all stones of sizes with area less than 0.001 m² from the 6 panels analyzed earlier on and putting them into the statistically equivalent area of mortar. By taking the stones directly from the wall panels analyzed, the true size and aspect ratio of the stone elements were statistically met. The total size of the statistically equivalent domain was 1.18 m x 1.18 m, with the mortar taking up 84% of the area and the stones taking up 16% of the area. The statistical analysis of the wall panels used to determine the statistically equivalent morphology can be seen in Table 9.

Table 9 - Area of Stones ≤ 0.001 (m²) Analysis

Wall Panel	Area of Stones (%)	Area of Mortar (%)
Wall 1	15%	85%
Wall 2	10%	90%
Wall 3	18%	82%
Wall 4	18%	82%
Wall 5	15%	85%
Wall 6	22%	78%
Mean	16%	84%
St. Dev	4%	4%
COV (%)	23%	5%

From there, the stones were randomly scattered within the domain utilizing the “SCATTER” function in AutoCAD. Any stones that were shown to be overlapping were manually moved. Rectangles were then made and randomly placed using the same scatter function to produce test windows. The size of the test windows was set at 0.1 m x 0.1 m to ensure it was at least 3 times the size of the largest stone dimension found within the mortar. Since the fabricated morphology captures the complete substrate within; the smaller test-windows encompass the variation in overall properties which is realistic since no part of masonry includes that size of microstructure. It is recommended a more rigorous analysis of micro-scale test windows are completed, but due to time constraints only 5 windows were made to test the concept. The complete statistically equivalent morphology and test windows can be seen in Figure 31.

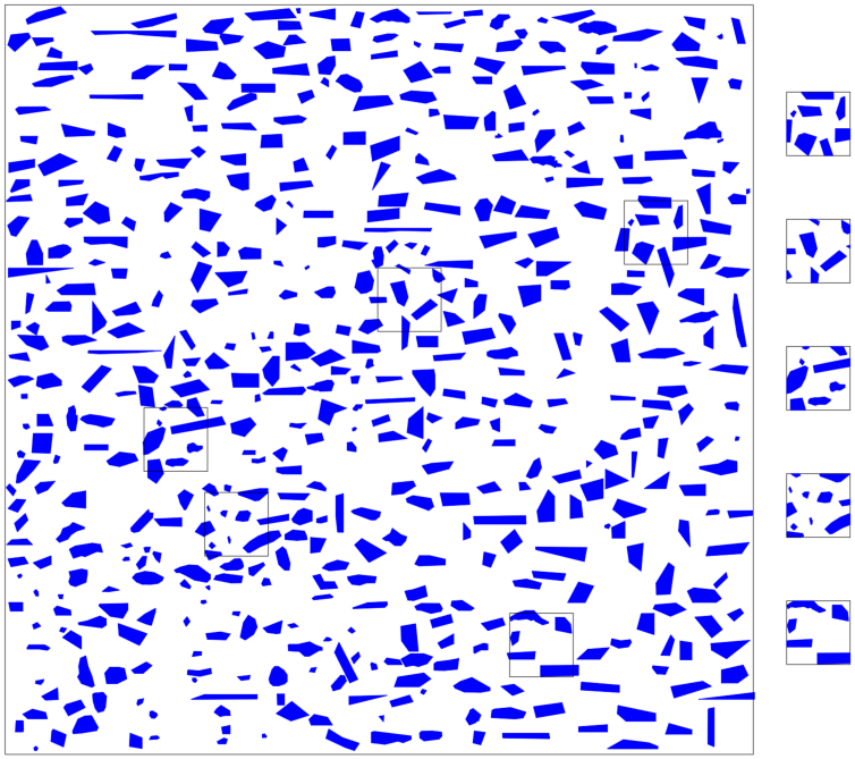

Figure 31 - Statistically Equivalent Morphology (Left). Test Windows (Right) for Stones ≤ 0.001 m².

In a similar fashion, a statistically equivalent morphology and test windows for stone sizes less than 0.002 m² were completed and modelled. The test windows were set to be 3 times the size of the largest stone dimension found within the mortar, therefore be 0.15 m x 0.15 m. Statistical analysis of the wall panels used to determine the statistical equivalent morphology can be seen in Table 10 and Figure 32 illustrates the randomly generated, statistically equivalent morphology and test windows for stones sizes less than 0.002 m².

Table 10 - Area of Stones ≤ 0.002 (m²) Analysis

Wall Panel	Area of Stones (%)	Area of Mortar (%)
Wall 1	32%	68%
Wall 2	21%	79%
Wall 3	31%	69%
Wall 4	33%	67%
Wall 5	28%	72%
Wall 6	34%	66%
Mean	30%	70%
St. Dev	5%	5%
COV (%)	15%	7%

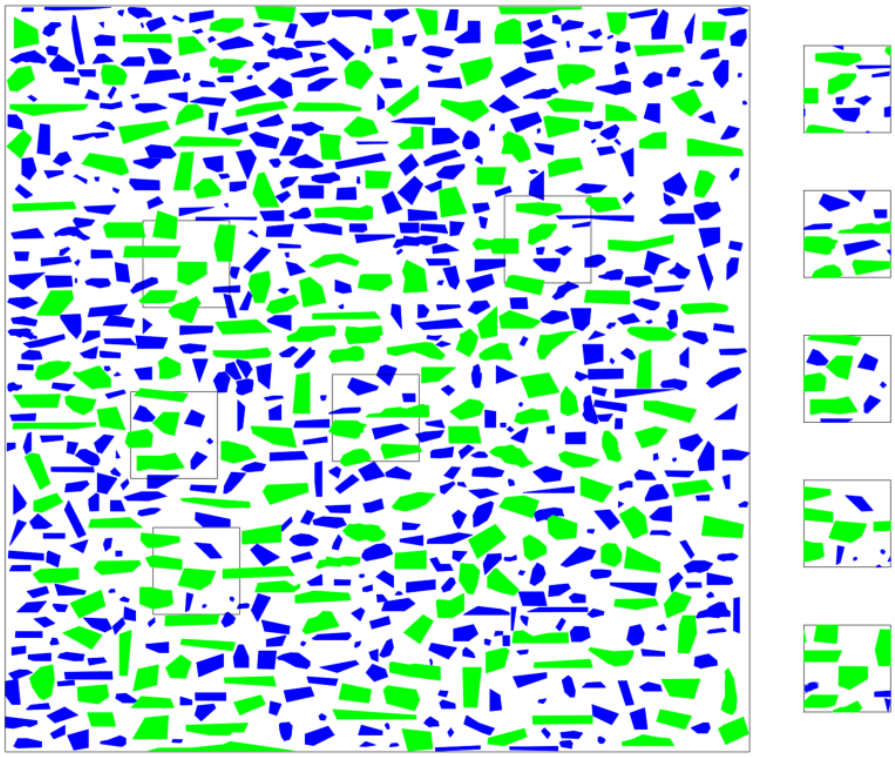

Figure 32 - Statistically Equivalent Morphology (Left). Test Windows (Right) for Stones ≤ 0.002 m².

The models were set up as described in Section 3.4.1 and tested under uniaxial compression and tension to gain information on Young's modulus (E), compressive strength (f_c), tensile strength (f_t), and fracture energy (G_f). An example of the models constructed in GID, along with mesh size 0.005 m and set boundary conditions, applied displacements, and monitors can be seen in Figures 33 and 34. The methodology and associated equations used to determine the homogenized properties of the micro-scale models are summarized in Figure 35.

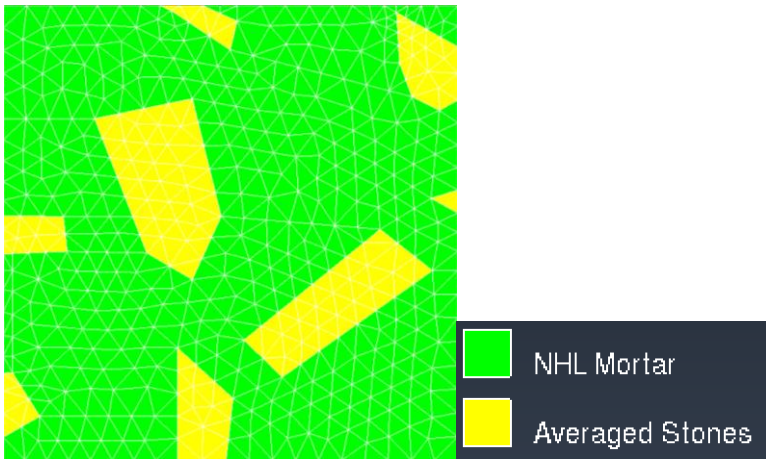

Figure 33 - Micro-scale Model 1 and Generated Mesh (Sized 0.005m).

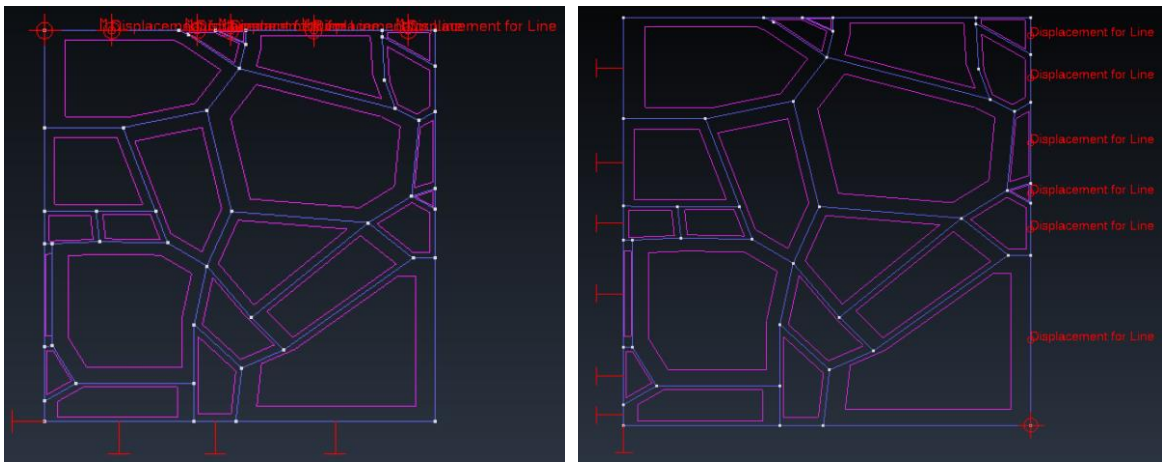

Figure 34 - Set Conditions for Micro-scale Models. Compression Test (Left) and Tensile Test (Right).

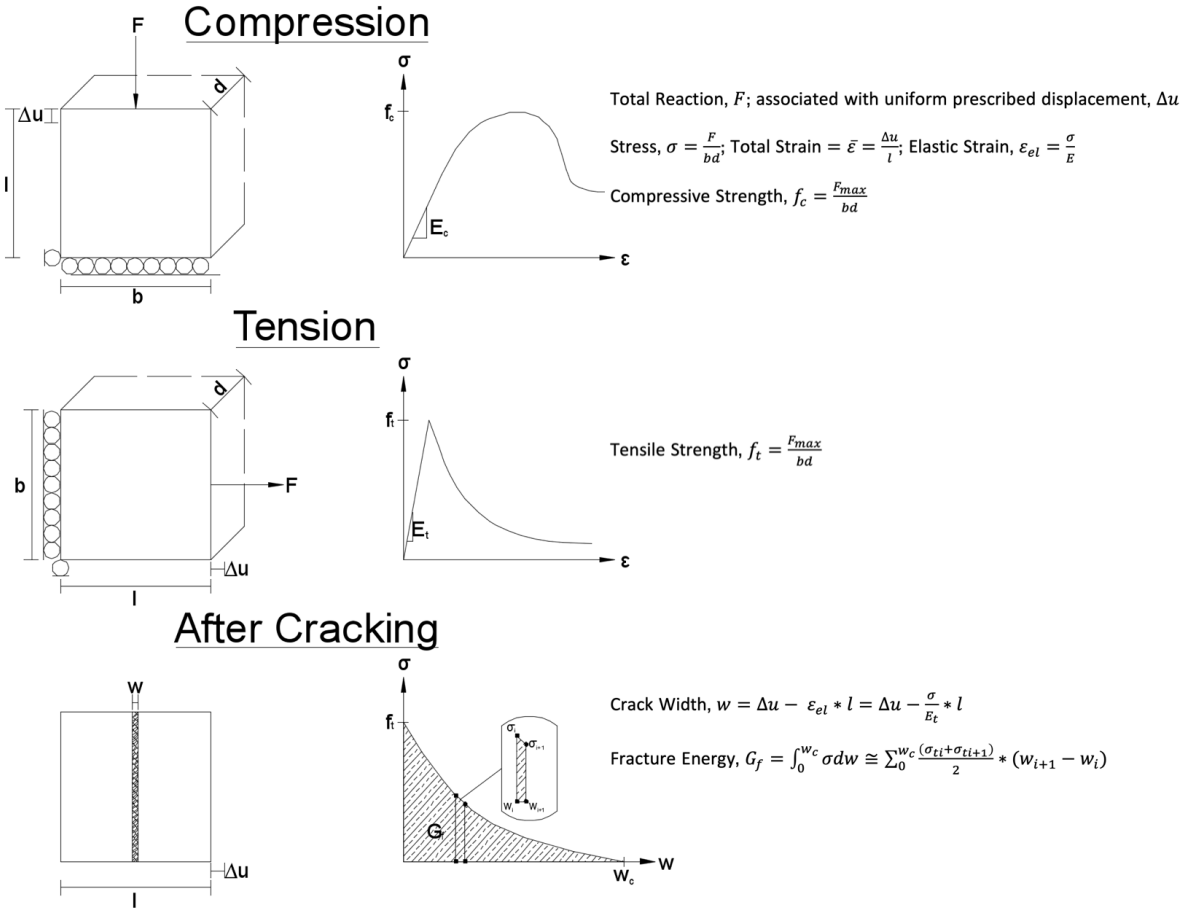

Figure 35 - Methodology for Calculating Homogenized Properties of Matrix Component.

3.4.3 MESO-SCALE MODELS

3.4.3.1 MESO-SCALE MODELS WITH UNIFORM MATRIX PROPERTIES

Once the analyses of the micro-scale models were complete, meso-scale models were constructed which consisted of large stones embedded in a matrix component with uniform properties. The meso-scale models were constructed directly from the 1 m x 1 m wall panels analyzed earlier on, since they encompass a size 3 times the area of the largest stone. The models were tested under uniaxial compression using simply supported boundary conditions and prescribed displacements as previously described. No uniaxial tensile tests were performed on the meso-scale models due to time constraints. The mean values for the homogenized properties obtained from the micro-scale models were input into the properties of the matrix for the meso-models. Two types of meso-scale models were created, one with a matrix consisting of mortar and stone sizes less than 0.001 m² and another with a matrix consisting of mortar and stone sizes less than 0.002 m². Figures 36 -39 depict the models constructed in GID, along with set boundary conditions and generated mesh size using 0.01 m triangular elements.

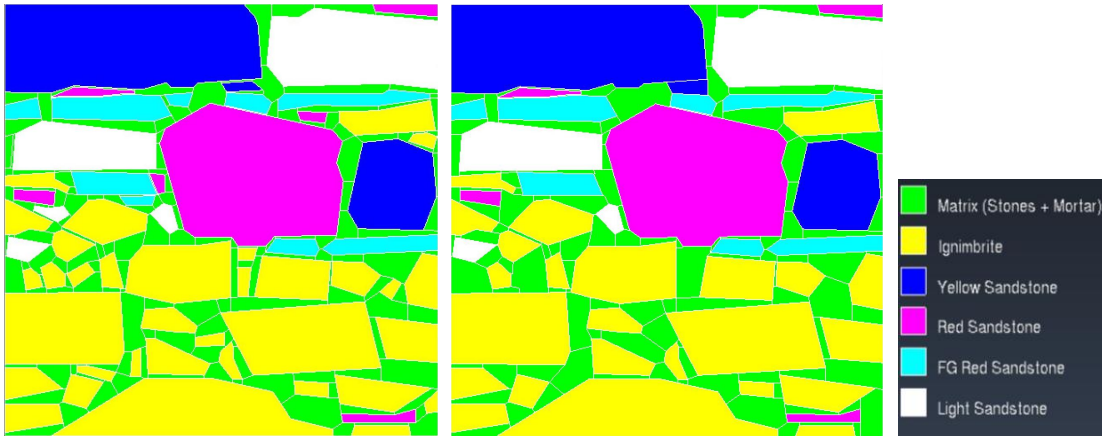

Figure 36 - Meso-scale Model 1. Matrix w/ Stones ≤ 0.001m² (Left). Matrix w/ Stones ≤ 0.002 m² (Right).

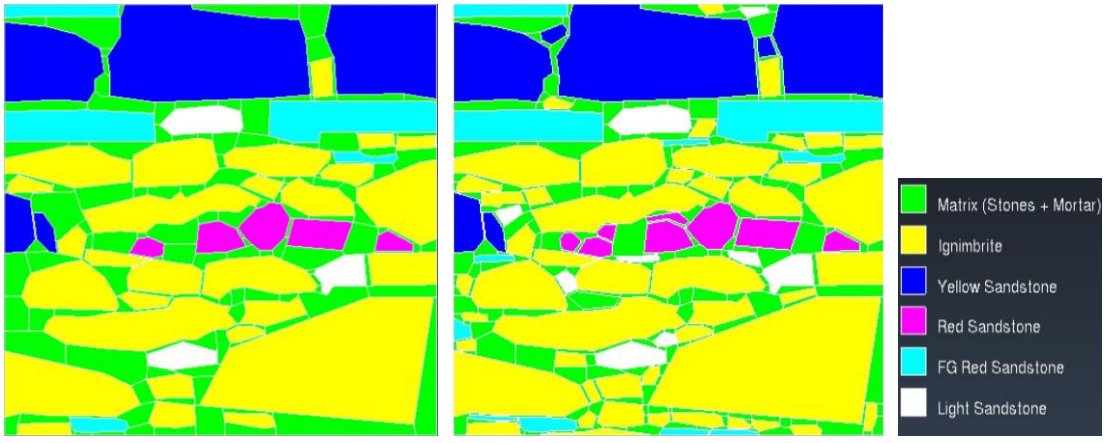

Figure 37 - Meso-scale Model 2. Matrix w/ Stones ≤ 0.001 m² (Left). Matrix w/ Stones ≤ 0.002 m² (Right).

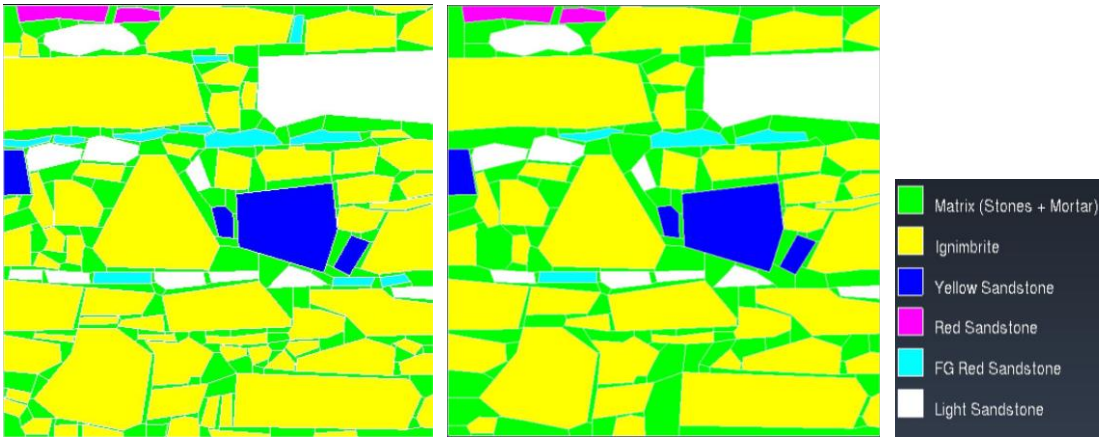

Figure 38 - Meso-scale Model 3. Matrix w/ Stones ≤ 0.001 m² (Left). Matrix w/ Stones ≤ 0.002 m² (Right).

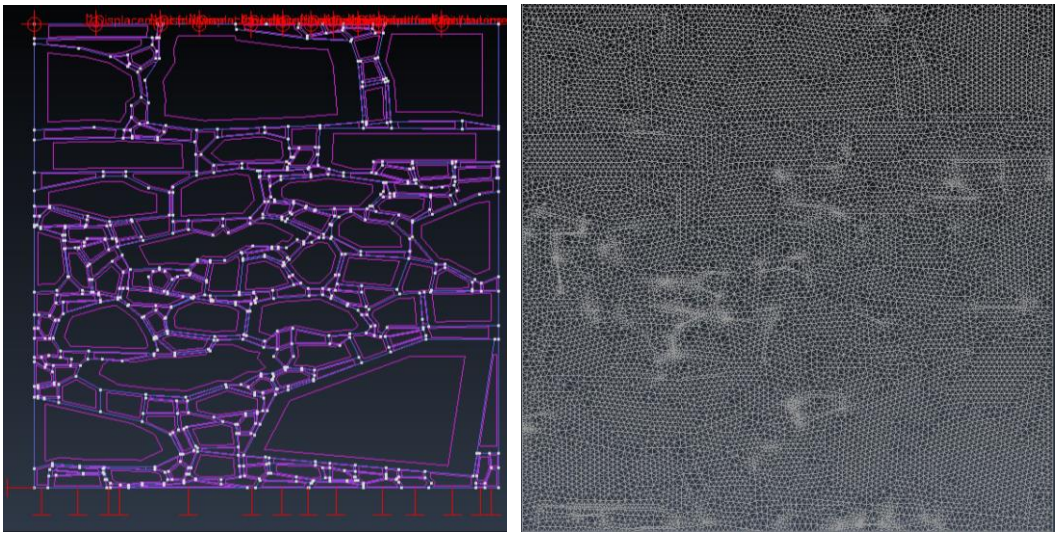

Figure 39 - Meso-scale Model 2. Set Conditions (Left). Generated Mesh (Sized 0.01m) (Right).

3.4.3.2 MESO-SCALE MODELS UTILIZING RANDOM FIELDS

To capture the variability in the homogenized properties of the matrix component obtained from the micro-scale modelling analysis, random fields were utilized to define the matrix properties and used to reanalyze both types meso-scale models. The random field parameters were defined by taking the mean and standard deviation of the values for the homogenized properties found from the micro-scale modelling analysis. The autocorrelation length, which defines the level of variability of the properties in space, was set to match the test window size of the micro-scale models studied. Therefore, for the matrix including stones less than 0.001 m² in size, the autocorrelation length was set to 0.1 m in the x and y direction. Similarly, for the matrix including stones less than 0.002 m² in size, the autocorrelation length was set to 0.15 m in the x and y direction. By setting the autocorrelation length in this way, the random fields are believed to encompass the statistical distribution of the properties found within the micro-scale models and match the spatial distance in which the small stones appear in the mortar.

Once these parameters were set, FREET was used to generate the stochastic variation of the properties used to define the random fields. The Latin hypercube sampling method was used to generate the random fields for each of the properties, which were then visually generated within the program. In total, 5 random fields were generated for the matrices of both types of meso-scale model. An example of a random field generation for the material properties E, f_c, f_t, and G_f can be seen in Figures 40-41.

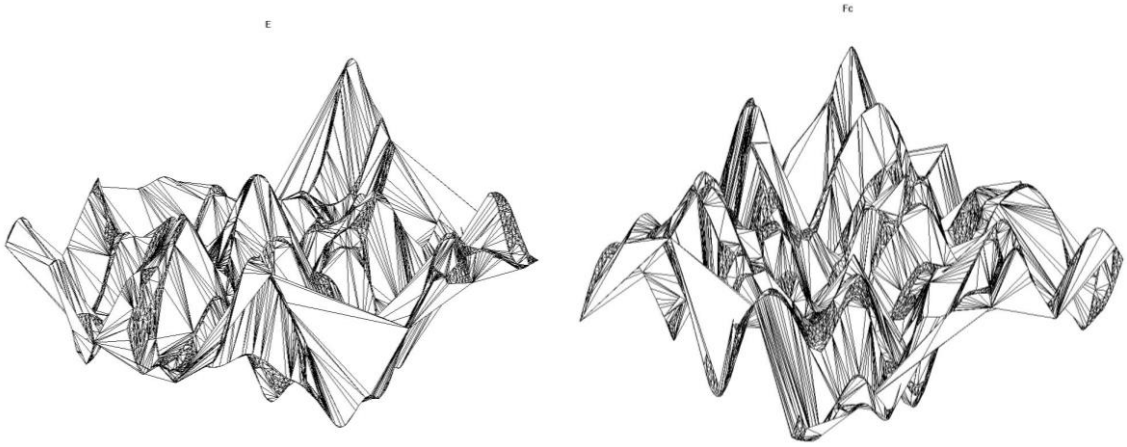

Figure 40 - Random Fields Generated for E and f_c in FREET.

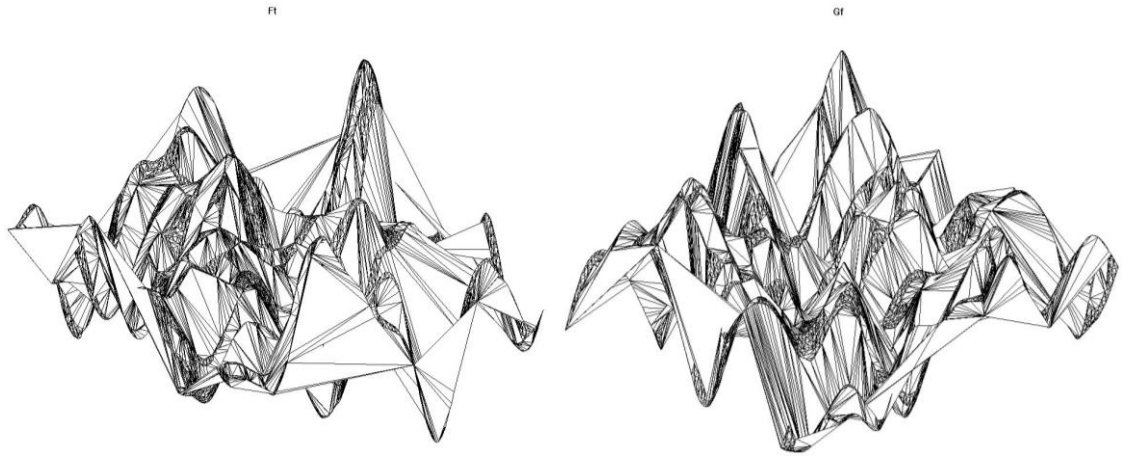

Figure 41 - Random Fields Generated for f_t and G_f in FREET.

Once the random field files were produced and validated using the visualizations in FREET, they were linked to the models in ATENA Science through a reference in the input file, and the analyses were run for each of the simulations. The generated random fields could then be visualized for each of the material properties using the post-processing interface within ATENA Science and allowed for a clear analysis of the effect of the distribution of the matrix properties on the overall compressive strength of the masonry. Due to time constraints, only one meso-scale model was analyzed with random fields.

4. RESULTS

The results from the application of the methodology described in the previous will be presented and discussed within this section. The focus of this section is on the homogenized properties and variability gained from the micro-scale models and their subsequent application to the meso-scale models, first with uniform matrix properties and then with variable matrix properties utilizing random fields.

4.1 MICRO-SCALE MODELS

For compressive strength, the micro-scale models were analyzed by comparing contour plots for crack width and equivalent plastic strain to determine failure modes before and after the peak stress was reached. The equivalent plastic strain was used to verify plastic yielding in compression. If there was a major jump in crack width without any increase in equivalent plastic strain, then the failure was categorized as tensile splitting. If the equivalent plastic strain was reached, then compressive failure occurred due to crushing. The deformed shape was also analyzed to help determine if tensile splitting played a major role in failure. For tensile strength, the micro-scale models were analyzed using contour plots for crack width to illustrate the developed cracking locations. The failure mode and stress-strain plot for compression and tension for micro-scale model 1 can be seen in Figures 42-47. For a detailed look at each of the micro-scale models and failure modes, see Appendix C.

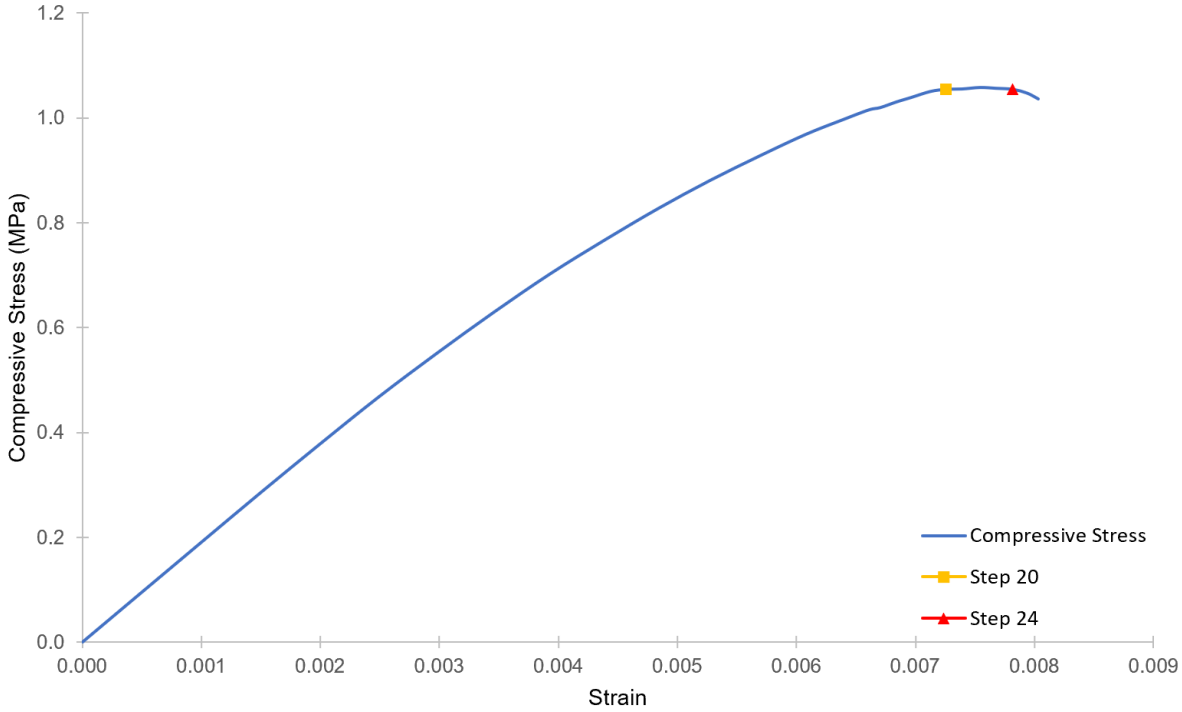

Figure 42 - Micro-scale Model 1 Compressive Stress vs Strain Diagram.

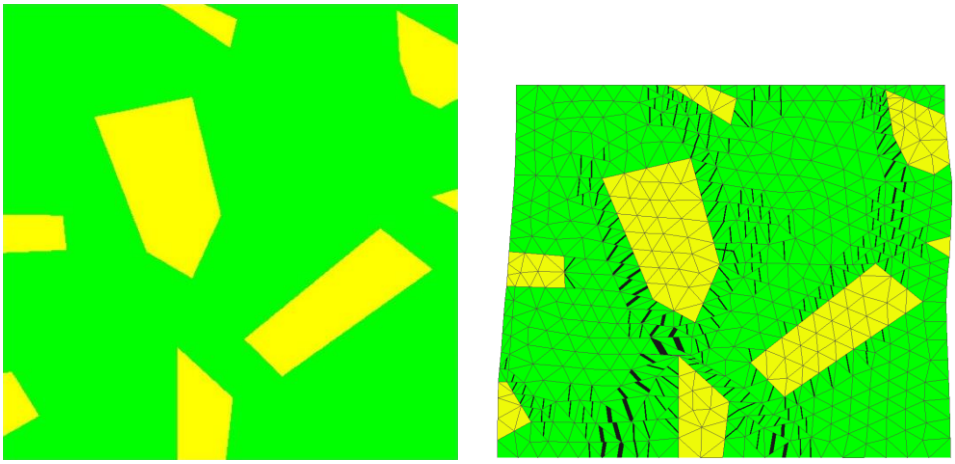

Figure 43 - Micro-Scale Model 1 Geometry (Left) and Final Deformed Shape with Cracks (Right).

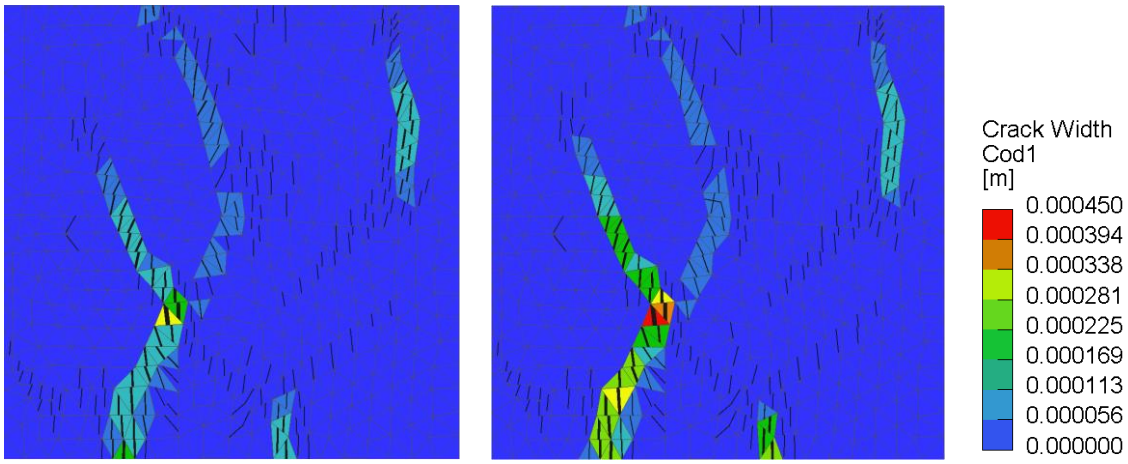

Figure 44 - Micro-scale Model 1 Crack Width: Step 20 (Left) at Step 24 (Right).

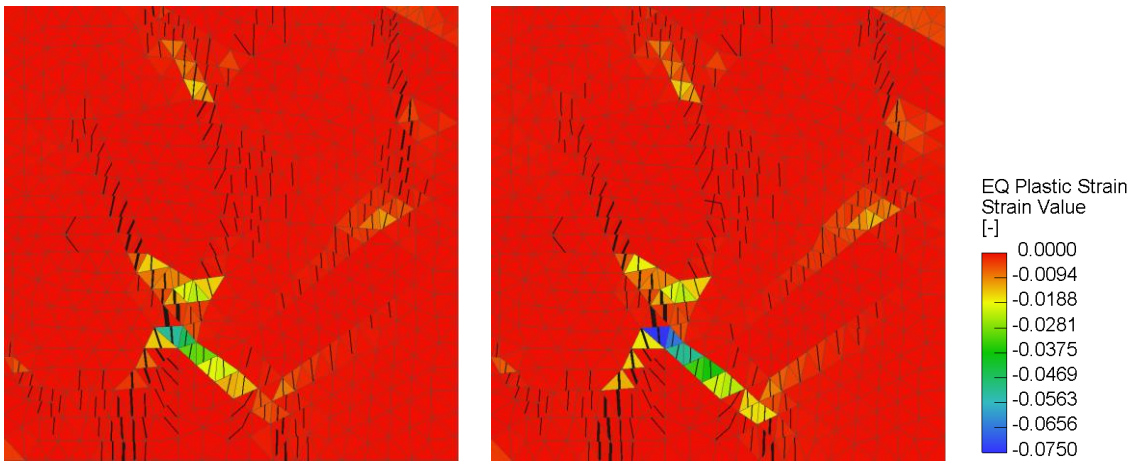

Figure 45 - Micro-scale Model 1 Equivalent Plastic Strain: Step 20 (Left) at Step 24 (Right).

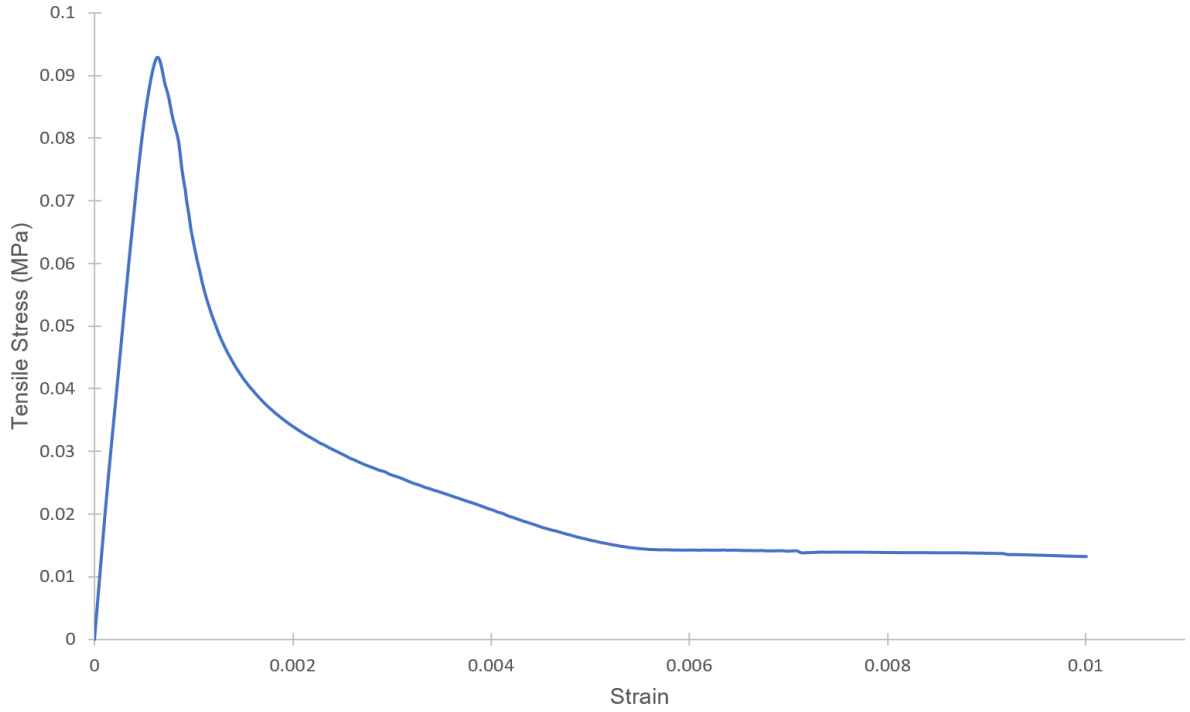

Figure 46 - Micro-scale Model 1 Tensile Stress vs Strain Diagram.

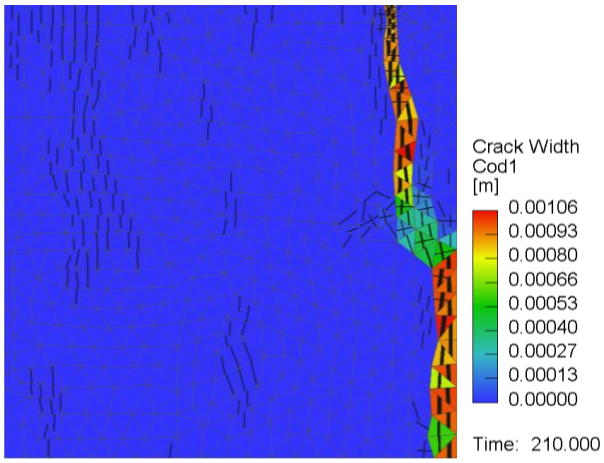

Figure 47 - Micro-scale Model 1 Crack Width under Uniaxial Tension.

As can be seen in the above figures and graphs, the formation of cracks initiated the non-linear behaviour of the material. Overall, the cracks and stresses were shown to be concentrated in the weakest material, being the mortar in this case.

For the compressive tests, failure seems to have occurred due the combination of compressive crushing and tensile splitting. Since the models were unrestricted along the vertical axes, they compressed in the vertical direction and expanded in the horizontal direction, which led to the formation of either one or multiple tensile splitting cracks in the mortar. Futhermore, although crushing

occurred in the mortar locally, the model underwent hardening since the overall strain was less than the peak compressive strain set for the mortar. The highest compressive stresses were observed in models where cracks matched up with the areas of high plastic strain. Figure 48 details the post-peak contour plots for crack width and plastic strain of micro-scale model 2, which was shown to have the highest compressive strength of the set.

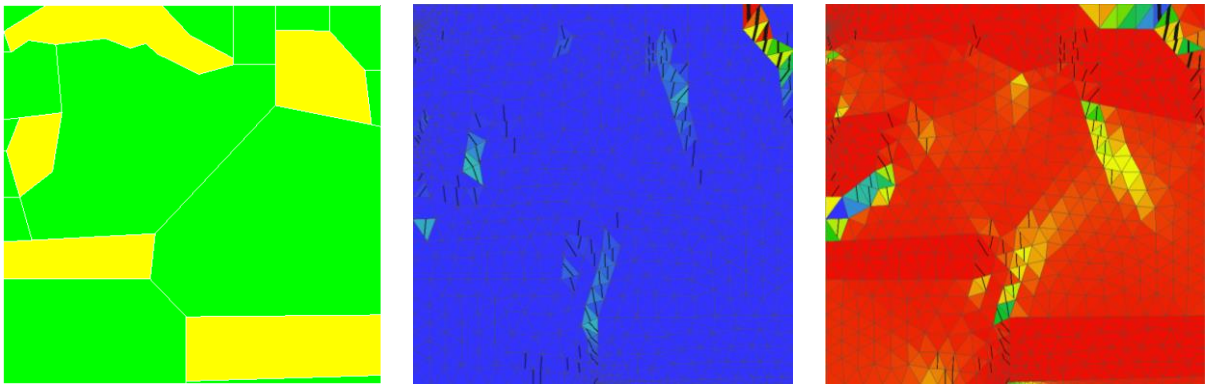

Figure 48 - Micro-scale Model 2 Geometry (Left), Crack Width (Centre), Equivalent Plastic Strain (Right).

For the tensile tests, failure was caused by a crack that formed in the mortar which developed along the easiest path around the stones to form a full crack across the whole model. Therefore, the model having a tensile strength close to that of the mortar is reasonable. High fracture energies correlated to extremely tortuous cracks and which was especially true for models where 2 cracks form. The formation of 2 cracks effects the fracture energy as it is calculated based on the assessment of a single crack. Since the results will be used for a smeared crack model which assumes the fracture is smeared over a characteristic length and crack band, this will be concentrated back into a single crack on the meso-scale models and was thus assumed to be reasonable to use. See Figure 49 detailing tensile failure for micro-scale model 2 and 5, which have the highest fracture energies of the set. Figures 50-52 plot the compressive stress and tensile stress versus the strain and crack-width for each of the micro-scale model tests performed.

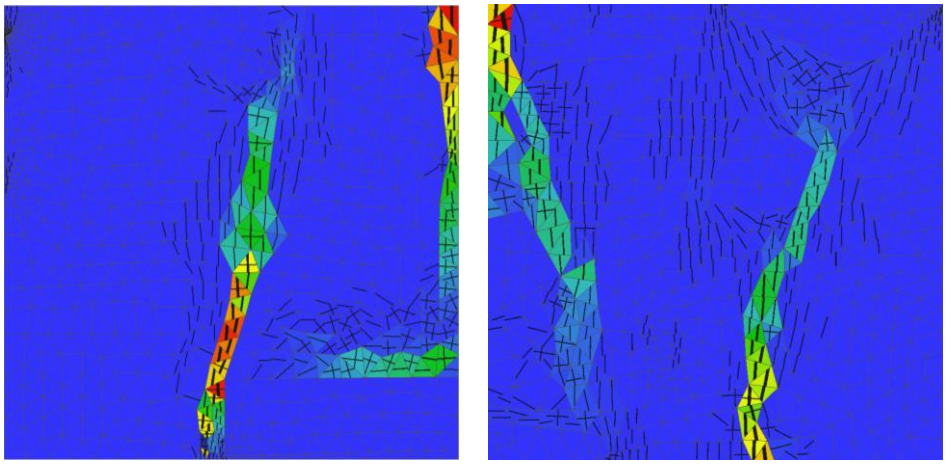

Figure 49 - Tensile Failure for Micro-scale Model 2 (Left) and Micro-scale Model 5 (Right).

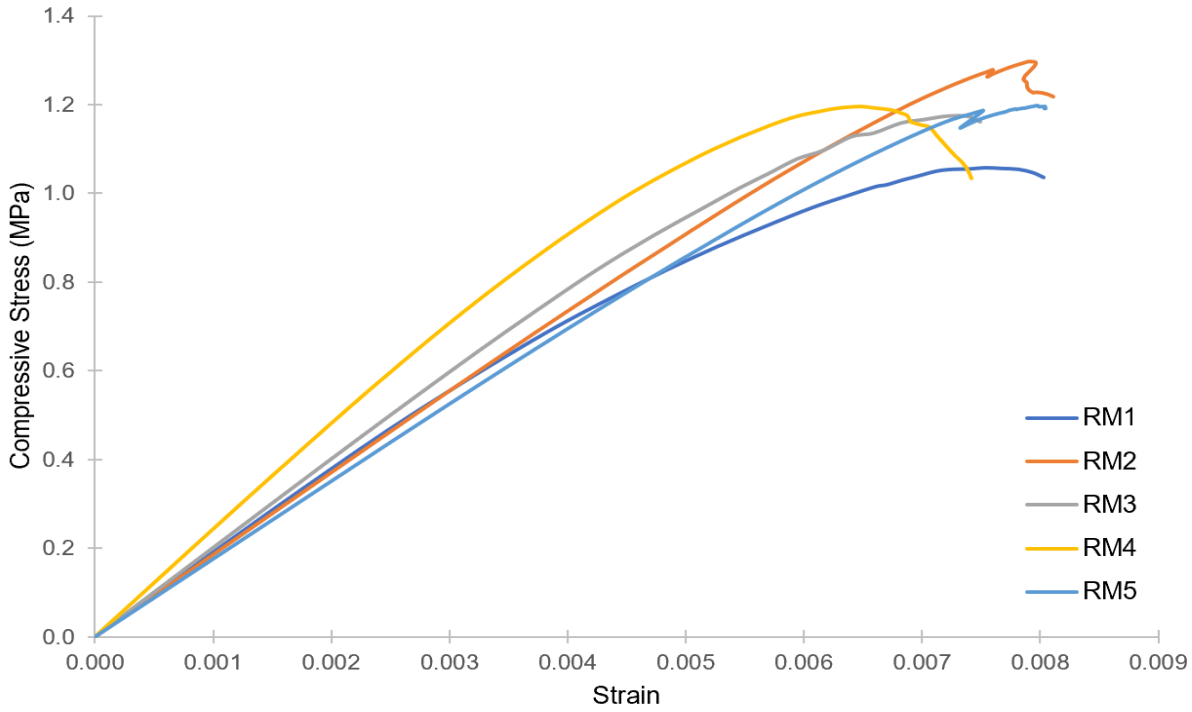

Figure 50 - Compressive Stress vs Strain for all Micro-scale Models with Stones ≤ 0.001 m².

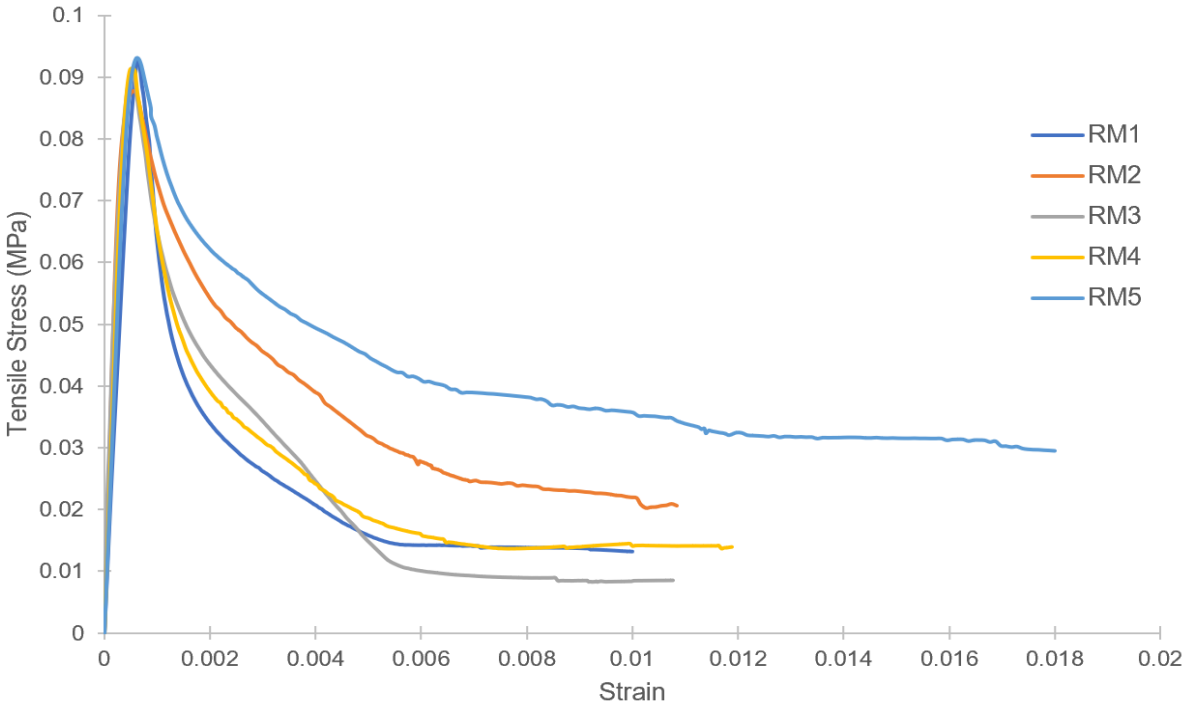

Figure 51 - Tensile Stress vs Strain for all Micro-scale Models with Stones ≤ 0.001 m².

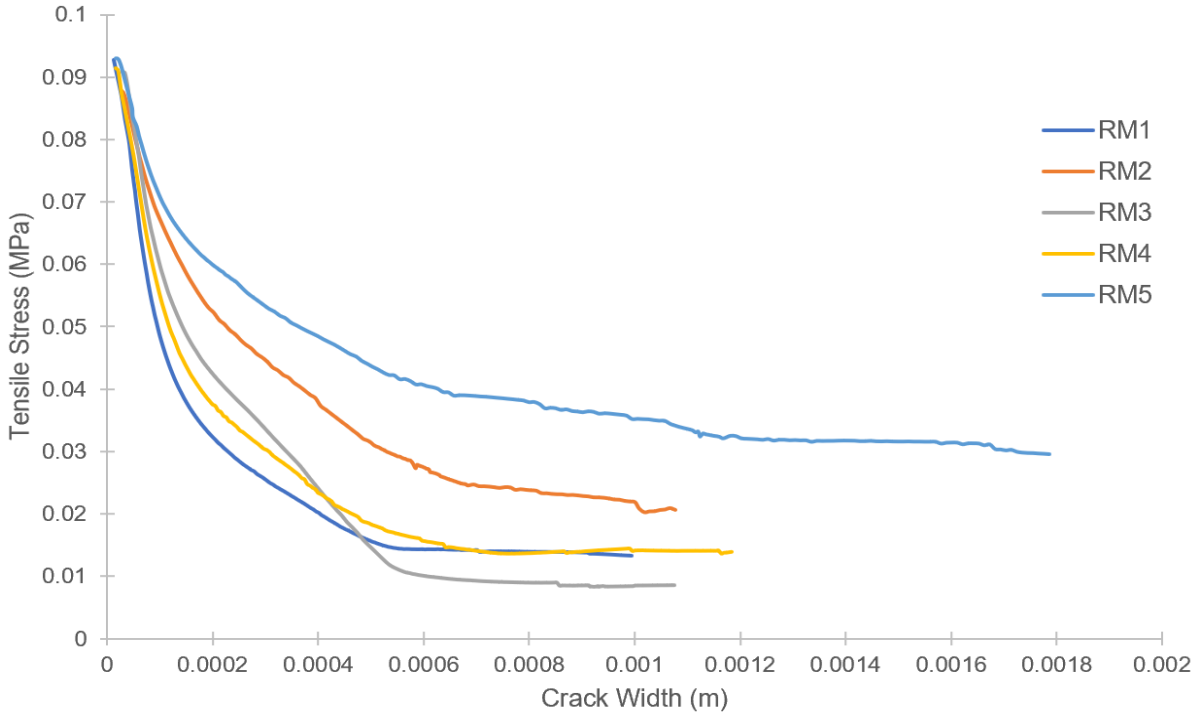

Figure 52 - Tensile Stress vs Crack Width for all Micro-scale Models with Stones ≤ 0.001 m².

As can be seen from the above graph for tensile stress versus crack width, all models do not reach the same crack width due to convergence issues, which posed a problem when trying to compare fracture energies. Therefore, for the calculation of the fracture energy, the decision was made to cut off all calculations at 0.001 m since this was the largest value for which all models converged to and is at the tail end of the curves, the point at which they begin to go flat. The long tail of the curves is due to numerical stiffness, which is a by-product of the finite element method. While the new value is not considered to be the full fracture energy, it was assumed that the remaining part of the tail is small, and its exclusion would not alter the results significantly. Furthermore, due to the convergence issues the curves for tensile stress versus crack width do not continue to a zero-stress state as idealized in the model and instead some residual stress is left over. In a linear unloading scenario, the model would behave elastically and return to a zero stress-state, meaning there is energy recovered by the specimen. Therefore, as seen in Figure 53, the value of the recovered energy is shown by the lower triangle and was not included in the calculation of fracture energy. Table 11 summarizes the homogenized properties determined from the completed analyses.

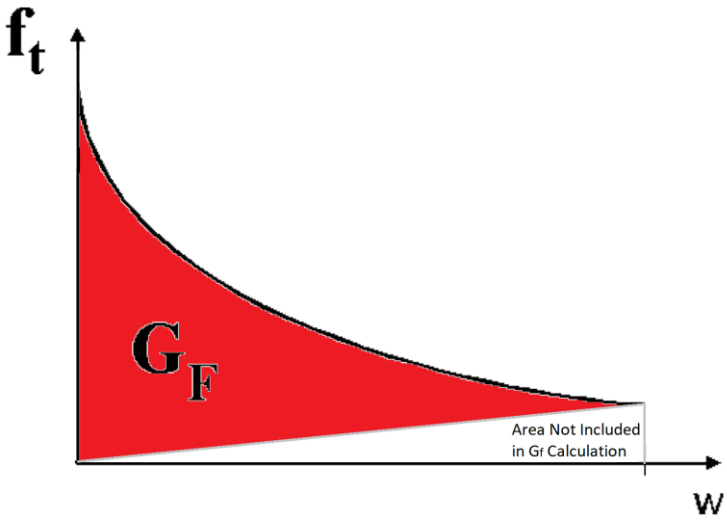

Figure 53 - Revised Method of Calculating Fracture Energy, G_f.

Table 11 - Summary of Homogenized Values for all Micro-scale Models with Stones ≤ 0.001 m².

Test Windows	Compressive Strength, f_c (MPa)	Tensile Strength, f_t (MPa)	Young's Modulus, E (MPa)	Fracture Energy, G_f (N/m)
RM1	1.06	0.093	190.73	18.17
RM2	1.30	0.088	185.19	27.69
RM3	1.18	0.091	200.98	21.42
RM4	1.20	0.091	242.89	20.38
RM5	1.20	0.093	175.54	31.83
Mean	1.18	0.091	199.06	23.90
St.Dev	0.08	0.002	23.41	5.07
COV (%)	6.44%	2.05%	11.76%	21.22%

As can be seen from the summarized table, the mean values for compressive strength and tensile strength are lower than that of the properties set for the mortar, with little variability. This shows that the homogenized strengths of the models are heavily dependent on the properties of mortar, since that is where the failure is concentrated. Furthermore, the irregular topology is shown to create stress concentrations which reduce the overall compressive strength.

It is interesting to note that the modulus of elasticity and fracture energy both show increases when compared to the properties of the mortar, proving that the models are stiffer and harder to pull apart than mortar on its own. The increase in stiffness is due to the addition of the highly stiff small stones into the mortar. Intuitively, a longer crack path increases the amount of energy required to form a full crack. Therefore, the values for fracture energy increased since the cracks that formed in the mortar were forced to propagate around the small stones instead of going through them.

The results for micro-scale models including stones less than 0.002 m² produced very similar results with less variance when compared to the previous set of micro-scale models. Figures 54-56 plot the compressive stress and tensile stress versus the strain and crack-width for each of the micro-

scale model tests performed and Table 12 summarizes the homogenized properties determined from the completed analyses. Since the failure modes between the two sets of micro-scale models were quite similar, detailed figures for this set have been left out of the body of the report and inserted into Appendix C.

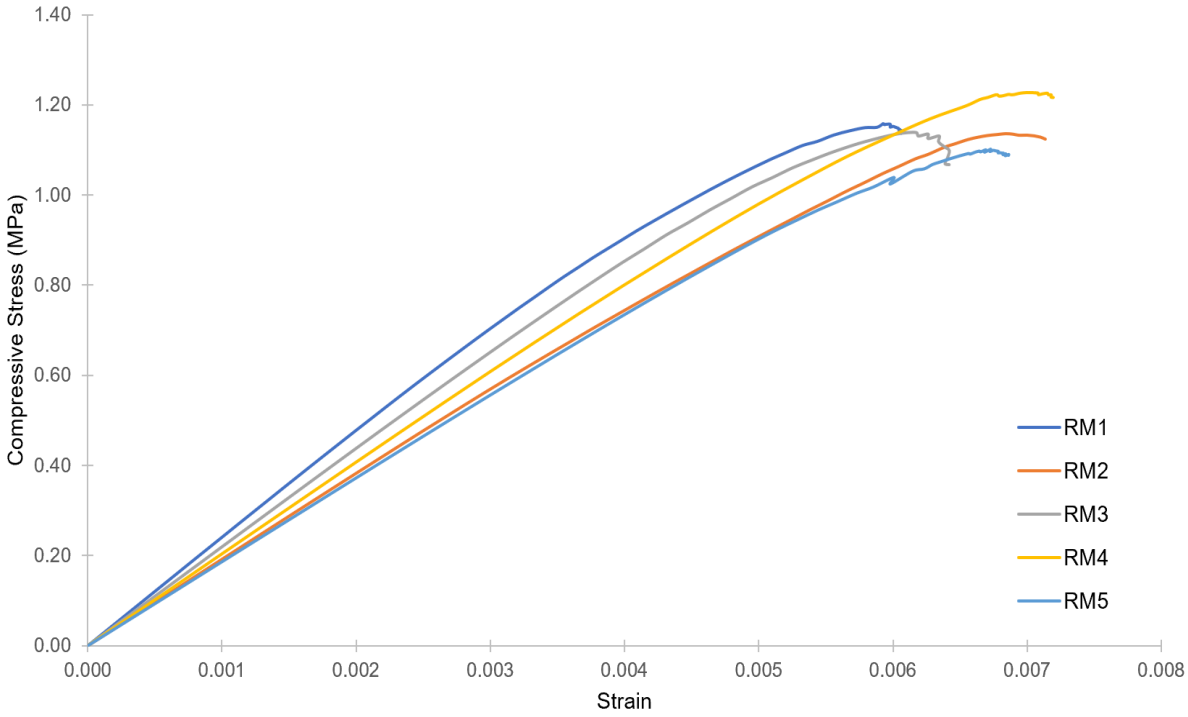

Figure 54 - Compressive Stress vs Strain for all Micro-scale Models with Stones ≤ 0.002 m².

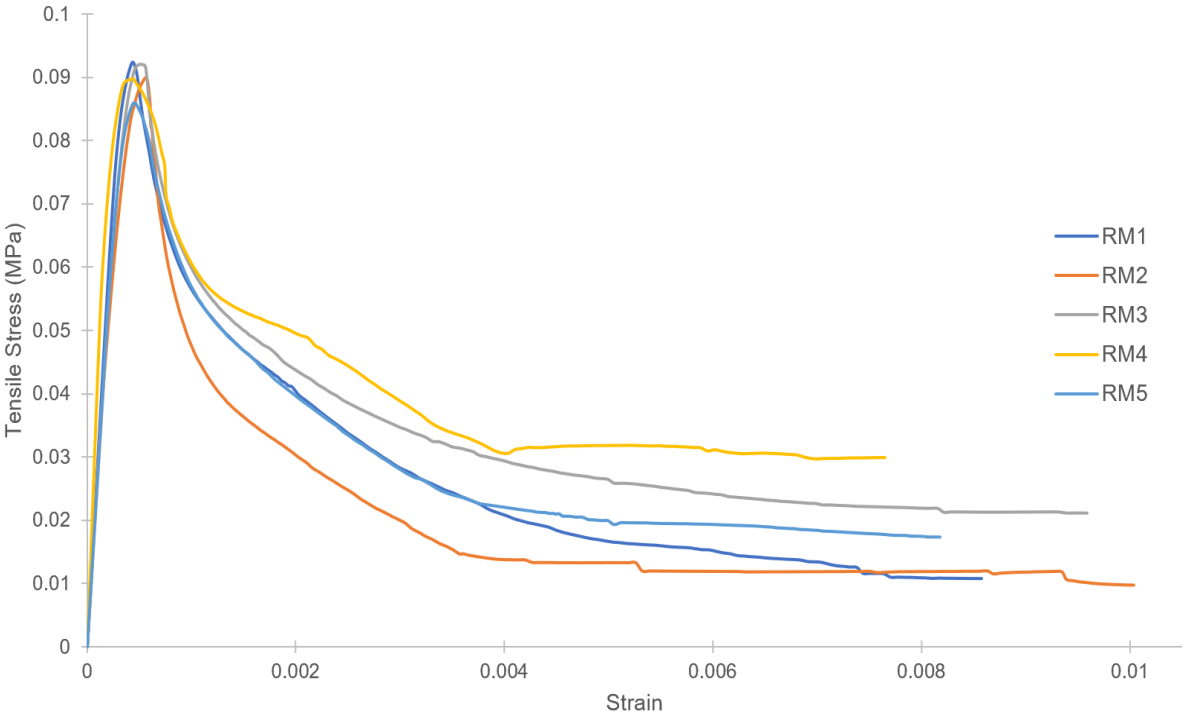

Figure 55 - Tensile Stress vs Strain for all Micro-scale Models with Stones ≤ 0.002 m².

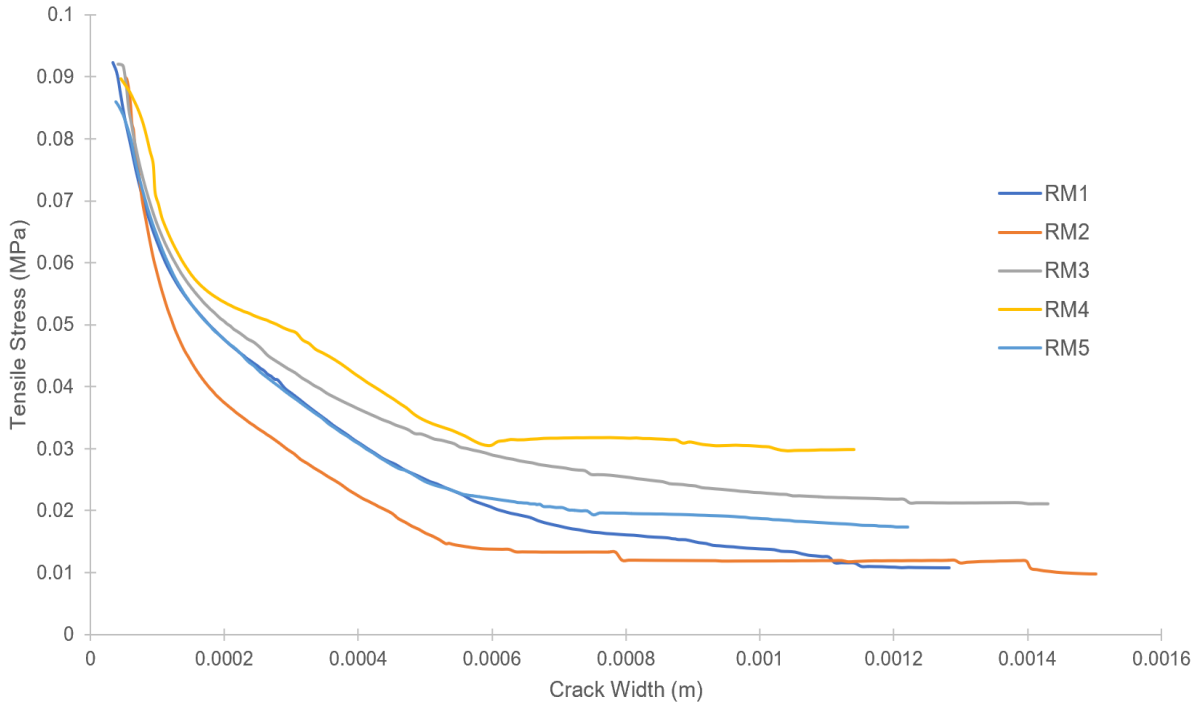

Figure 56 - Tensile Stress vs Crack Width all Micro-scale Models with Stones ≤ 0.002 m².

Table 12 - Summary of Homogenized Values for all Micro-scale Models with Stones ≤ 0.002 m².

Test Windows	Compressive Strength, f_c (MPa)	Tensile Strength, f_t (MPa)	Young's Modulus, E (MPa)	Fracture Energy, G_f (N/m)
RM1	1.16	0.092	241.02	25.30
RM2	1.14	0.090	192.21	19.94
RM3	1.14	0.092	219.39	26.95
RM4	1.23	0.090	203.75	27.94
RM5	1.10	0.086	186.26	23.95
Mean	1.15	0.090	208.53	24.82
St.Dev	0.04	0.002	19.79	2.80
COV (%)	3.61%	2.54%	9.49%	11.26%

When comparing the results of the homogenized properties for the micro-scale models incorporating different stone thresholds, the compressive strength is shown to be slightly lower for the models with 0.002 m² stones. The loss in strength in this model type can be attributed to the larger test-window size, since a larger test window includes for the possibility of a decrease in projected stone area within the mortar, meaning a lesser total area of stone projected to the model plane. The formation of more tortuous cracks within the micro-scale models with 0.002 m² stones led to slight increases in stiffness and fracture energy. Based on the results, it is recommended a more rigorous analysis of micro-scale models are completed utilizing more test windows to attain a better distribution

of homogenized properties. Figures 57 and 58 depict the overlap of the normal distributions for homogenized properties for the micro-scale models with different stone thresholds.

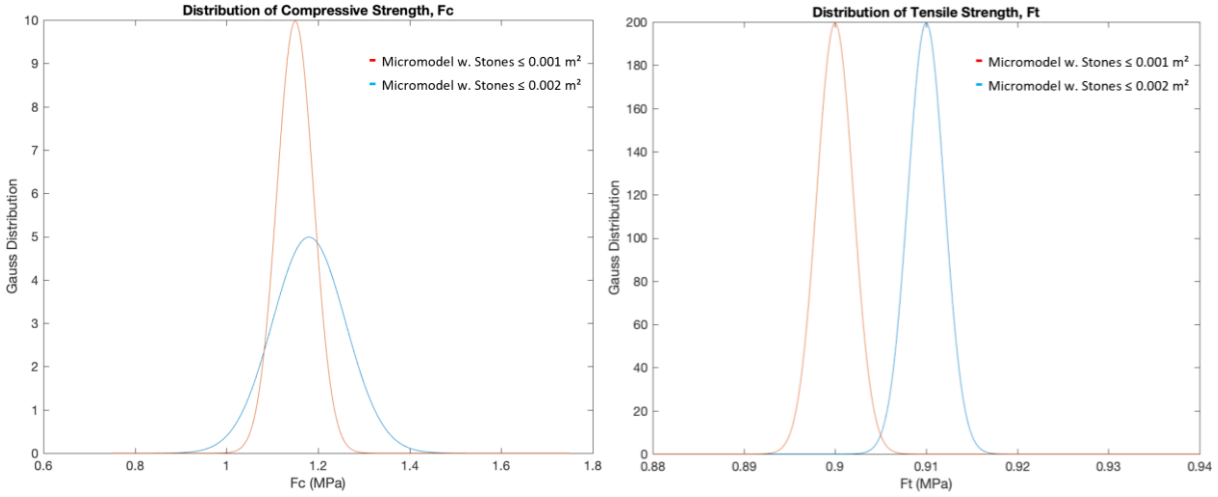

Figure 57 - Overlap of Normal Distributions for f_c and f_t.

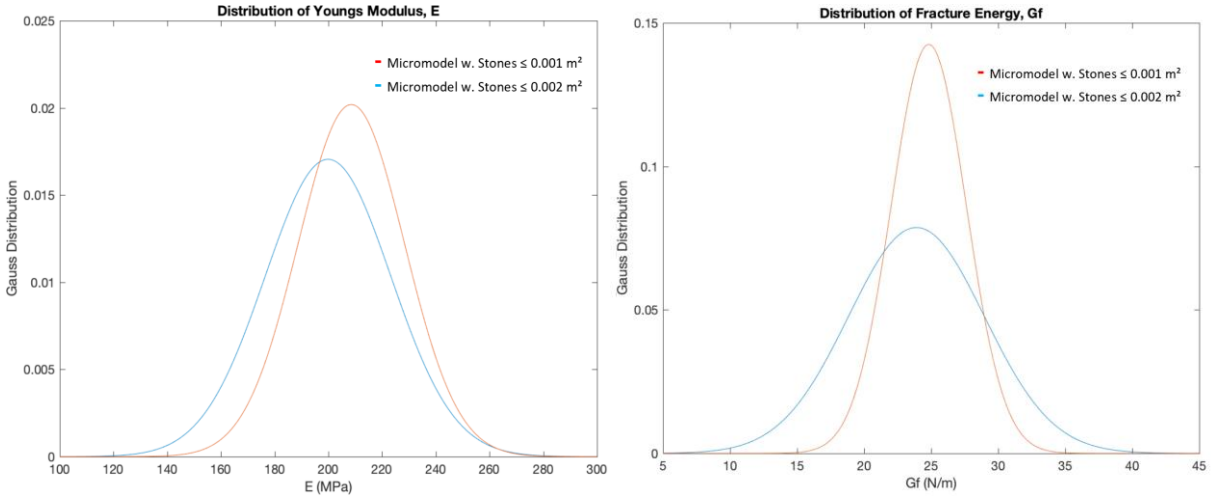

Figure 58 - Overlap of Normal Distributions for E and G_f.

4.2 MESO-SCALE MODELS WITH UNIFORM MATRIX PROPERTIES

The meso-scale models were first run using the mean values obtained for both matrix components described in the previous section. The meso-scale models were analyzed by observing contour plots for crack width, equivalent plastic strain and deformed shape. Figures 59-61 detail the post-peak results for meso-scale model 2. For a detailed look at each of the meso-scale models and failure modes, see Appendix D.

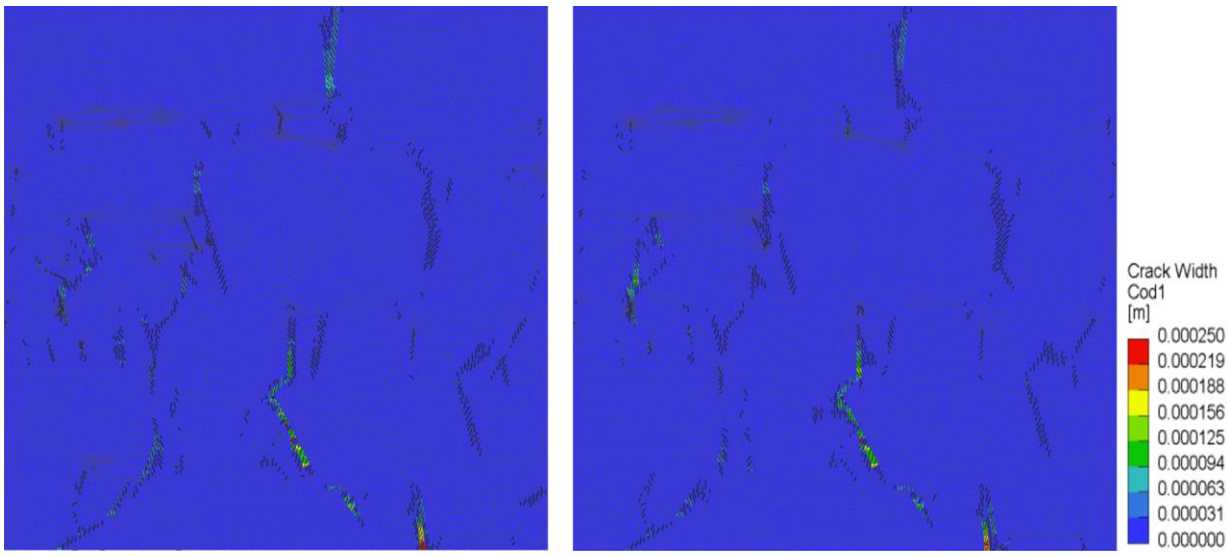

Figure 59 - Meso-scale Model 2 Crack Width. Matrix with Stones ≤ 0.001 m² (Left). Matrix with Stones ≤ 0.002 m² (Right).

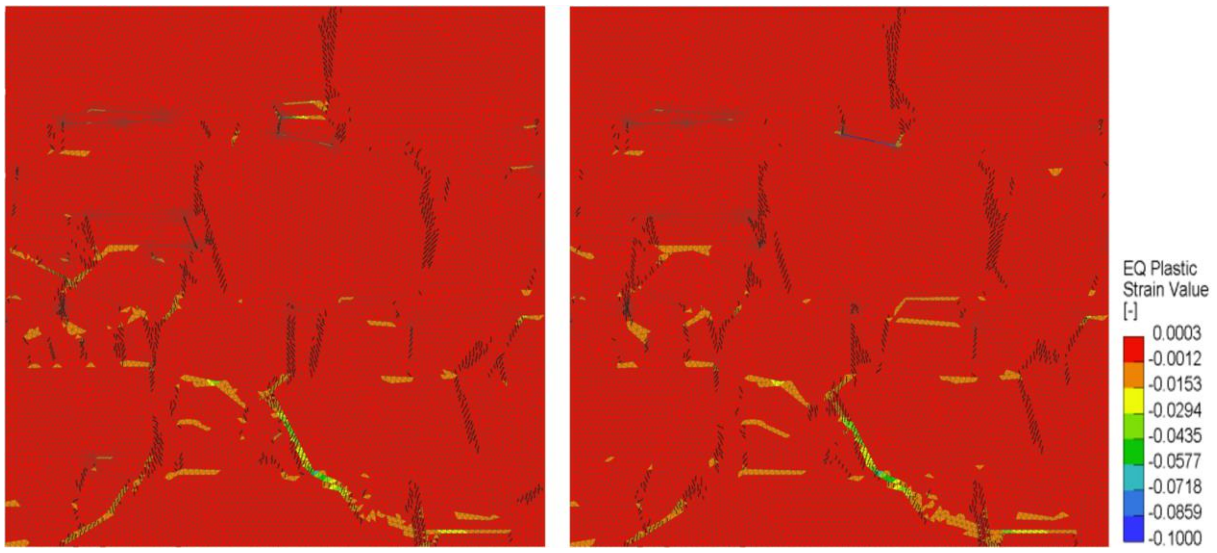

Figure 60 - Meso-scale Model 2 Equivalent Plastic Strain. Matrix with Stones ≤ 0.001 m² (Left). Matrix with Stones ≤ 0.002 m² (Right).

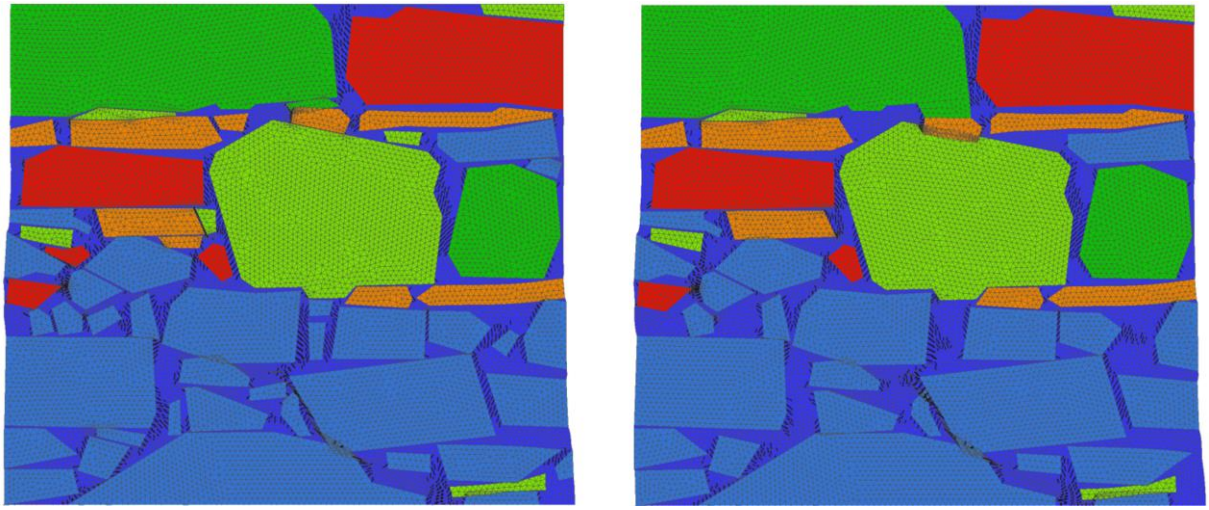

Figure 61 - Meso-scale Model 2 Deformed Shapes. Matrix with Stones ≤ 0.001 m² (Left). Matrix with Stones ≤ 0.002 m² (Right).

From the above visuals obtained from the analysis of meso-scale model 2, both models were shown to exhibit the same behaviours of failure. The locations of cracks and crack width values for both models were seen to be relatively similar, but there was a slight increase in the number of cracks in the model with a matrix including stones less than 0.001 m². This is due to the model having a higher projected stone area than the model with a matrix including stones less than 0.002 m². Comparing equivalent plastic strain, the areas of concentration slightly change, with the model with a matrix including stones less than 0.002 m² having a few additional areas due to the decrease in projected stone area, meaning more stone elements were encompassed within the matrix component. Based on the deformed shaped, it was observed that models both failed due to a combination of local compressive crushing and tensile splitting. In summary, a higher projected stone area modelled and not encompassed within the matrix component led to the formation of more cracks due to the increased irregularity in the model topology. Furthermore, a change in the projected stone area modelled led to a change in the distribution of equivalent plastic strain. These results were typical for all meso-scale models tested. Figure 62 along with Tables 13 and 14 summarize the compressive strength and stiffness data gained from each of the models.

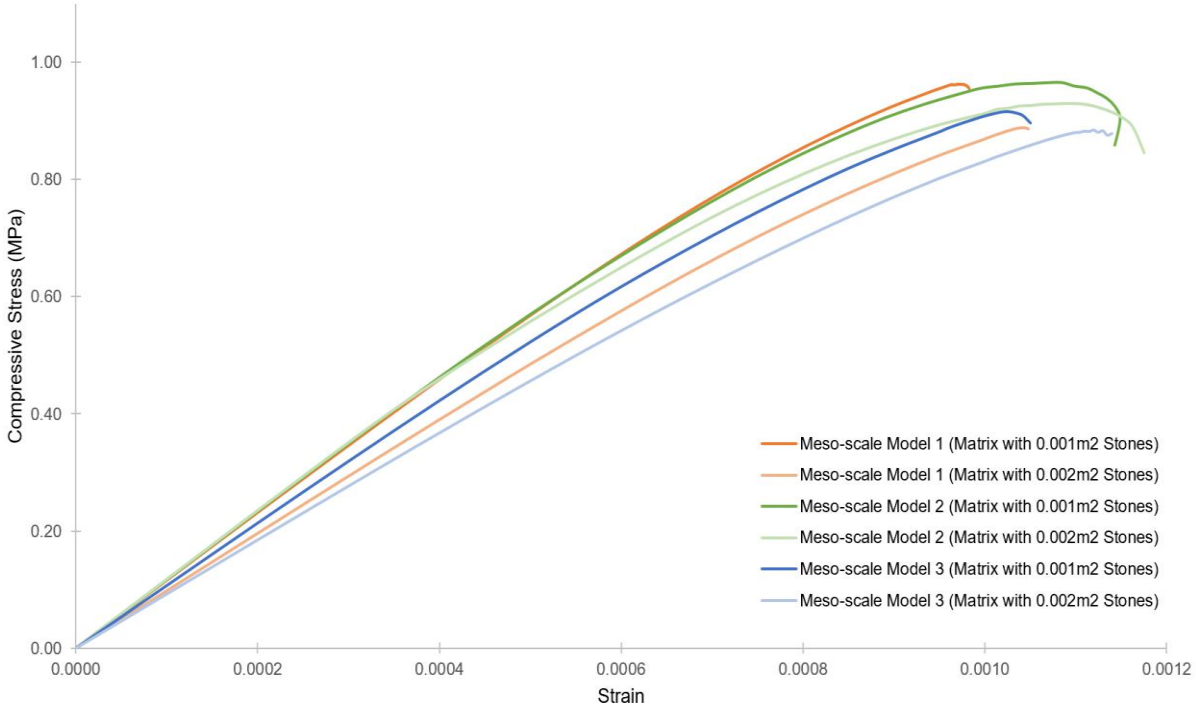

Figure 62 - Compressive Stress vs Strain for Meso-scale Models with Uniform Matrix Properties.

Table 13 - Compressive Strengths for Meso-scale Models with Uniform Matrix Properties.

Meso-scale Models	Wall Panel 1	Wall Panel 2	Wall Panel 3	Average	St. Dev	COV (%)
	Compressive Strength, f_c (MPa)					
Matrix with Stones ≤ 0.001 m²	0.96	0.97	0.92	0.95	0.019	2.04%
Matrix with Stones ≤ 0.002 m²	0.89	0.93	0.88	0.90	0.017	1.96%

Table 14 - Young's Modulus for Meso-scale Models with Uniform Matrix Properties.

Meso-scale Models	Wall Panel 1	Wall Panel 2	Wall Panel 3	Average	St. Dev	COV (%)
	Young's Modulus, E (GPa)					
Matrix with Stones ≤ 0.001 m²	1.16	1.17	1.07	1.13	0.045	3.97%
Matrix with Stones ≤ 0.002 m²	0.98	1.18	0.92	1.02	0.111	10.83%

Overall, the uniaxial compressive strength and Young's modulus of models with both matrices were relatively close in value and both had a small coefficient of variance. By observing the failure mechanism for each meso-scale model, it can be concluded that the irregularity in the topology of the walls created stress concentrations in the weakest component, in this case being the matrix, where it failed due to combined local crushing and tensile splitting.

4.3 MESO-SCALE MODELS UTILIZING RANDOM FIELDS

Utilizing the homogenized property distributions obtained from the micro-scale model analyses, random fields were generated in FREET for both types of meso-scale models for wall panel 2. This specific model was chosen to proceed with the analysis as it easily reached post-peak behaviour with

no convergence issues in earlier calculations. The generated distributions for the random fields can be found in Table 15 and images of the random fields for simulation 1 overlaid with post-peak crack locations for both types of meso-scale models can be seen in Figures 63-66. Additional figures showing the random field generations and post-peak crack locations for simulations 2 and 3 can be found in Appendix E.

Table 15 - Random Field Distributions.

Random Field Simulation	Matrix with Stones ≤ 0.001 m²			Matrix with Stones ≤ 0.002 m²		
	Property	Mean	St. Dev	Property	Mean	St. Dev
1	f_c	-1.154	0.079	f_c	-1.145	0.041
	E	201.660	25.494	E	208.970	18.496
	f_t	0.092	0.002	f_t	0.090	0.002
	G_f	24.477	5.521	G_f	25.527	2.4776
2	f_c	-1.183	0.067	f_c	-1.163	0.045
	E	200.190	26.601	E	203.820	17.525
	f_t	0.091	0.002	f_t	0.089	0.002
	G_f	24.159	5.761	G_f	26.262	2.8191
3	f_c	-1.170	0.080	f_c	-1.149	0.043
	E	201.510	25.282	E	206.750	20.614
	f_t	0.091	0.002	f_t	0.090	0.002
	G_f	24.443	5.475	G_f	25.142	3.0353
4	f_c	-1.204	0.079	f_c	-1.150	0.041
	E	206.050	21.131	E	207.180	20.735
	f_t	0.090	0.002	f_t	0.090	0.002
	G_f	25.426	4.577	G_f	25.247	2.7099
5	f_c	-1.177	0.085	f_c	-1.140	0.039
	E	206.420	22.510	E	204.930	17.678
	f_t	0.091	0.002	f_t	0.091	0.002
	G_f	25.506	4.875	G_f	26.032	3.1781

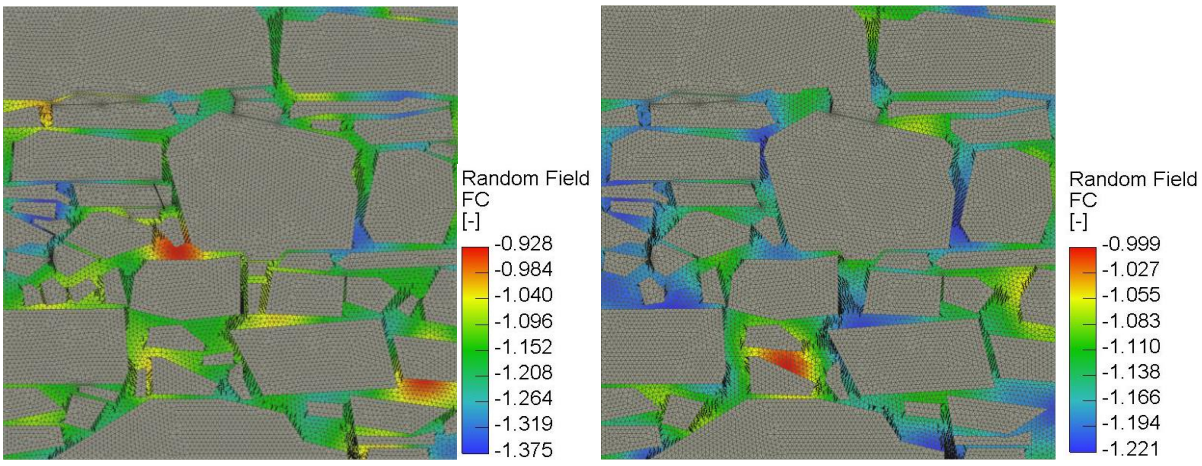

Figure 63 - Random Fields for f_c and Post-Peak Crack Locations. Matrix with Stones ≤ 0.001 m² (Left). Matrix with Stones ≤ 0.002 m² (Right).

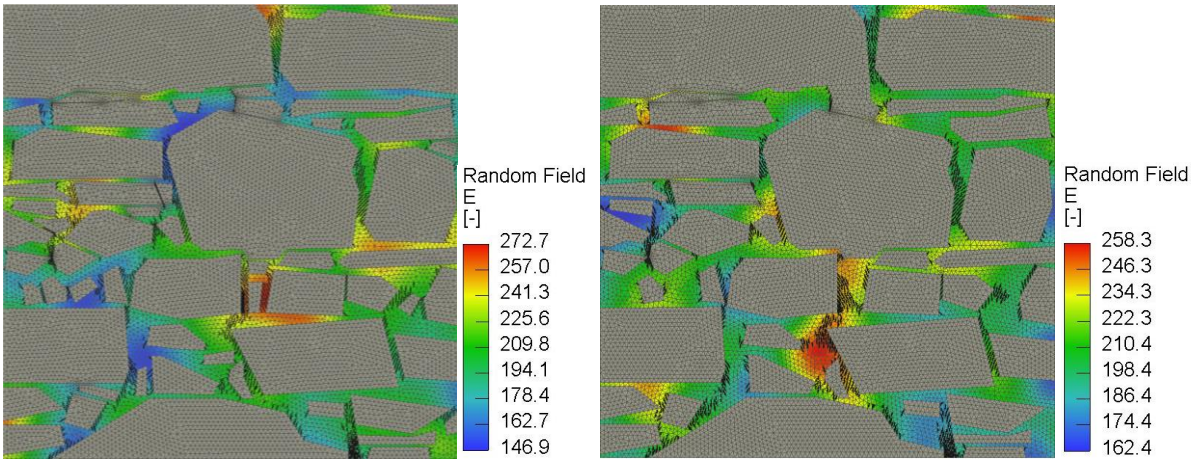

Figure 64 - Random Fields for E and Post-Peak Crack Locations. Matrix with Stones ≤ 0.001 m² (Left). Matrix with Stones ≤ 0.002 m² (Right).

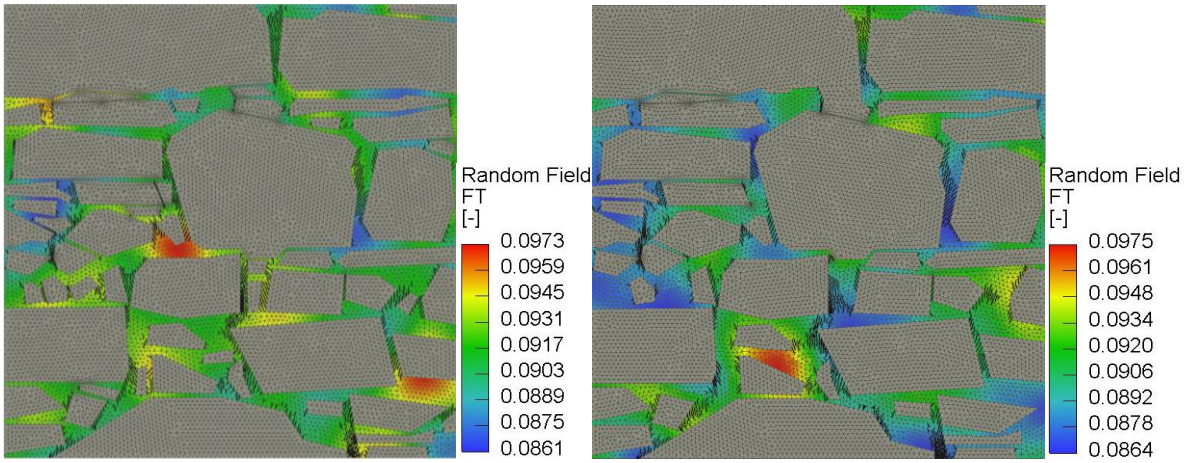

Figure 65 - Random Fields for F_t and Post-Peak Crack Locations. Matrix with Stones ≤ 0.001 m² (Left). Matrix with Stones ≤ 0.002 m² (Right).

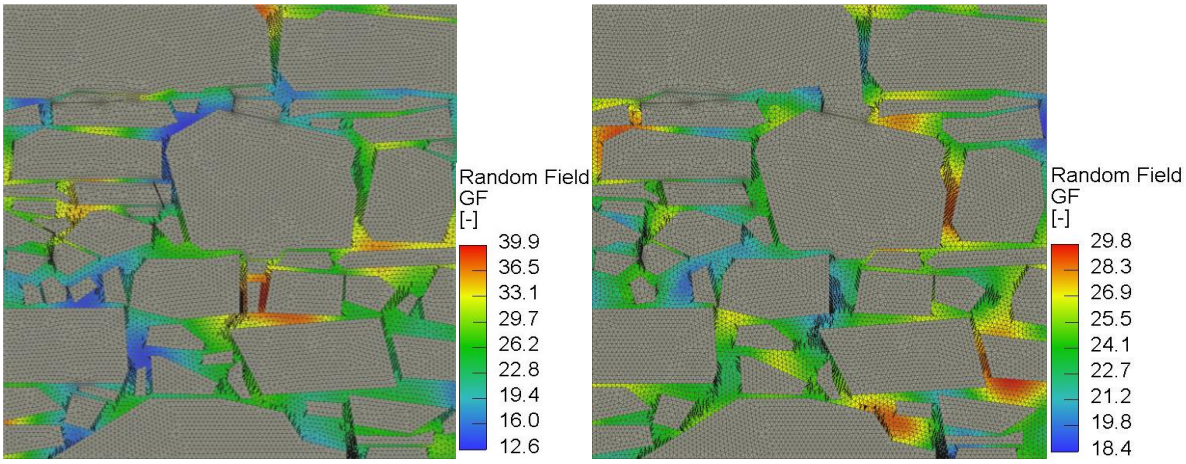

Figure 66 - Random Fields for G_f and Post-Peak Crack Locations. Matrix with Stones ≤ 0.001 m² (Left). Matrix with Stones ≤ 0.002 m² (Right).

As can be seen from the above figures, cracks were observed to form in the same locations between both models regardless of the spatial variability of the material parameters for the matrix. This can be attributed to the very minor difference and low variability between the matrix properties for each random field generation. Furthermore, by observing contour plots for the equivalent plastic strain as shown in Figure 67, areas that reach local crushing are similar to the ones found within the meso-scale models calculated using a uniform matrix. Additional areas of local crushing are due to low compressive strengths produced by the random field for the matrix component in that area. The compressive strengths from the random field analyses completed are plotted against strain in Figures 68-69 and results are summarized in Table 16.

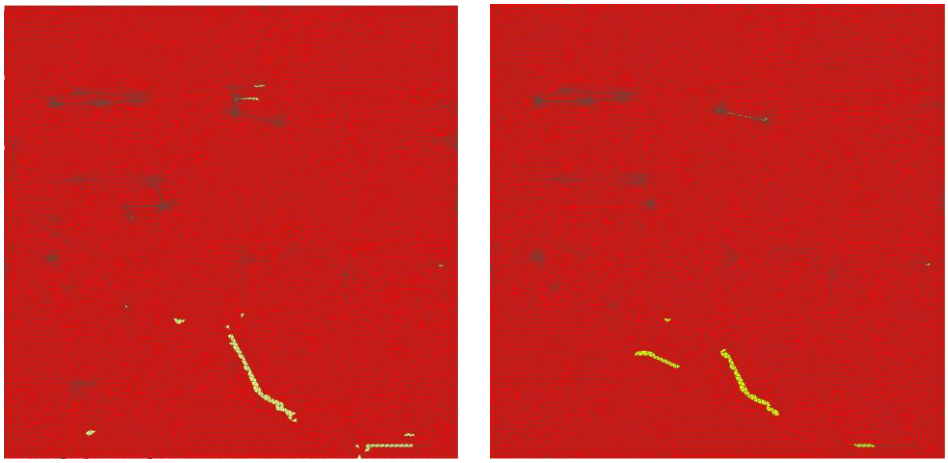

Figure 67 - Areas with High Plastic Strain. Matrix with Stones ≤ 0.001 m² (Left). Matrix with Stones ≤ 0.002 m² (Right).

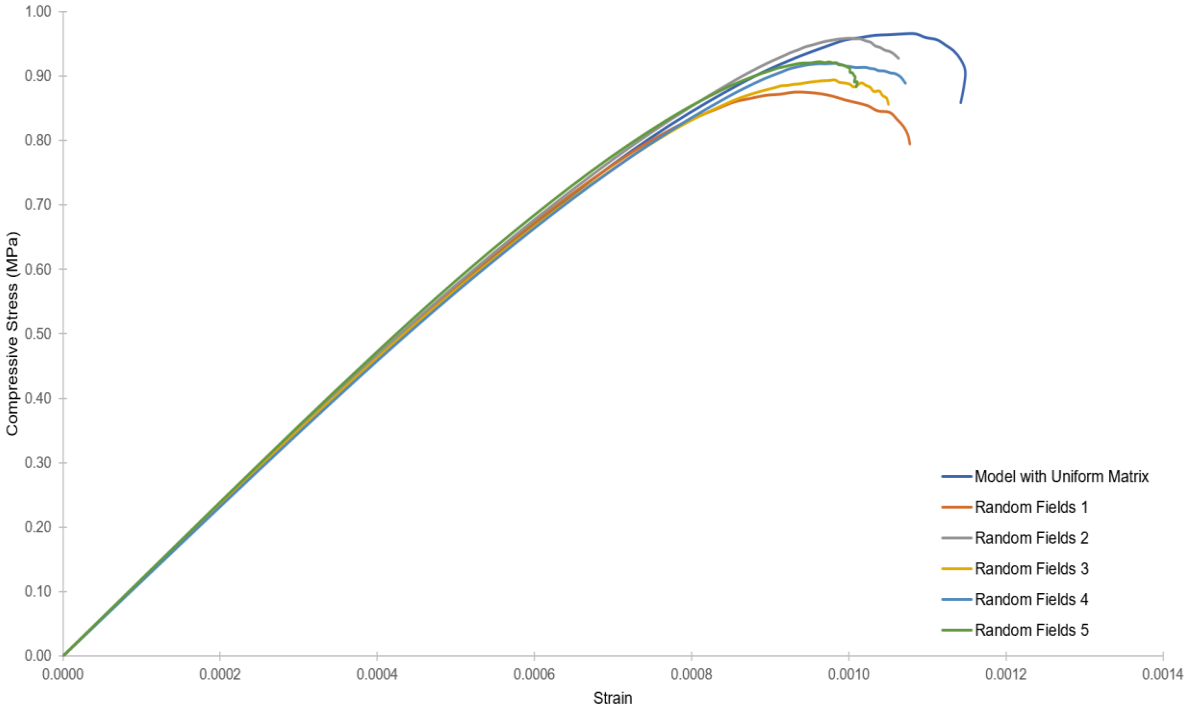

Figure 68 - Compressive Stress vs Strain for Meso-scale Model 2 with Matrix with Stones ≤ 0.001 m².

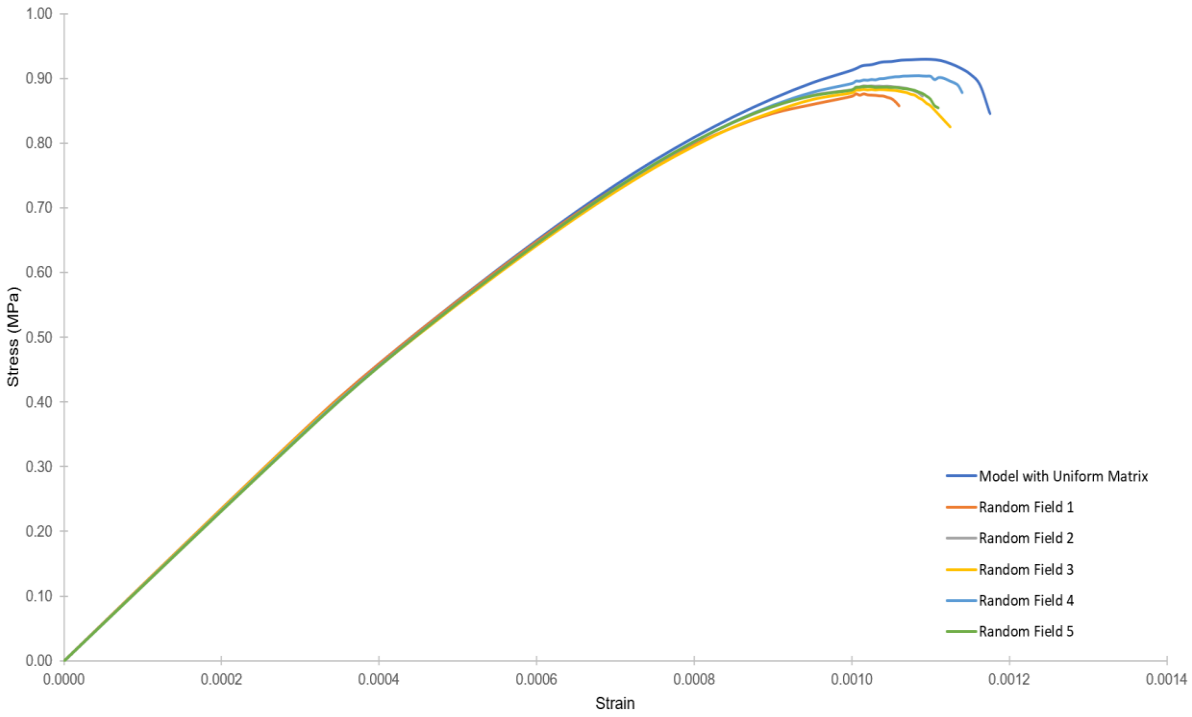

Figure 69 - Compressive Stress vs Strain for Meso-scale Model 2 with Matrix with Stones ≤ 0.002 m².

Table 16 - Summary of Compressive Strength (MPa) for Wall Panel 2.

Model	Matrix Incl. Stones ≤ 0.001 m²	Matrix Incl. Stones ≤ 0.002 m²
Model with Uniform Matrix	0.97	0.93
RF1	0.87	0.88
RF2	0.96	0.89
RF3	0.89	0.88
RF4	0.92	0.88
RF5	0.92	0.89
Mean	0.92	0.89
St. Dev	0.03	0.02
COV (%)	3.50%	1.98%

Based on the results, by considering spatial variability of the matrix, the overall compressive strength of the masonry wall panel was reduced by 0.04-0.05 MPa for both matrices containing different thresholds of stone sizes. High mean values generated for the compressive strength of the matrix component correlated to higher values of overall compressive strength for the random field models. The spatial variability of these properties still caused a reduction in overall strength when compared to models with a uniform matrix, which is attributed to introduction of weaker properties on a local scale generated by the random fields.

4.4 COMPARISONS

To ensure accuracy of the results attained through the multi-scale modelling approach, simple comparisons for the overall uniaxial compressive strength were made to literature and other methods for historic masonry structures. First, the masonry quality index (MQI), as previously mentioned in Section 2.4, was used to determine the compressive strength based on a qualitative assessment of the walls of St. Ann's Church. The parameters and assumptions used to calculate the MQI can be seen in Table 17.

Table 17 - Masonry Quality Index Calculation for St. Ann's Church.

Evaluated Categories		Given Factor	Value for Vertical Loading
Mechanical Properties and Conservation State	SM	PF	0.7
Unit Dimensions	SD	PF	0.5
Unit Shapes	SS	NF	0
Wall Leaf Connections	WC	PF	1
Horizontal Bed Joints	HJ	NF	0
Vertical Bed Joints	VJ	NF	0
Mortar Quality	MM	NF	0
MQI			1.05

A masonry quality index of around 1 correlates with a uniaxial compressive strength of around 1 MPa, is which relatively close to the values attained from the analyses. Furthermore, reviewing the Italian code for masonry (NTC 2008), the lower and upper limit for uniaxial compressive strength of irregular stone masonry (pebbles, erratic, irregular stones) is 1-1.8 MPa, which is also close to the values attained from the analyses. Even the average Young's modulus of 1 GPa attained from the meso-scale models lines up with the upper limit given in the NTC (NTC 2008). The minor difference in strength could be due to the low values that were set for the mortar during the micro-scale modelling analyses.

5. CONCLUSION

The structural analysis of historic structures can be quite troublesome when dealing with irregular masonry due to the randomness of the topology and lack of information available. Due to the limitations of finite element analysis, a multi-scale modelling approach was utilized to analyze the masonry walls of St. Ann's Church. Using a statistical analysis of the irregular geometry, small stones were grouped in with the mortar and treated as a matrix component with homogenized properties in a mesoscale-level representation of the masonry. To characterize this matrix component, microscale-level models were constructed, in which only the small stones and mortar were represented. Using updated material parameters taken from on-site and laboratory tests, the micro-scale models were tested under uniaxial compression and tension to determine homogenized properties. Meso-scale models were then tested under uniaxial compression, first using a matrix component with uniform

properties, and then using a matrix component with variable properties described by random fields. Furthermore, the multi-scale study was performed for two different threshold sizes defining the “small” stones to compare differences.

Based on the analysis completed, the uniaxial compressive strength decreased when moving from the micro-structure of the mortar, to the micro-scale models of the mortar with small stones, to the meso-scale models of the matrix with large stones. This decrease was attributed to the non-uniformity of the topology which caused stress concentrations in the weak material at each level, leading to combined failure mechanisms from both local compressive crushing and tensile splitting. The use of random fields showed minor decreases in compressive strength, with the location of cracks and failure mechanisms remaining similar throughout all meso-scale models. The results of this study show that the spatial variability of the matrix component can be neglected due to the small distributions of the homogenized properties obtained but should be considered if the distributions become larger after analyzing more micro-scale models.

In the future, the author of this work proposes a few additional steps to enhance the quality and accuracy of the work carried out. For example, more micro-scale models using the test-window method should be analyzed to provide a full statistical description of the randomness of topology of small stones in the mortar. This would allow for the determination of a good distribution of homogenized properties of the matrix component, since the limited number of windows completed within the study led to a variable response that was quite narrow and unrealistic. Furthermore, the variability shouldn’t be limited to the topology and instead extended to the material properties as well. Therefore, the study could be enhanced by considering random variables for the mortar properties in unison with the multi-scale modelling approach and application of random fields. Also, expanding the random fields to encompass the variability in the stone properties could yield interesting results and allow for a quicker analysis by eliminating the requirement to identify each stone separately. Lastly, it could be interesting to analyze size effect and the possible implementation of different boundary conditions to determine their effect on the overall strength of the masonry walls at St. Ann’s Church.

6. REFERENCES

Abdulla, K. F., Cunningham, L. S., & Gillie, M. (2017). Simulating masonry wall behaviour using a simplified micro-model approach. *Engineering Structures*, *151*, 349–365. https://doi.org/10.1016/j.engstruct.2017.08.021

Avila, E. A. (2019). Scanning Electron Microscopy. Guimaraes: University of Minho.

“Bauxite - Czechoslovakia” in Czech Republic, Aluminum Occurrence. (2003). Retrieved June 2, 2019, from https://thediggings.com/mines/usgs10093367

Borri, A., Corradi, M., Castori, G., & De Maria, A. (2015). A method for the analysis and classification of historic masonry. *Bulletin of Earthquake Engineering*, *13*(9), 2647–2665. https://doi.org/10.1007/s10518-015-9731-4

Cavalagli, N., Cluni, F., & Gusella, V. (2013). Evaluation of a Statistically Equivalent Periodic Unit Cell for a quasi-periodic masonry. *International Journal of Solids and Structures*, *50*(25–26), 4226–4240. https://doi.org/10.1016/j.ijsolstr.2013.08.027

Cavalagli, N., Cluni, F., & Gusella, V. (2018). Failure surface of quasi-periodic masonry by means of Statistically Equivalent Periodic Unit Cell approach. *Meccanica*, *53*(7), 1719–1736. https://doi.org/10.1007/s11012-017-0771-5

Červenka, V., Jendele, L., & Červenka, J. (2018). *ATENA Program Documentation Part 1 Theory*. *Červenka Consulting*. Prague.

Cluni, F., & Gusella, V. (2004). Homogenization of non-periodic masonry structures. *International Journal of Solids and Structures*, *41*(7), 1911–1923. https://doi.org/10.1016/j.ijsolstr.2003.11.011

Drdácký, M., & Slížková, Z. (2008). Mechanical Characteristics of Historical Mortars from Tests on Small-Sample Non-Standard Specimens, (January).

Falsone, G., & Lombardo, M. (2007). Stochastic representation of the mechanical properties of irregular masonry structures. *International Journal of Solids and Structures*, *44*(25–26), 8600–8612. https://doi.org/10.1016/j.ijsolstr.2007.06.030

Gajjar, P. (2018). *Nonlinear numerical evaluation of the wall bearing capacity and the structure stability of the St. Ann Church from the Broumov Group of Churches*. Czech Technical University.

Goins, E. S. (2004). Materials Research Series. Standard Practice for Determining the Components of Historic Cementitious Materials, 1–69.

Gusella, V., & Federico, C. (2006). Random Field and Homogenization For Masonry With Nonperiodic Microstructure. *Journal of Mechanics of Materials and Structures*, *1*(2), 357–386.

Kabele, P. (2018). SA2.1 : Structural Analysis Techniques: Governing Equations of Solid Mechanics. Prague: SAHC.

Kuklík, P. (Czech T. U. (2018). *Core Sampling at St. Ann's Church*. Prague.

Lorenço, P. (1996). *Computational Strategies for Masonry Structures*. Delft University.

Lourenço, P. B. (2018). Modelling of Masonry and Homogenization - Solving Engineering Problems & Definition of Practical Rules Materials with Micro-Structure.

Milani, G., Esquivel, Y. W., Lourenço, P. B., Riveiro, B., & Oliveira, D. V. (2013). Characterization of the response of quasi-periodic masonry: Geometrical investigation, homogenization and application to the Guimarães castle, Portugal. *Engineering Structures*, *56*, 621–641. https://doi.org/10.1016/j.engstruct.2013.05.040

Minerals Database - Aluminum. (2019). Retrieved June 2, 2019, from https://mineralseducationcoalition.org/minerals-database/aluminum/

Minerals Database - Feldspar. (2019). Retrieved June 2, 2019, from https://mineralseducationcoalition.org/minerals-database/feldspar/

Mojsilović, N. (2011). Strength of masonry subjected to in-plane loading: A contribution. *International Journal of Solids and Structures*, *48*(6), 865–873. https://doi.org/10.1016/j.ijsolstr.2010.11.019

Novák, D., Teplý, B., Keršner, Z., & Vořechovský, M. (2002). FREET Program Documentation - Theory. BRNO: Cervenka Consulting.

NTC. (2008). Italian Ministry of Infrastructure and Transportation.

Oates, J. A. H. (Joseph A. H. (1998). *Lime and limestone : chemistry and technology, production and uses*. Derbyshire: Wiley - VCH. Retrieved from https://books.google.cz/books?id=MVoEMNI5Vb0C&pg=PR3&hl=et&source=gbs_selected_pages&cad=2#v=onepage&q&f=false

Ostoja-Starzewski, M. (2006). Material spatial randomness: From statistical to representative volume element. *Probabilistic Engineering Mechanics*, *21*(2), 112–132. https://doi.org/10.1016/j.probengmech.2005.07.007

Proceq Rock Schmidt Hammer Operating Instructions. (2017).

Roca, P., Cervera, M., Gariup, G., & Pela', L. (2010). Structural Analysis of Masonry Historical Constructions. Classical and Advanced Approaches. *Archives of Computational Methods in Engineering*, *17*(3), 299–325. https://doi.org/10.1007/s11831-010-9046-1

Scacco, J. (2018). *Nonlinear numerical evaluation of the bearing capacity and the structure stability of the St. Jacob Church from the Broumov Group of Churches*. Czech Technical University.

Šejnoha, J., Šejnoha, M., Zeman, J., Sýkora, J., & Vorel, J. (2008). Mesoscopic study on historic masonry. *Structural Engineering and Mechanics*, *30*(1), 99–117. https://doi.org/10.12989/sem.2008.30.1.099

Speer, E. (2012). *Computer Modelling of the Spatial Variability of Material Parameters Within a Historical Masonry Arch Railway Bridge*. Czech Technical University.

Spence, S. M. J., Gioffrè, M., & Grigoriu, M. D. (2008). Probabilistic Models and Simulation of Irregular Masonry Walls. *Journal of Engineering Mechanics*, *134*(9), 750–762. https://doi.org/10.1061/(ASCE)0733-9399(2008)134:9(750)

Válek, J., & Veiga, R. (2005). Characterisation of mechanical properties of historic mortars: testing of irregular samples. *Transactions on the Built Environment*, *83*, 365–374. Retrieved from http://cat.inist.fr/?aModele=afficheN&cpsidt=17545867

Zeman, J., & Šejnoha, M. (2007). From random microstructures to representative volume elements. *Modelling and Simulation in Materials Science and Engineering*, *15*(4), S325–S335. https://doi.org/10.1088/0965-0393/15/4/S01

Zhang, S., Hofmann, M., & Beyer, K. (2018). A 2D typology generator for historical masonry elements. *Construction and Building Materials*, *184*, 440–453. https://doi.org/10.1016/j.conbuildmat.2018.06.085

Zhang, S., Taheri Mousavi, S. M., Richart, N., Molinari, J. F., & Beyer, K. (2017). Micro-mechanical finite element modeling of diagonal compression test for historical stone masonry structure. *International Journal of Solids and Structures*, *112*, 122–132. https://doi.org/10.1016/j.ijsolstr.2017.02.014

Appendix A: Statistical Calculations for Masonry Wall Geometry

Statistical Analysis - Summary

Wall Section	Area of Stones≤0.001 (m²)	Area of Stones≤0.002 (m²)	Area of Large Stones (m²)	Total Area of Stones (m²)	Area of Mortar
Wall 1	0.0329	0.0869	0.7272	0.8141	0.1859
Wall 2	0.0236	0.0548	0.7431	0.7979	0.2021
Wall 3	0.0458	0.0922	0.7041	0.7963	0.2037
Wall 4	0.0395	0.0920	0.7254	0.8174	0.1826
Wall 5	0.0337	0.0744	0.7387	0.8131	0.1869
Wall 6	0.0548	0.0998	0.7028	0.8026	0.1974
Mean	0.0384	0.0834	0.7235	0.8069	0.1931
St. Dev	0.0109	0.0163	0.0169	0.0091	0.0091
COV (%)	28.43%	19.57%	2.34%	1.12%	4.70%

Area of Stones ≤ 0.001 (m²) Analysis

Wall Panel	Area of Stones (%)	Area of Mortar (%)
Wall 1	15%	85%
Wall 2	10%	90%
Wall 3	18%	82%
Wall 4	18%	82%
Wall 5	15%	85%
Wall 6	22%	78%
Mean	16.4%	83.6%
St. Dev	4%	4%
COV (%)	23%	5%

Area of Stones ≤ 0.002 (m²) Analysis

Wall Panel	Area of Stones (%)	Area of Mortar (%)
Wall 1	32%	68%
Wall 2	21%	79%
Wall 3	31%	69%
Wall 4	33%	67%
Wall 5	28%	72%
Wall 6	34%	66%
Mean	30%	70%
St. Dev	5%	5%
COV (%)	15%	7%

Appendix B: Mortar Properties: SEM Analysis and Porosity Results

Elemental Analysis - St. Ann's Sample 1

Elements	1	2	3	4	5	6	7	8	9	10	11	12
CaO	48.29	0.11	1.14	1.82	52.60	67.99	66.56	72.37	62.70	71.50	78.01	74.69
SiO_2	1.31	99.17	73.34	55.84	29.85	19.66	21.22	14.53	20.24	18.39	11.24	17.68
Al_2O_3	0.60	0.27	14.24	27.19	11.41	7.60	6.94	8.34	11.25	6.28	7.51	4.24
MgO	0.24		1.98	5.00	1.80	1.29	1.05	1.36	1.47	0.91	0.81	0.84
Na_2O	0.07		0.17	0.12	0.36	0.14	0.16	0.55	0.21	0.18		0.25
K_2O	0.08		6.53	7.21	1.28	1.03	2.04	0.76	1.83	1.27	0.79	0.63
SO_3	49.40	0.08	0.11		0.15	0.37	0.15	0.42	0.18	0.06	0.26	0.20
Cl			0.15	0.12	0.50	0.70	0.47	0.83	0.44	0.40	0.25	0.42
TiO_2		0.24	0.18	2.70	0.36	0.12			0.05	0.10		0.23
FeO		0.09	2.15		1.71	1.09	1.41	0.84	1.66	0.91	1.11	0.83
celkem	100.0	100.0	100.0	100.0	100.0	100.0	100.0	100.0	100.0	100.0	100.0	100.0

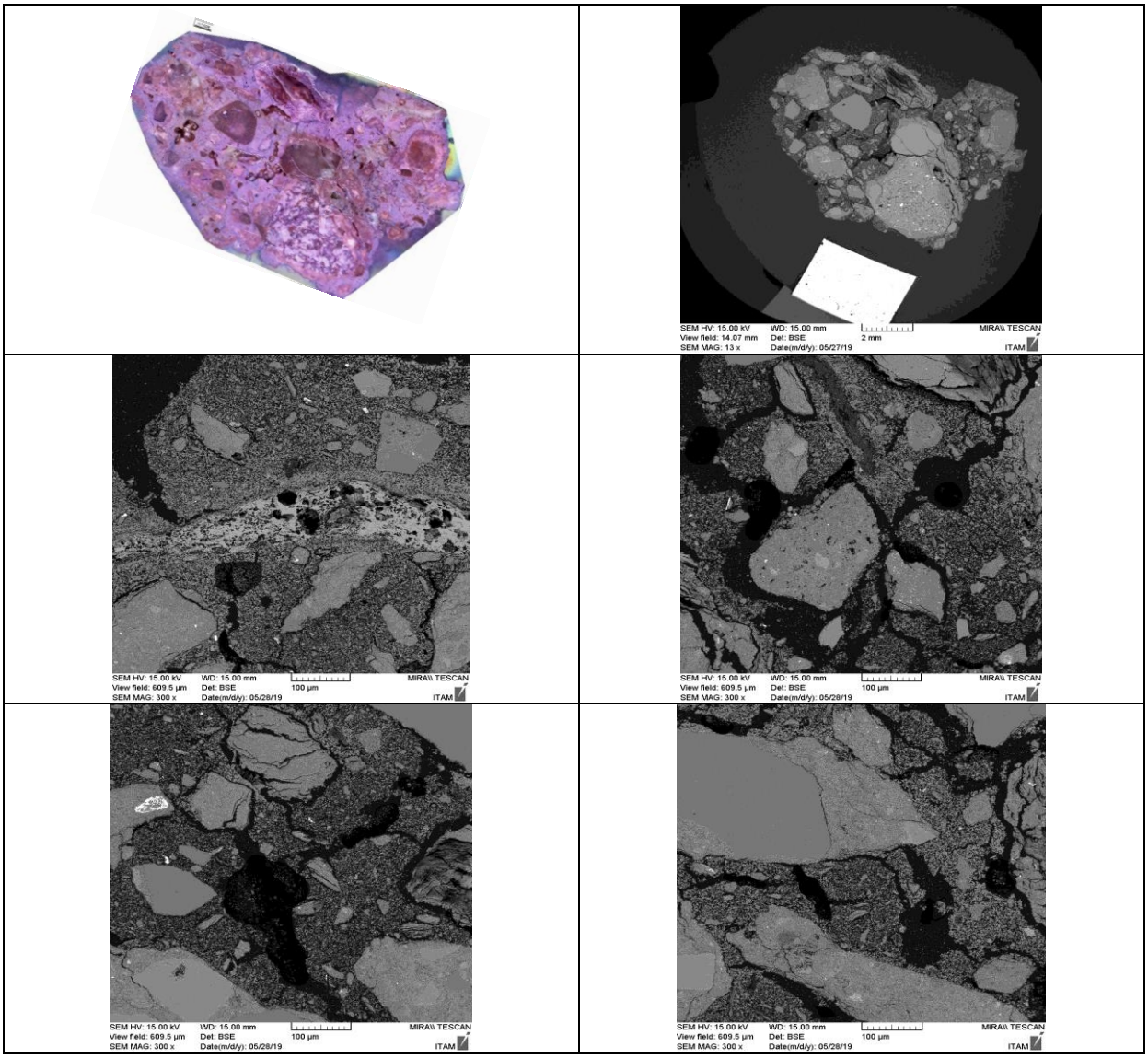

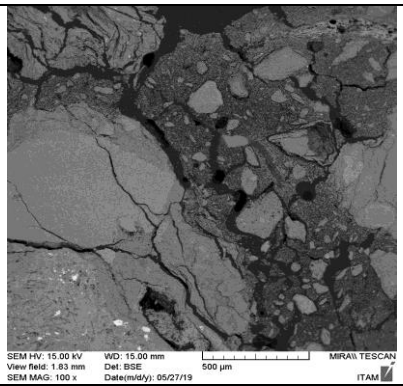
SEM HV: 15.00 kV
View field: 1.83 mm
SEM MAG: 100 x
WD: 15.00 mm
Det: BSE
Date(m/d/y): 05/27/19
500 µm
MIRA\\ TESCAN
ITAM

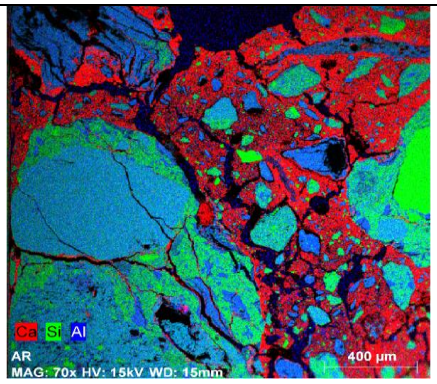
Ca
Si
Al
AR
MAG: 70x HV: 15kV WD: 15mm
400 µm

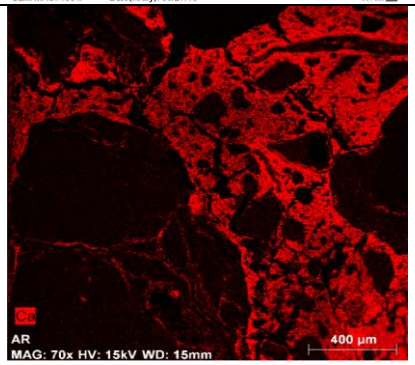
Ca
AR
MAG: 70x HV: 15kV WD: 15mm
400 µm

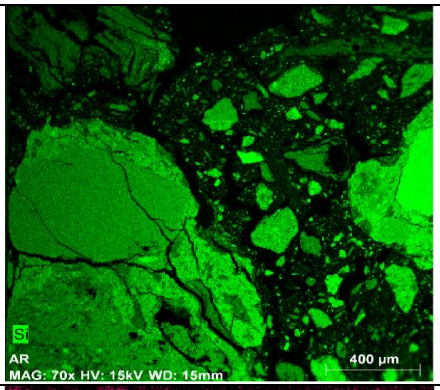
Si
AR
MAG: 70x HV: 15kV WD: 15mm
400 µm

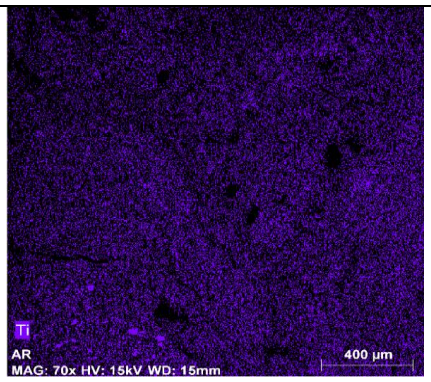
Ti
AR
MAG: 70x HV: 15kV WD: 15mm
400 µm

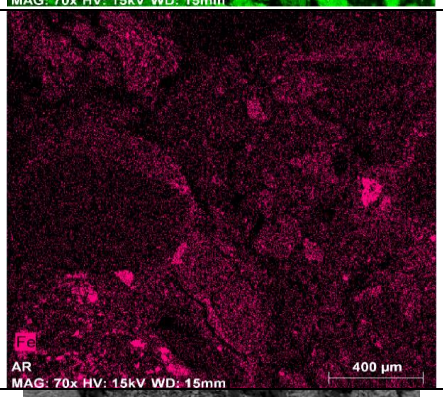
Fe
AR
MAG: 70x HV: 15kV WD: 15mm
400 µm

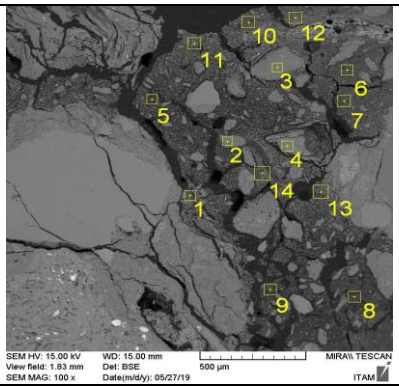
10
12
11
3
6
5
7
2
4
14
1
13
9
8
SEM HV: 15.00 kV
View field: 1.83 mm
SEM MAG: 100 x
WD: 15.00 mm
Det: BSE
Date(m/d/y): 05/27/19
500 µm
MIRA\\ TESCAN
ITAM


SEM HV: 15.00 kV
View field: 91.43 µm
SEM MAG: 2.00 kx
WD: 15.00 mm
Det: BSE
Date(m/d/y): 05/27/19
20 µm
MIRA\\ TESCAN
ITAM

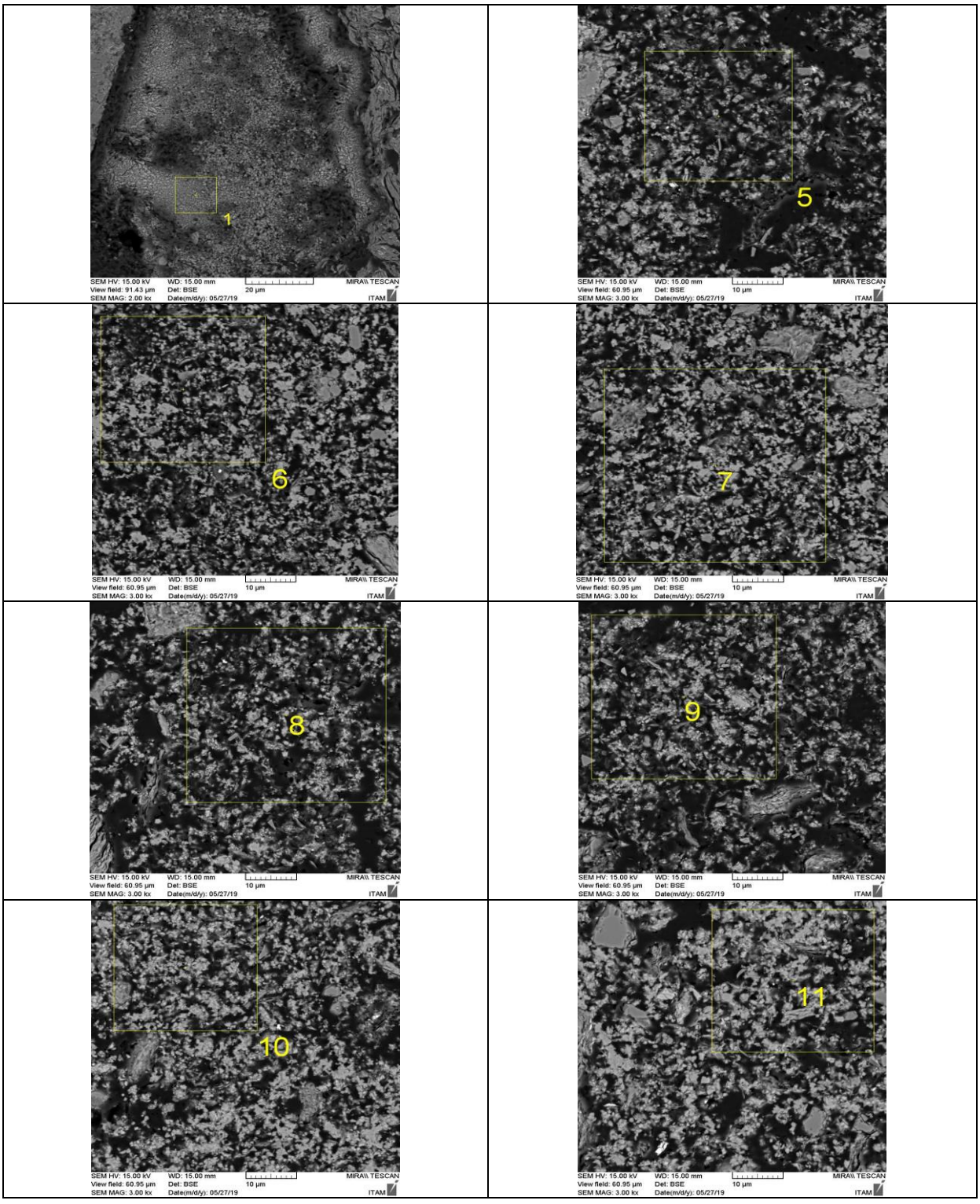
1
5
6
7
8
9
10
11

Elemental Analysis - St. Ann's Sample 2

Elements	1	2	3	4	5	6	7	8	9	10	11	12	13	14	15
CaO		0.37	1.61	0.34	9.28	51.44	57.29	58.20	50.59	70.34	80.55	63.74	75.24	63.16	84.12
SiO_2	99.74	63.92	53.00	64.86	48.10	31.97	28.87	26.33	30.94	17.87	11.99	24.28	15.56	21.77	8.03
Al_2O_3	0.06	18.74	28.75	12.61	21.83	7.58	7.26	7.98	8.22	5.62	3.81	5.85	4.37	7.51	2.35
MgO			9.56	1.94	4.18	1.02	1.32	0.95	0.91	1.02	0.50	0.79	0.84	1.60	0.38
Na_2O	0.05	3.46		0.14	0.94	0.18	0.14	0.56	0.53	0.52		0.22	0.09	0.14	0.15
K_2O		13.51	4.22	6.30	6.37	2.68	1.83	2.08	3.02	1.60	1.09	1.91	1.30	3.93	3.64
SO_3	0.07				0.10	0.79	0.59	0.76	0.74	0.75	0.50	0.94	0.57	0.18	0.97
Cl	0.07					0.21	0.41	0.30	0.67	0.47	0.15	0.33	0.29	0.26	0.15
TiO_2			0.17	0.64	0.58	0.30			0.09	0.30	0.26	0.24	0.10		0.11
FeO			2.64	13.17	8.60	3.84	2.29	2.83	4.29	1.50	1.15	1.69	1.64	1.44	0.08
celkem	100.0	100.00	100.0	100.0	100.0	100.0	100.0	100.0	100.0	100.0	100.0	100.0	100.0	100.0	100.0

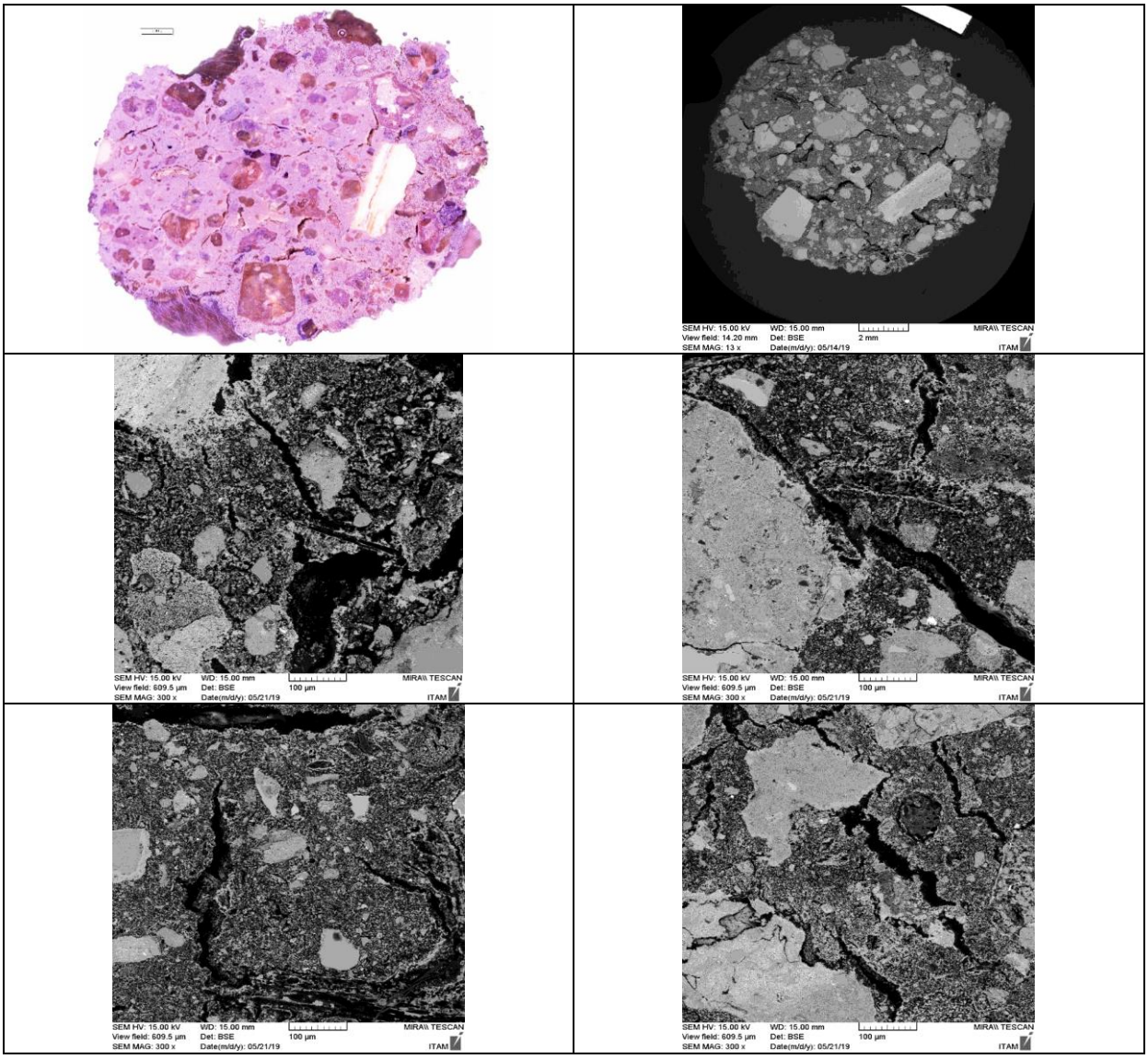

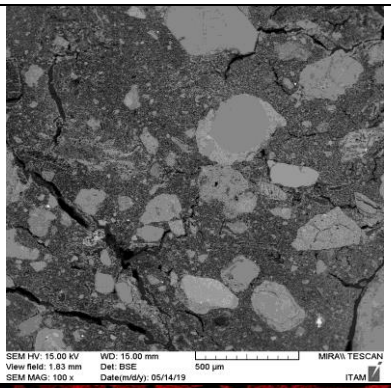
SEM HV: 15.00 kV
WD: 15.00 mm
MIRA\\ TESCAN
View field: 1.83 mm
Det: BSE
500 µm
SEM MAG: 100 x
Date(m/d/y): 05/14/19
ITAM

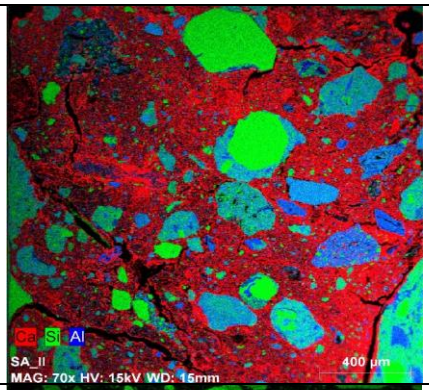
Ca Si Al
SA_II
MAG: 70x HV: 15kV WD: 15mm
400 µm

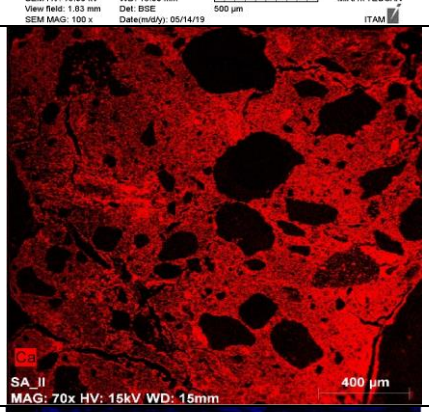
Ca
SA_II
MAG: 70x HV: 15kV WD: 15mm
400 µm

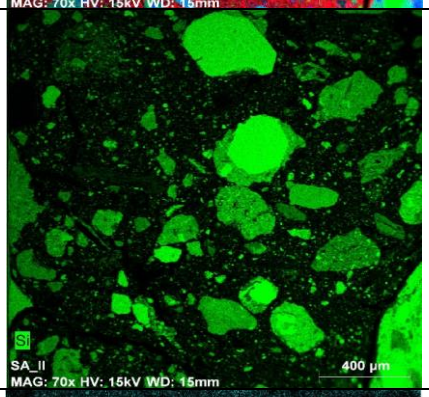
Si
SA_II
MAG: 70x HV: 15kV WD: 15mm
400 µm

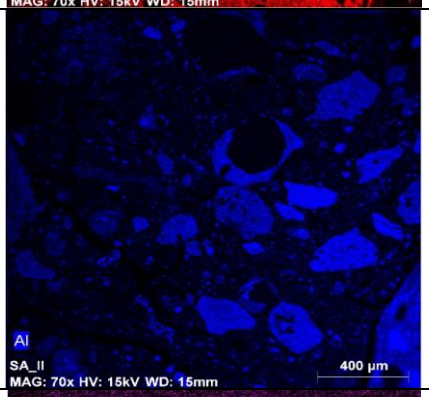
Al
SA_II
MAG: 70x HV: 15kV WD: 15mm
400 µm


Mg
SA_II
MAG: 70x HV: 15kV WD: 15mm
400 µm

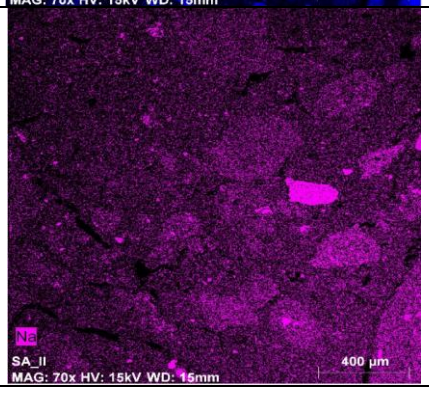
Na
SA_II
MAG: 70x HV: 15kV WD: 15mm
400 µm

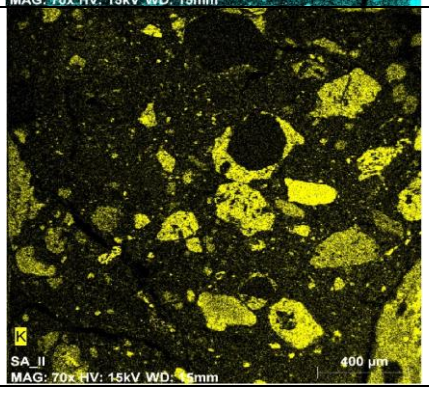
K
SA_II
MAG: 70x HV: 15kV WD: 15mm
400 µm

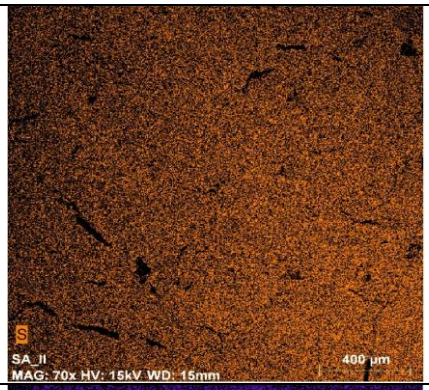
S
SA_II
MAG: 70x HV: 15kV WD: 15mm
400 µm

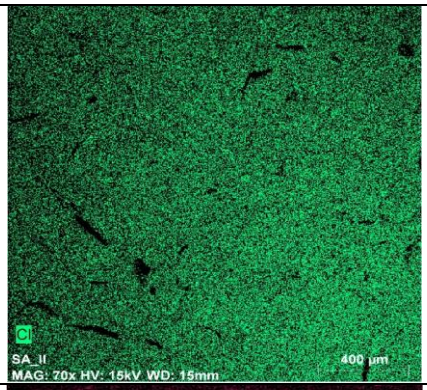
Cl
SA_II
MAG: 70x HV: 15kV WD: 15mm
400 µm

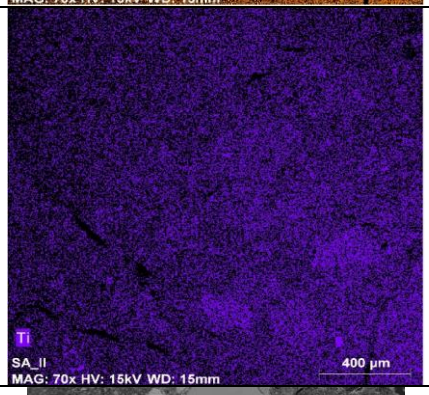
Ti
SA_II
MAG: 70x HV: 15kV WD: 15mm
400 µm

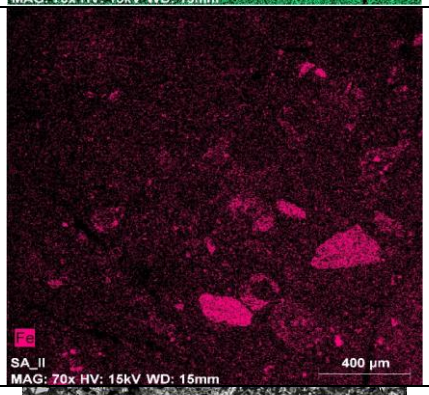
Fe
SA_II
MAG: 70x HV: 15kV WD: 15mm
400 µm

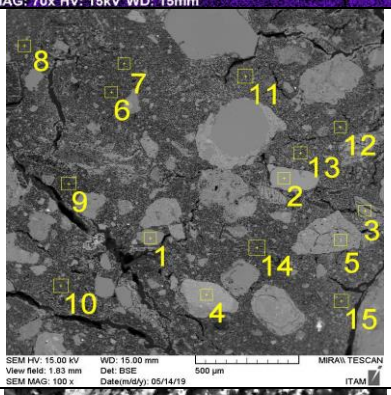
8
7
6
11
12
13
2
9
3
1
14
5
10
4
15
SEM HV: 15.00 kV
View field: 1.83 mm
SEM MAG: 100 x
WD: 15.00 mm
Det: BSE
Date(m/d/y): 05/14/19
500 µm
MIRA\\ TESCAN
ITAM

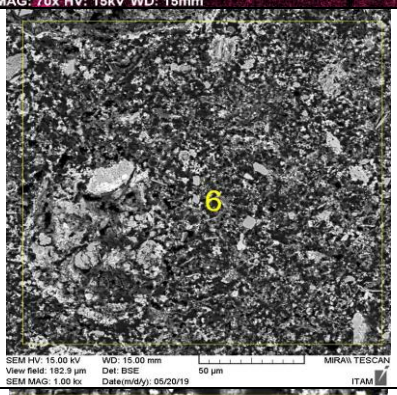
6
SEM HV: 15.00 kV
View field: 182.9 µm
SEM MAG: 1.00 kx
WD: 15.00 mm
Det: BSE
Date(m/d/y): 05/20/19
50 µm
MIRA\\ TESCAN
ITAM

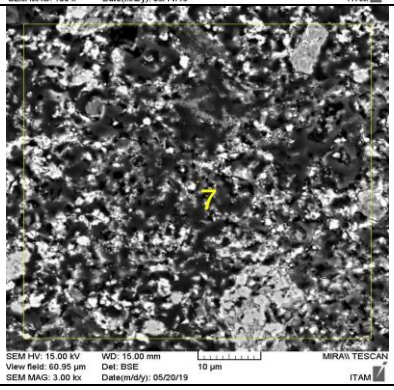
7
SEM HV: 15.00 kV
View field: 60.95 µm
SEM MAG: 3.00 kx
WD: 15.00 mm
Det: BSE
Date(m/d/y): 05/20/19
10 µm
MIRA\\ TESCAN
ITAM

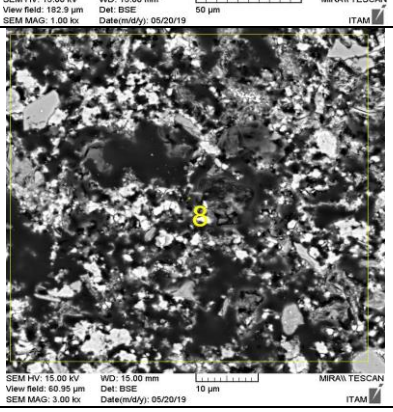
8
SEM HV: 15.00 kV
View field: 60.95 µm
SEM MAG: 3.00 kx
WD: 15.00 mm
Det: BSE
Date(m/d/y): 05/20/19
10 µm
MIRA\\ TESCAN
ITAM

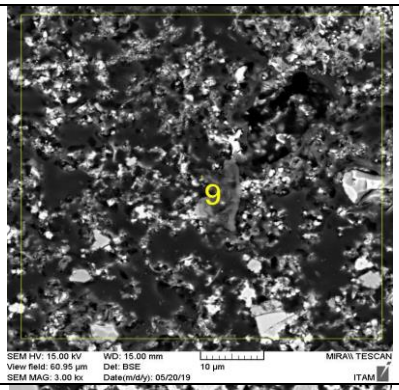
9
SEM HV: 15.00 kV
View field: 60.95 µm
SEM MAG: 3.00 kx
WD: 15.00 mm
Det: BSE
Date(m/d/y): 05/20/19
10 µm
MIRA\\ TESCAN
ITAM

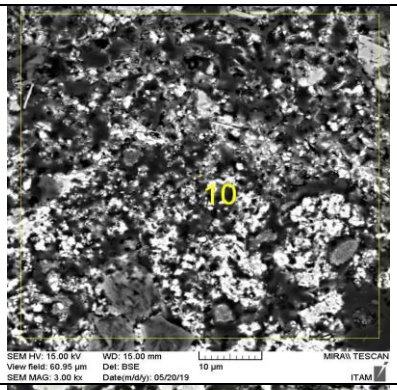
10
SEM HV: 15.00 kV
View field: 60.95 µm
SEM MAG: 3.00 kx
WD: 15.00 mm
Det: BSE
Date(m/d/y): 05/20/19
10 µm
MIRA\\ TESCAN
ITAM

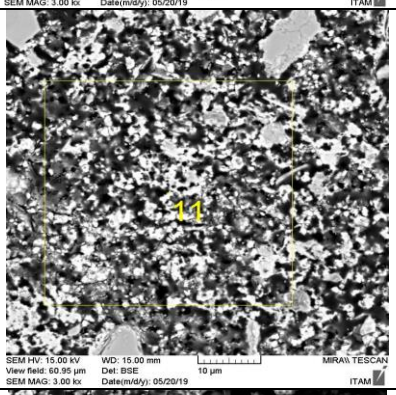
11
SEM HV: 15.00 kV
View field: 60.95 µm
SEM MAG: 3.00 kx
WD: 15.00 mm
Det: BSE
Date(m/d/y): 05/20/19
10 µm
MIRA\\ TESCAN
ITAM

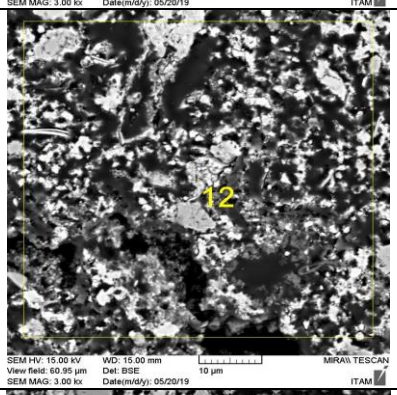
12
SEM HV: 15.00 kV
View field: 60.95 µm
SEM MAG: 3.00 kx
WD: 15.00 mm
Det: BSE
Date(m/d/y): 05/20/19
10 µm
MIRA\\ TESCAN
ITAM

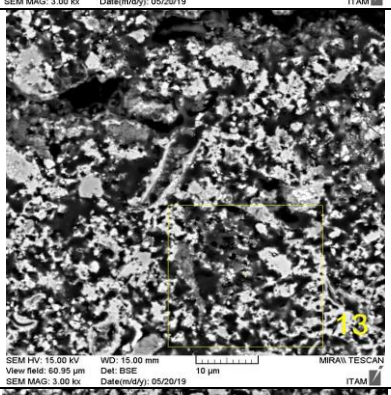
13
SEM HV: 15.00 kV
View field: 60.95 µm
SEM MAG: 3.00 kx
WD: 15.00 mm
Det: BSE
Date(m/d/y): 05/20/19
10 µm
MIRA\\ TESCAN
ITAM

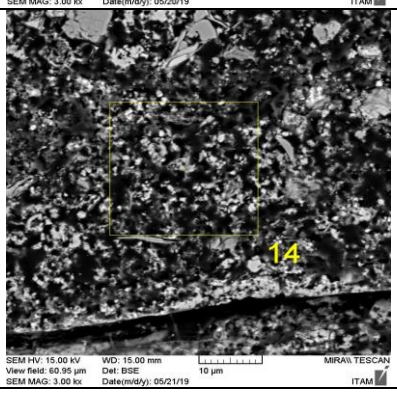
14
SEM HV: 15.00 kV
View field: 60.95 µm
SEM MAG: 3.00 kx
WD: 15.00 mm
Det: BSE
Date(m/d/y): 05/21/19
10 µm
MIRA\\ TESCAN
ITAM

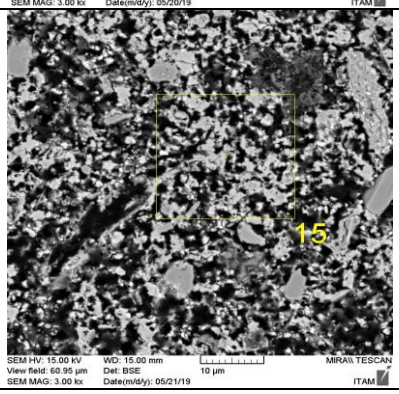
15
SEM HV: 15.00 kV
View field: 60.95 µm
SEM MAG: 3.00 kx
WD: 15.00 mm
Det: BSE
Date(m/d/y): 05/21/19
10 µm
MIRA\\ TESCAN
ITAM

Appendix C: Detailed Micro-scale Model Results

Mortar w/ Stone Range (m²):	0.001
Micro-Scale Model #:	1

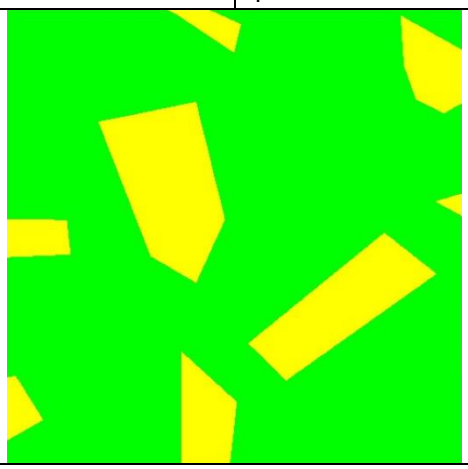

Compression Test – Peak = Step 22

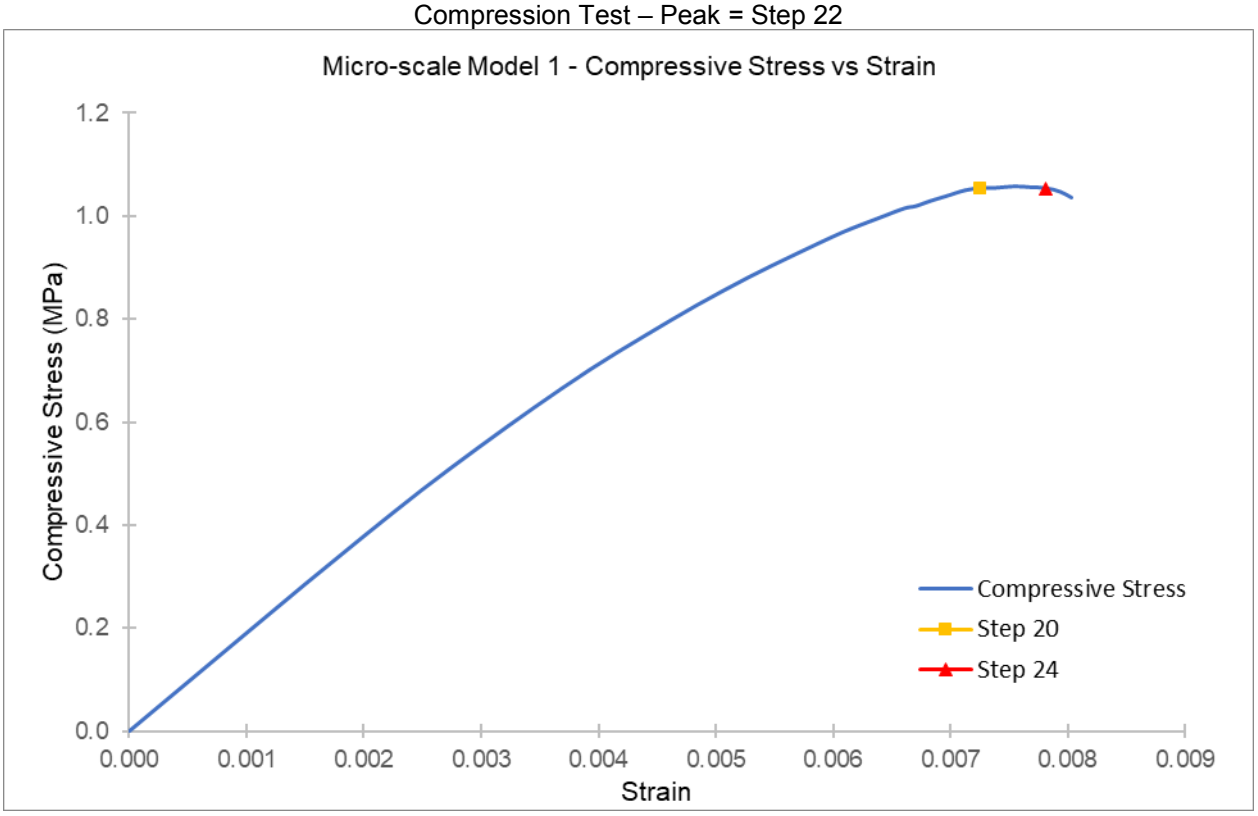

Crack Width

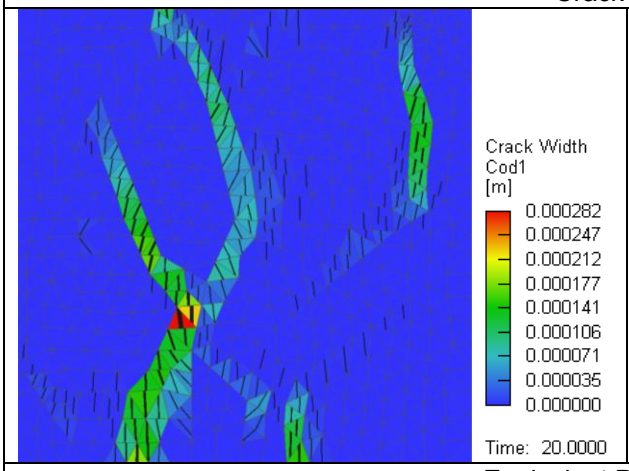

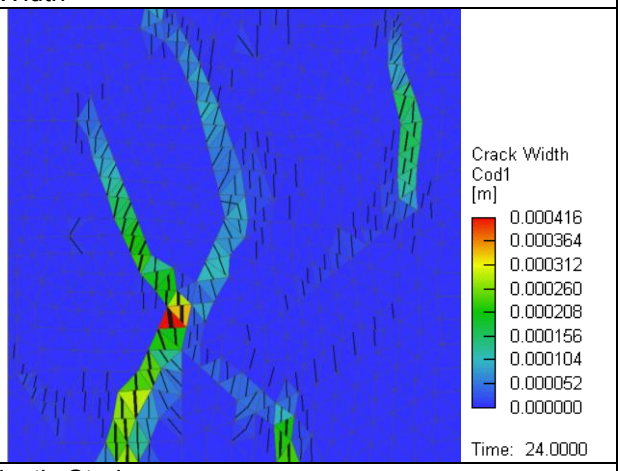

Equivalent Plastic Strain

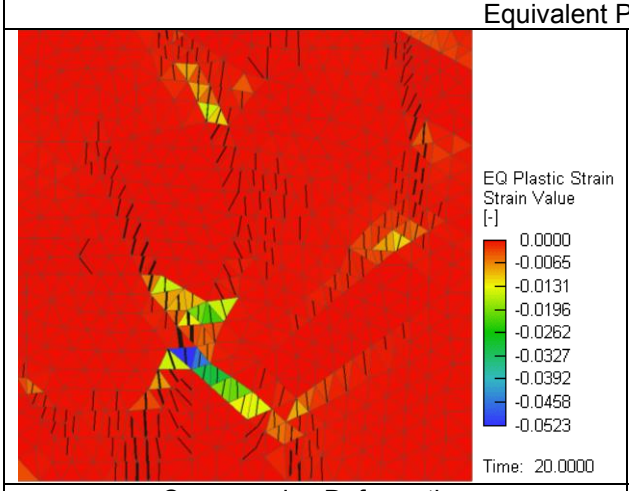

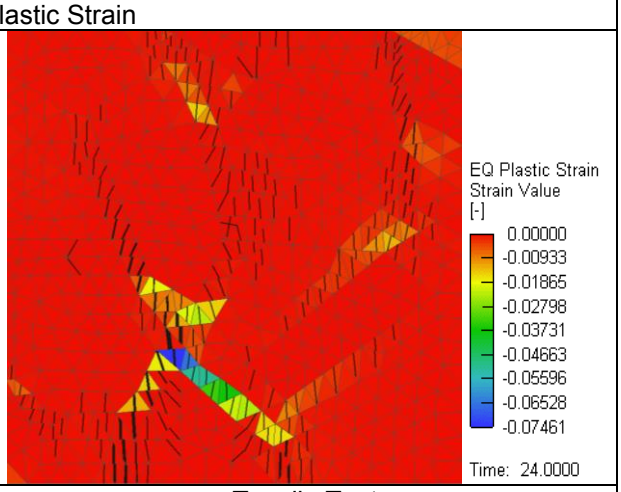

Compressive Deformation

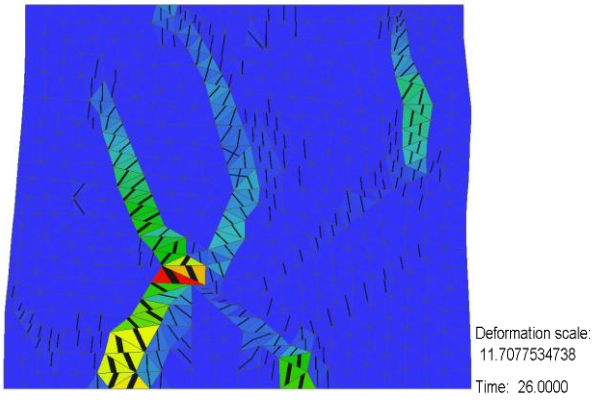

Tensile Test

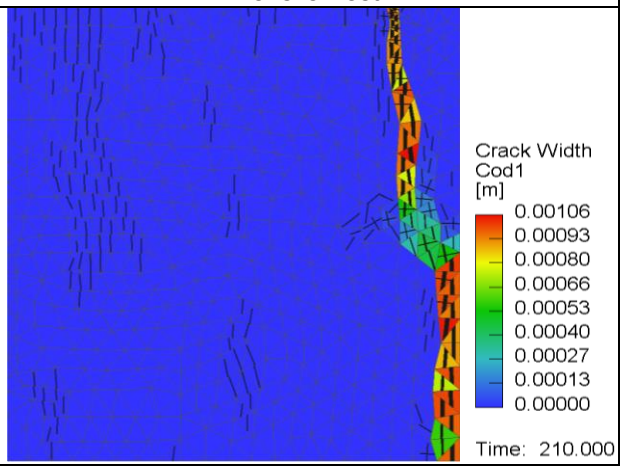

Mortar w/ Stone Range (m²):	0.001
Micro-scale Model #:	2

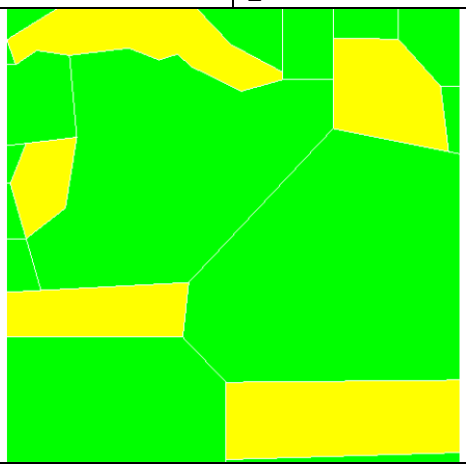

Compression Test – Peak = Step 80

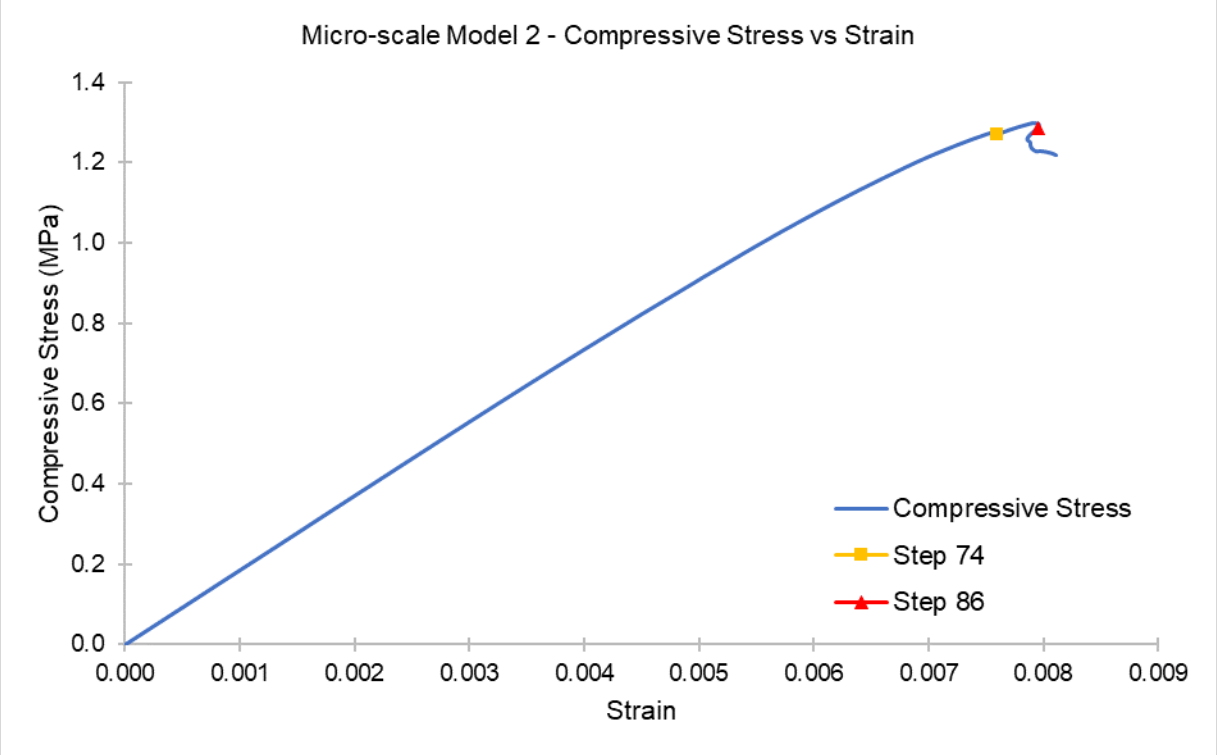

Crack Width

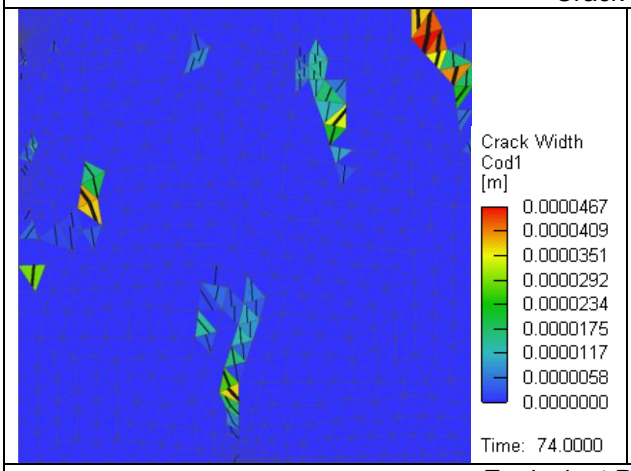

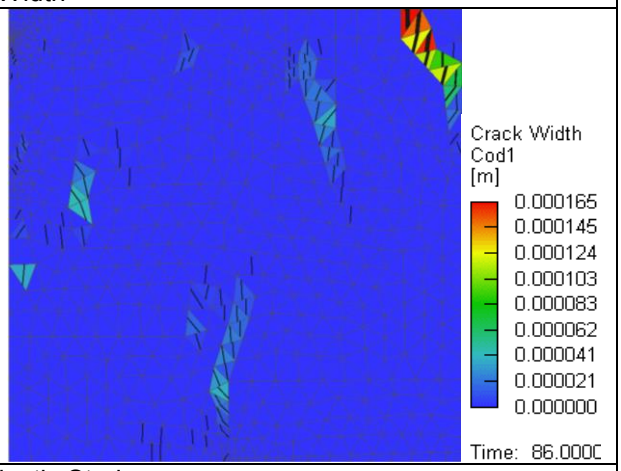

Equivalent Plastic Strain

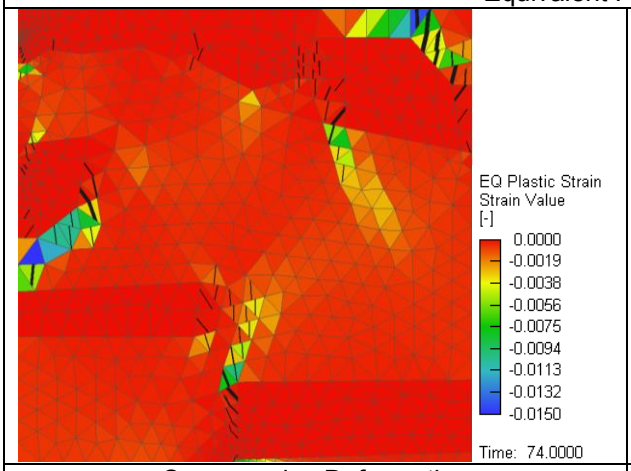

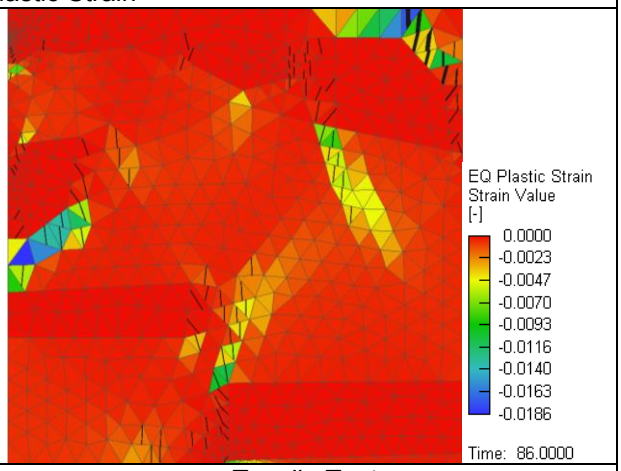

Compressive Deformation

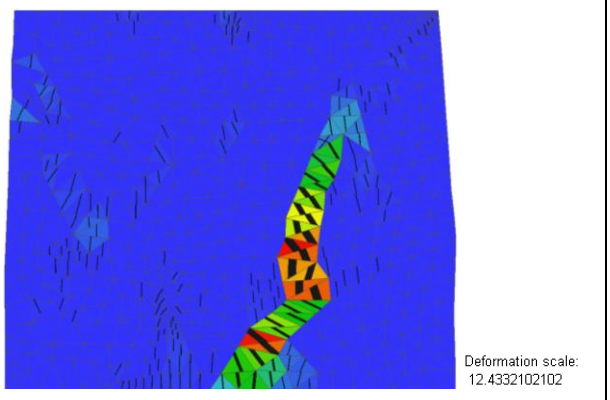

Tensile Test

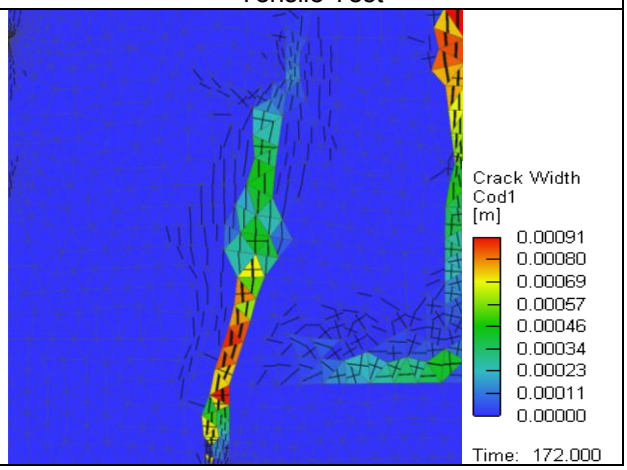

Mortar w/ Stone Range (m²):	0.001
Micro-scale Model #:	3

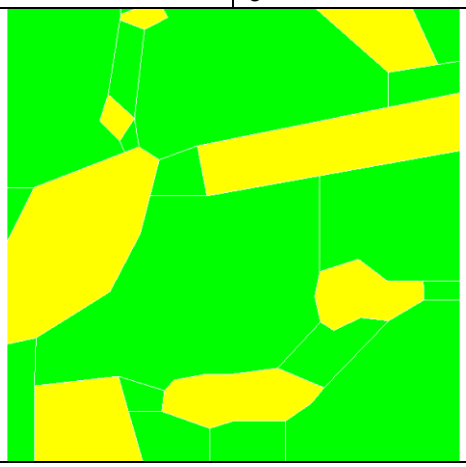

Compression Test – Peak = Step 30

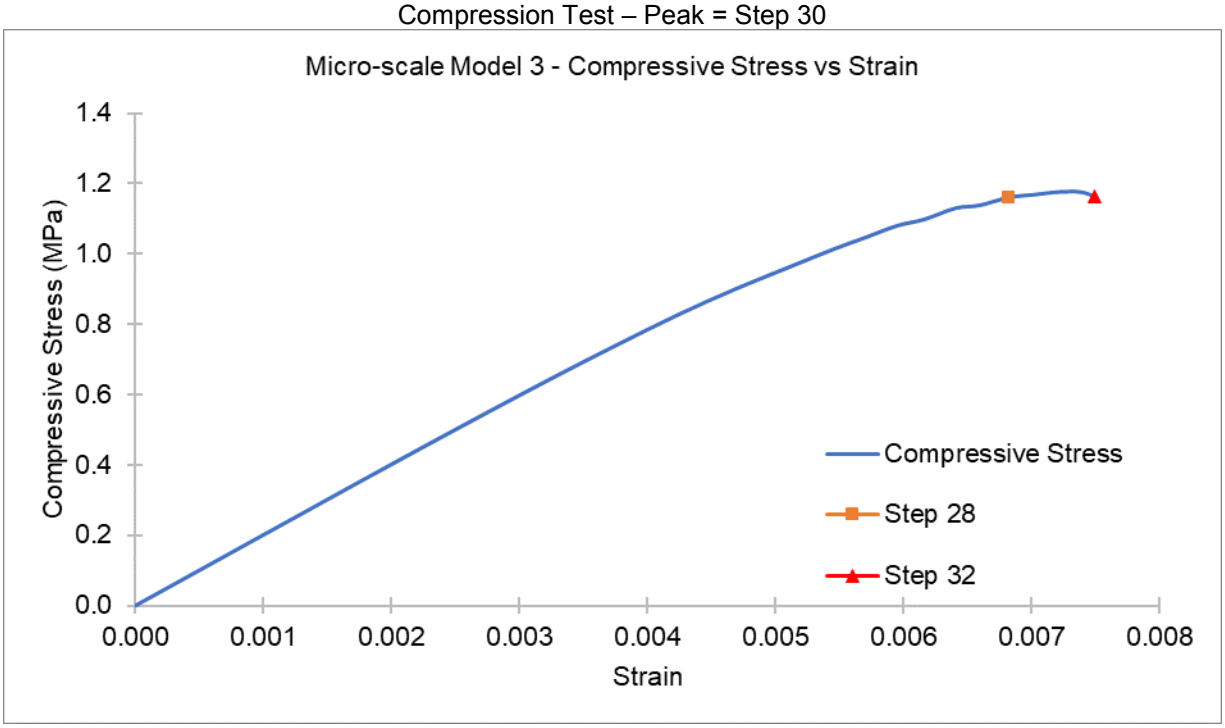

Crack Width

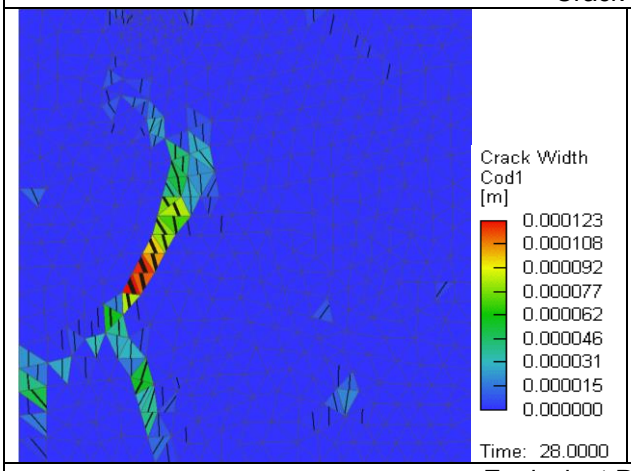

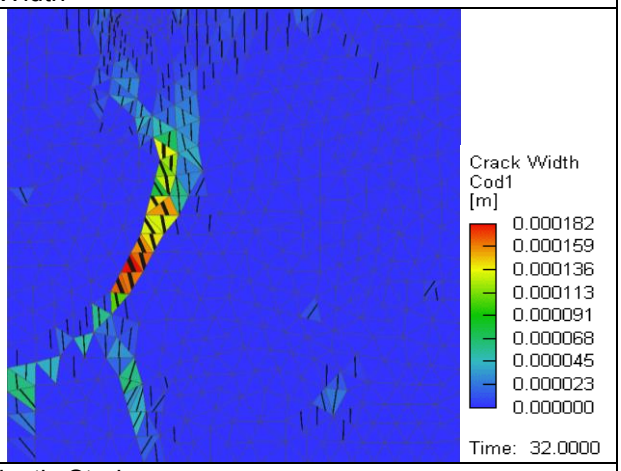

Equivalent Plastic Strain

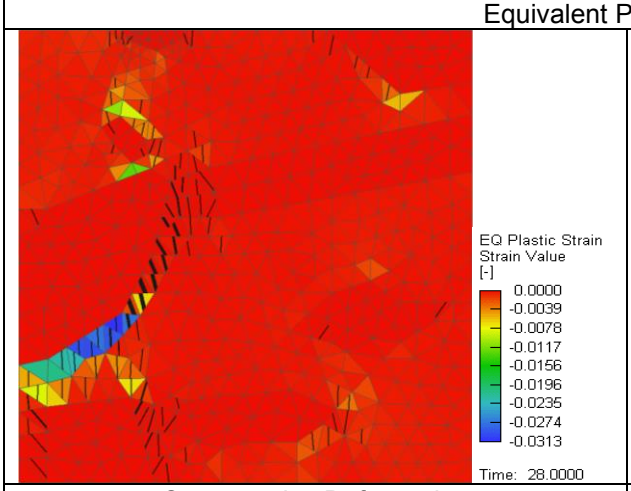

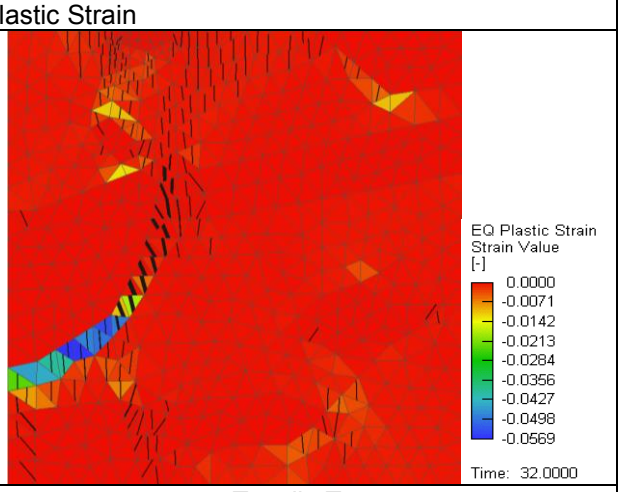

Compressive Deformation

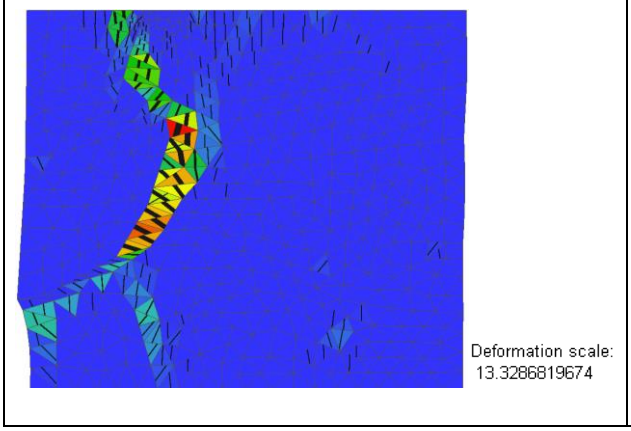

Tensile Test

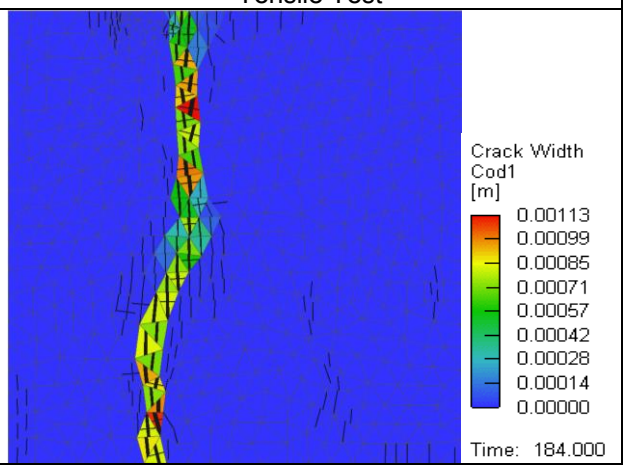

Mortar w/ Stone Range (m²):	0.001
Micro-scale Model #:	4

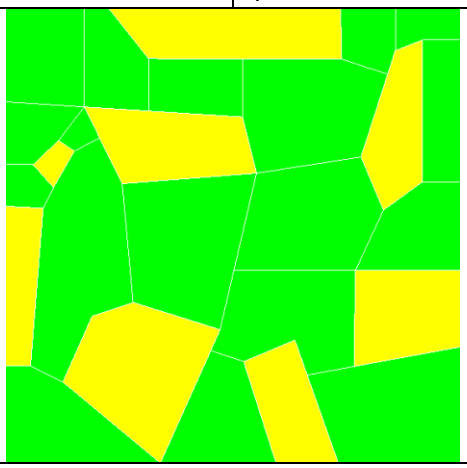

Compression Test – Peak = Step 45

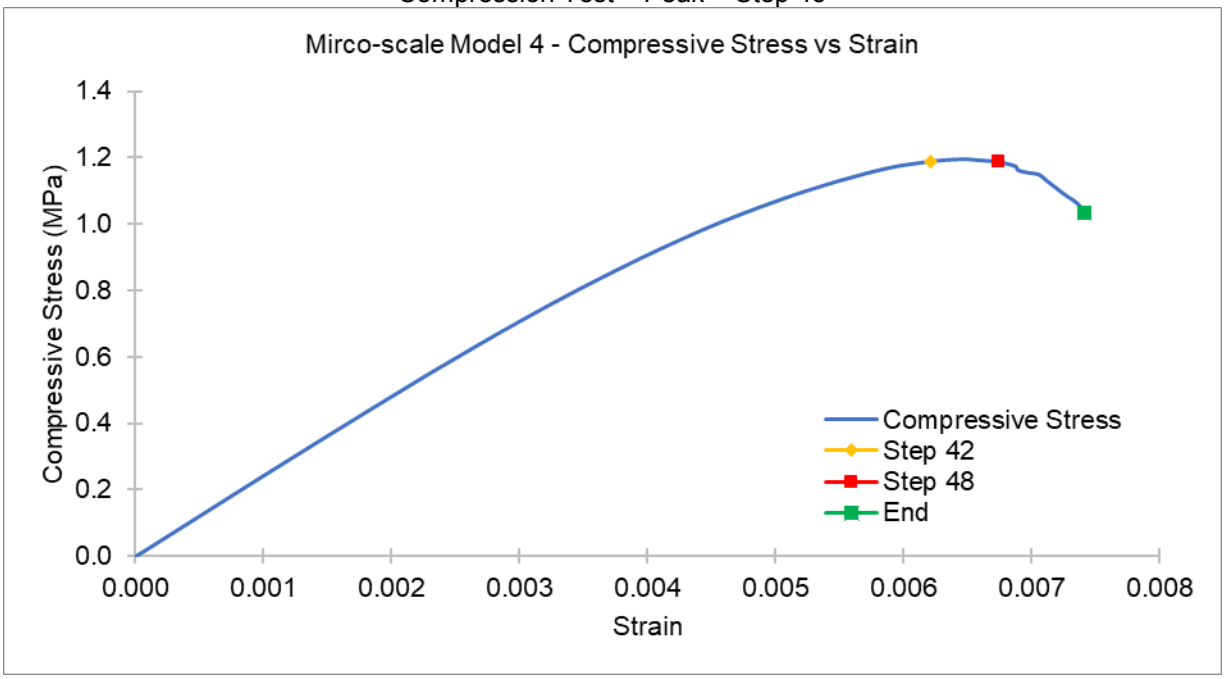

Crack Width

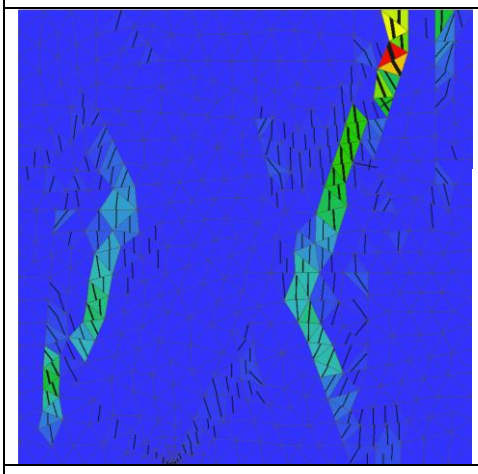

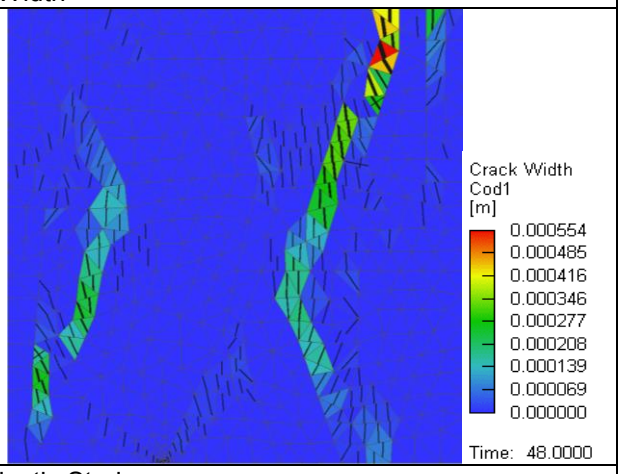

Equivalent Plastic Strain

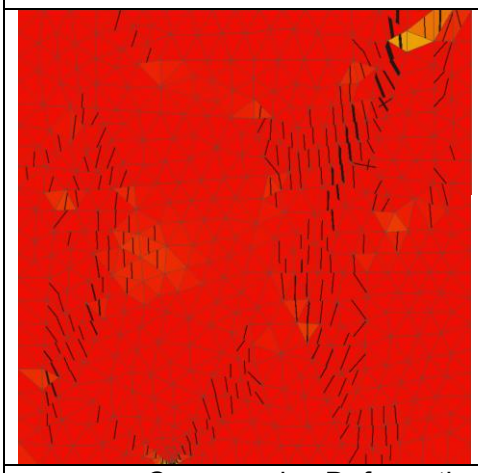

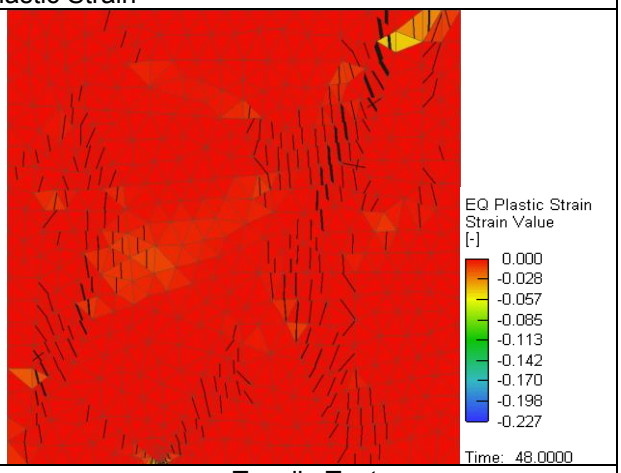

Compressive Deformation

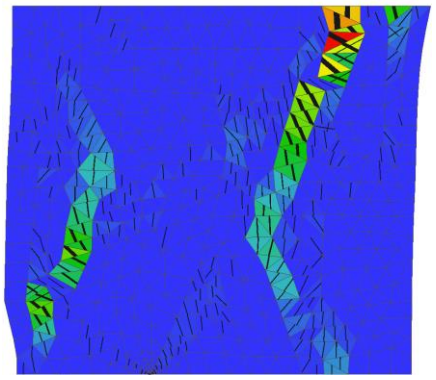

Tensile Test

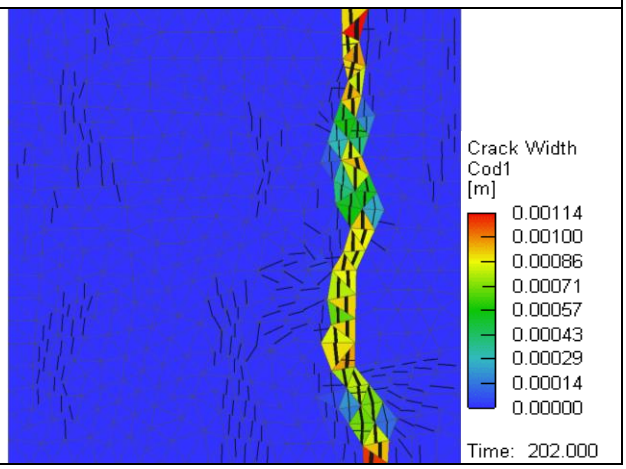

Mortar w/ Stone Range (m²):	0.001
Micro-scale Model #:	5

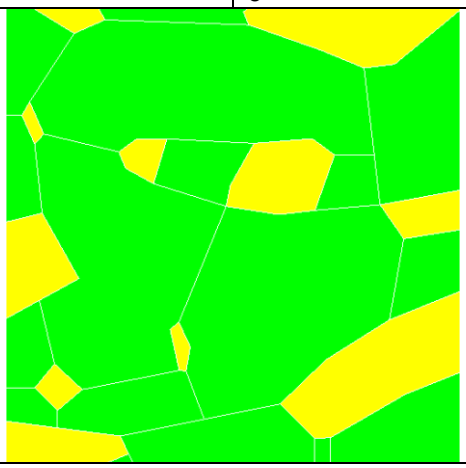

Compression Test – Peak = Step 133

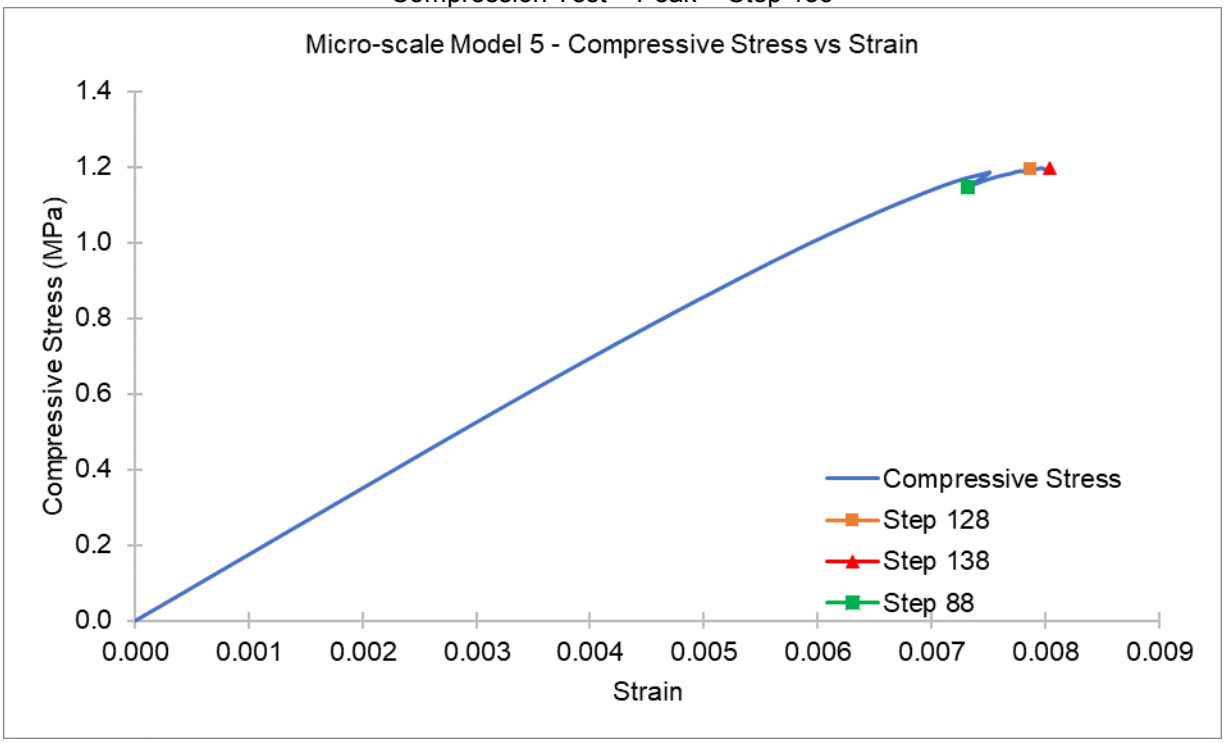

Crack Width

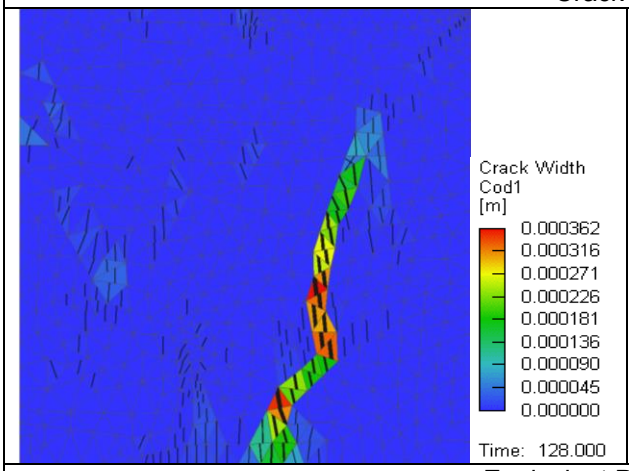

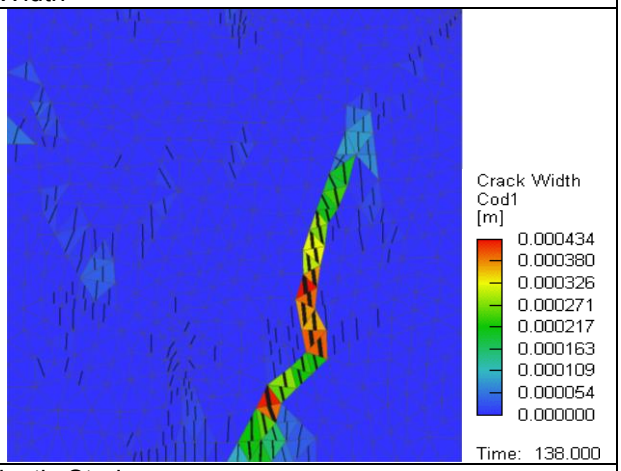

Equivalent Plastic Strain

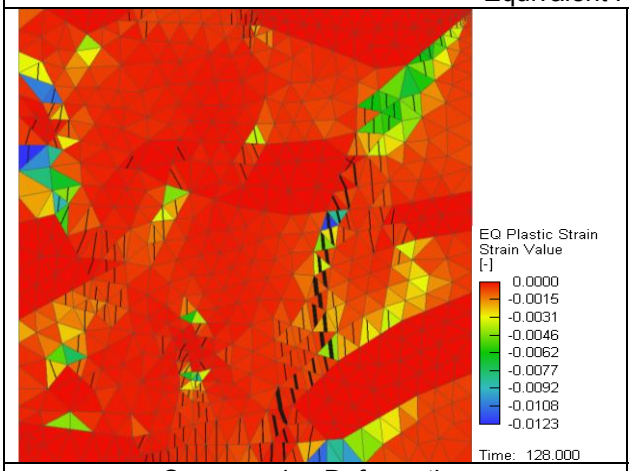

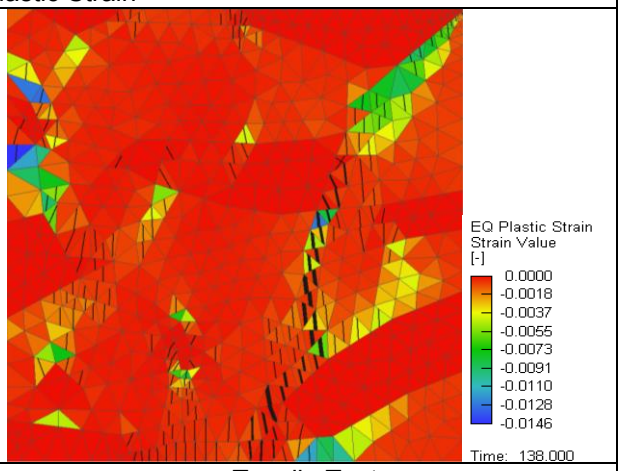

Compressive Deformation

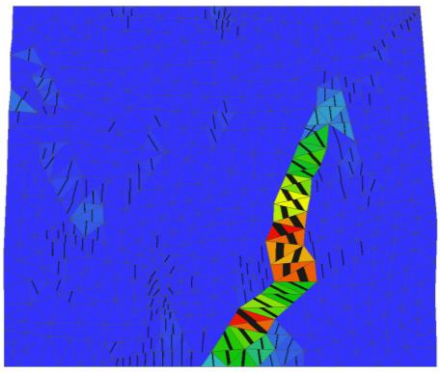

Tensile Test

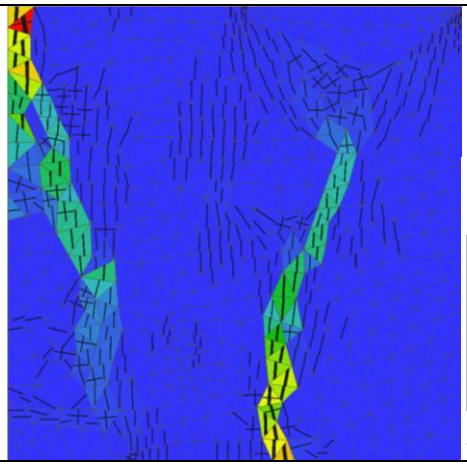

Mortar w/ Stone Range (m²):	0.002
Micro-scale Model #:	1

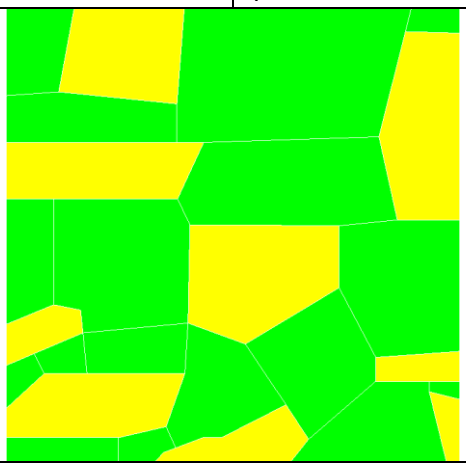

Compression Test – Peak = Step 54

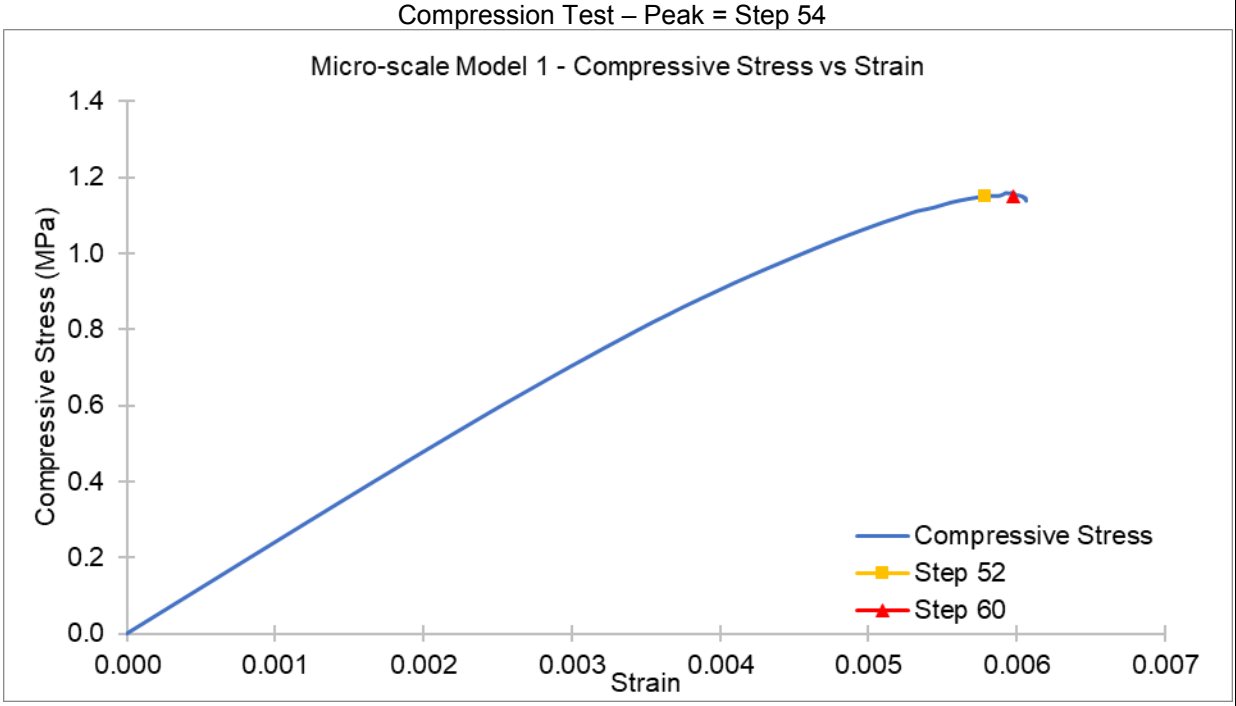

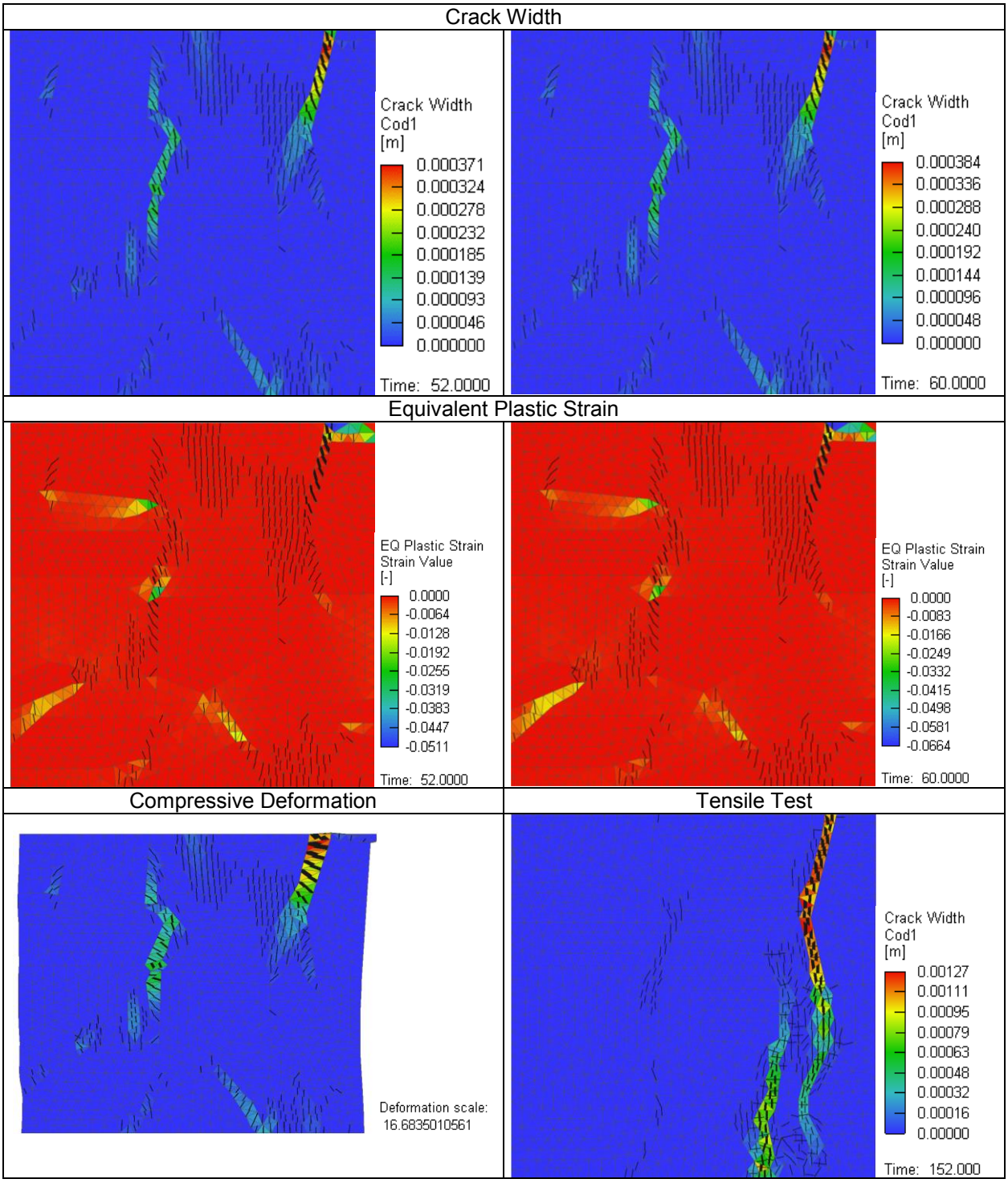
Crack Width
Crack Width
Cod1
[m]
0.000371
0.000324
0.000278
0.000232
0.000185
0.000139
0.000093
0.000046
0.000000
Time: 52.0000
Crack Width
Cod1
[m]
0.000384
0.000336
0.000288
0.000240
0.000192
0.000144
0.000096
0.000048
0.000000
Time: 60.0000
Equivalent Plastic Strain
EQ Plastic Strain
Strain Value
[-]
0.0000
-0.0064
-0.0128
-0.0192
-0.0255
-0.0319
-0.0383
-0.0447
-0.0511
Time: 52.0000
EQ Plastic Strain
Strain Value
[-]
0.0000
-0.0083
-0.0166
-0.0249
-0.0332
-0.0415
-0.0498
-0.0581
-0.0664
Time: 60.0000
Compressive Deformation
Deformation scale:
16.6835010561
Tensile Test
Crack Width
Cod1
[m]
0.00127
0.00111
0.00095
0.00079
0.00063
0.00048
0.00032
0.00016
0.00000
Time: 152.000

Mortar w/ Stone Range (m²):	0.002
Micro-scale Model #:	2

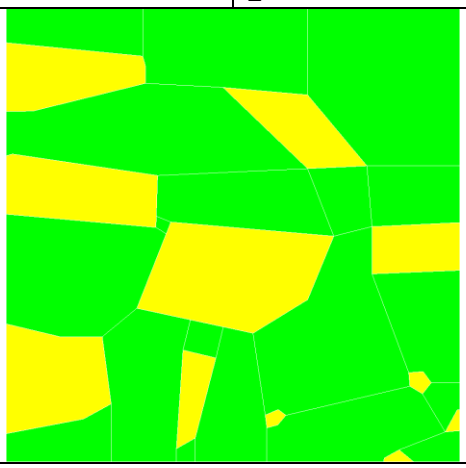

Compression Test – Peak = Step 48

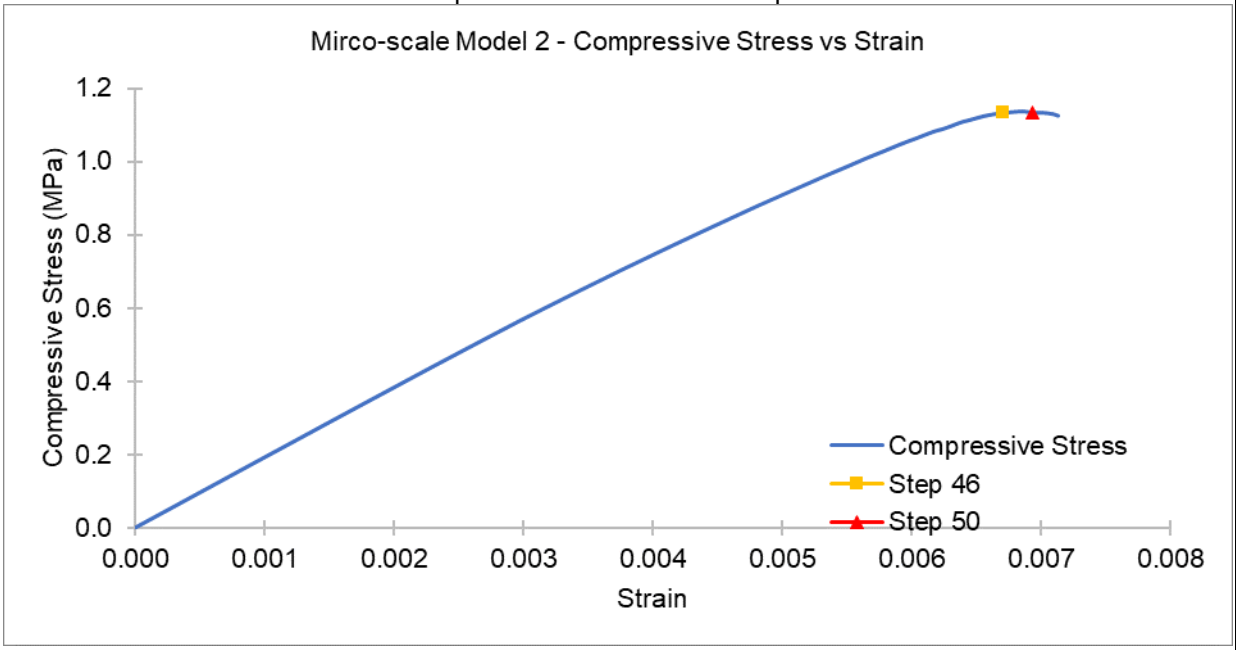

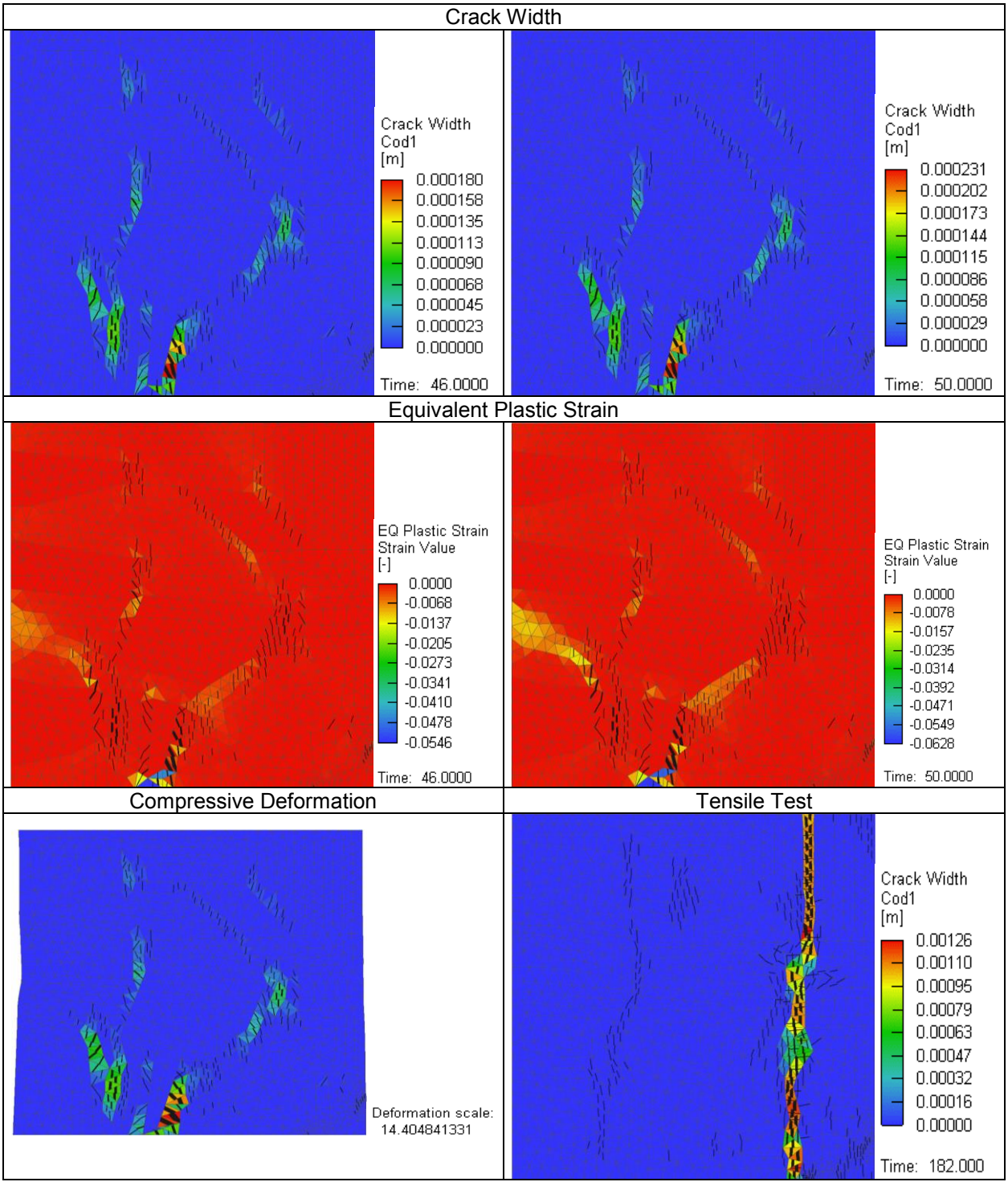
Crack Width
Crack Width
Cod1
[m]
0.000180
0.000158
0.000135
0.000113
0.000090
0.000068
0.000045
0.000023
0.000000
Time: 46.0000
Crack Width
Cod1
[m]
0.000231
0.000202
0.000173
0.000144
0.000115
0.000086
0.000058
0.000029
0.000000
Time: 50.0000
Equivalent Plastic Strain
EQ Plastic Strain
Strain Value
[-]
0.0000
-0.0068
-0.0137
-0.0205
-0.0273
-0.0341
-0.0410
-0.0478
-0.0546
Time: 46.0000
EQ Plastic Strain
Strain Value
[-]
0.0000
-0.0078
-0.0157
-0.0235
-0.0314
-0.0392
-0.0471
-0.0549
-0.0628
Time: 50.0000
Compressive Deformation
Deformation scale:
14.404841331
Tensile Test
Crack Width
Cod1
[m]
0.00126
0.00110
0.00095
0.00079
0.00063
0.00047
0.00032
0.00016
0.00000
Time: 182.000

Mortar w/ Stone Range (m²):	0.002
Micro-scale Model #:	3

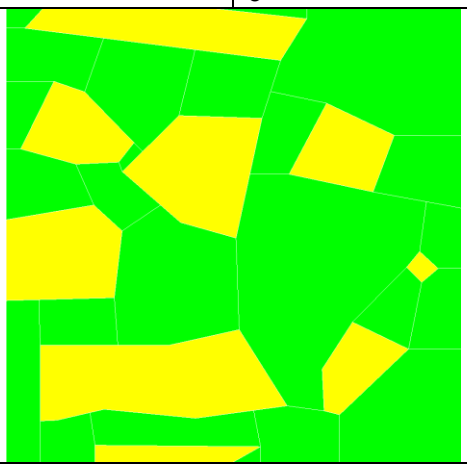

Compression Test – Peak = Step 40

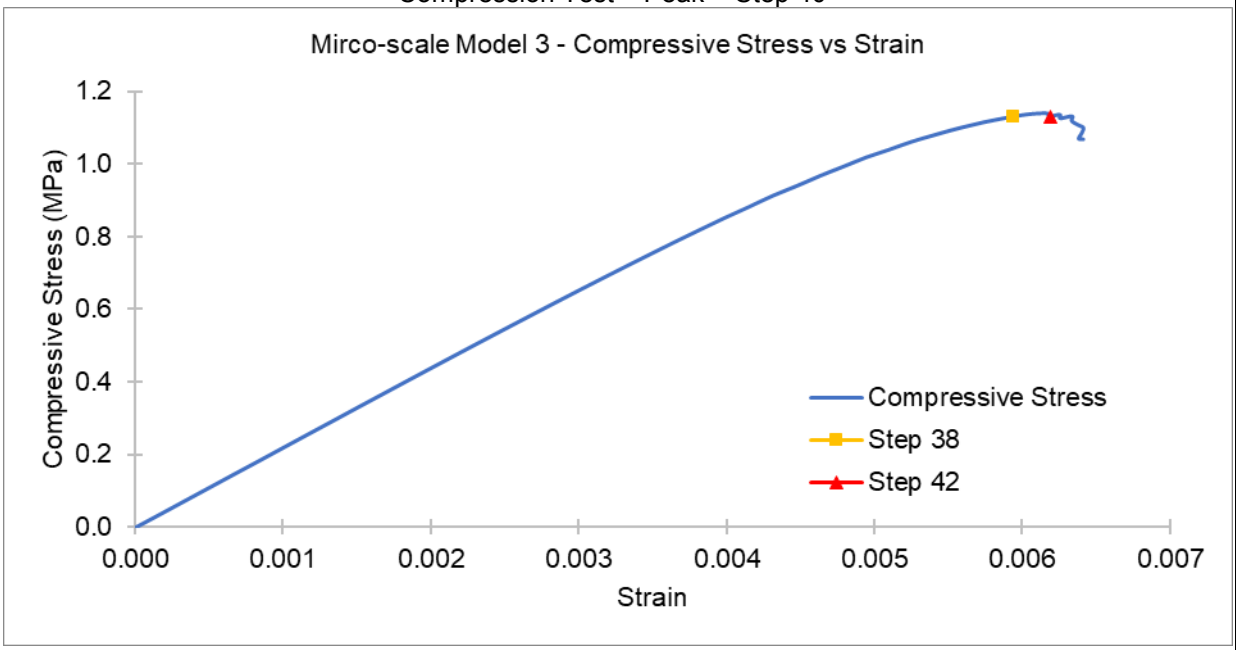

Crack Width

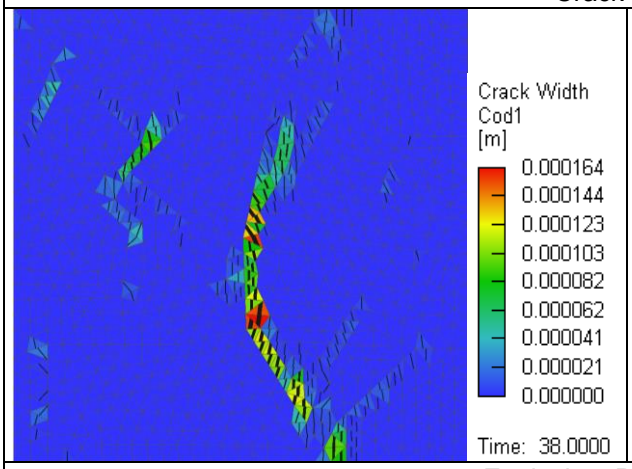

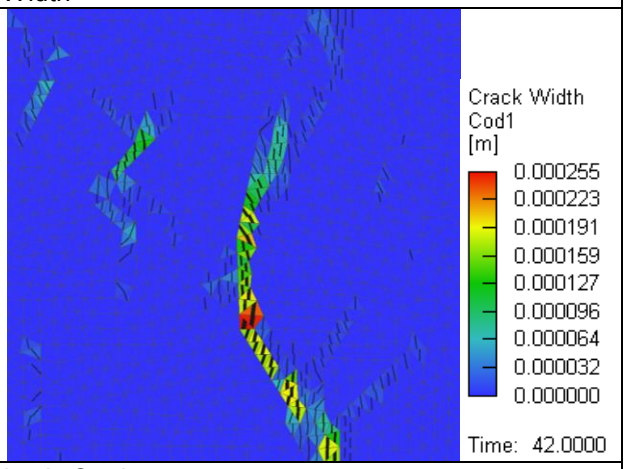

Equivalent Plastic Strain

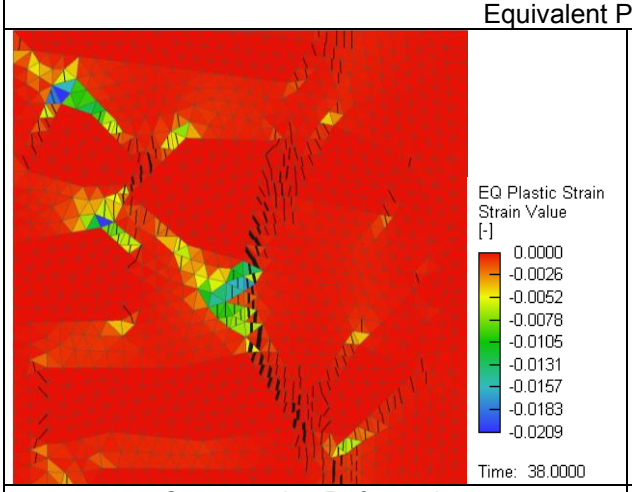

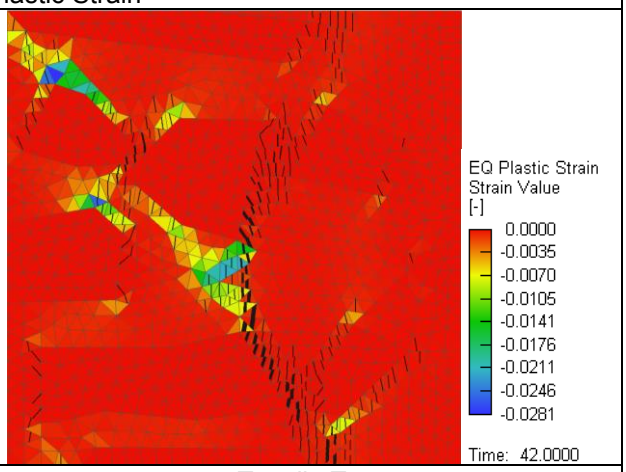

Compressive Deformation

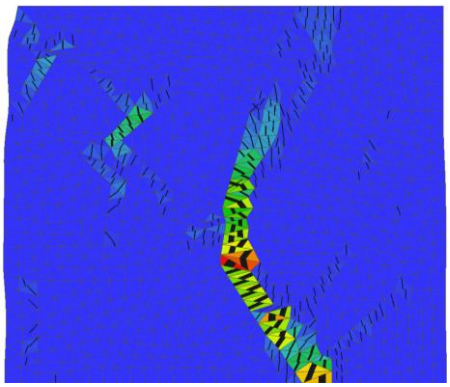

Tensile Test

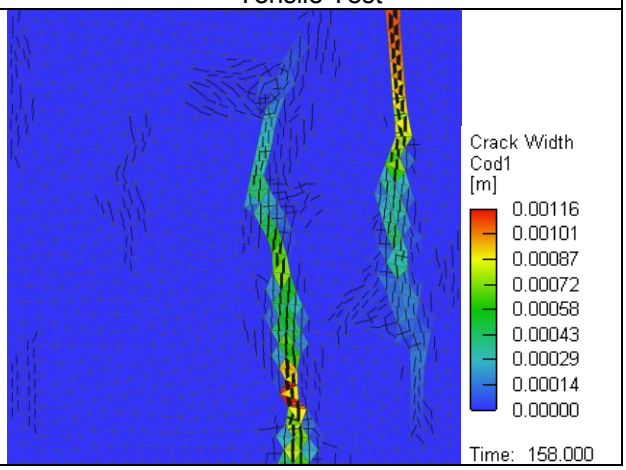

Mortar w/ Stone Range (m²):	0.002
Micro-scale Model #:	4

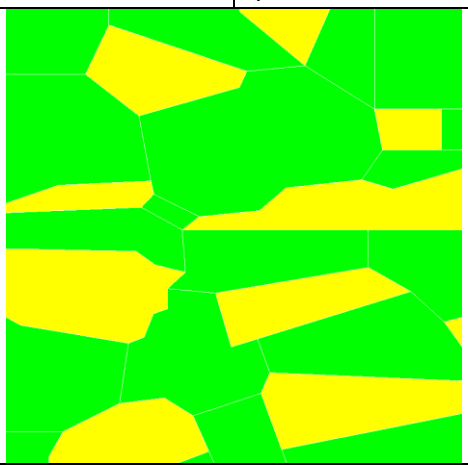

Compression Test – Peak = Step 32

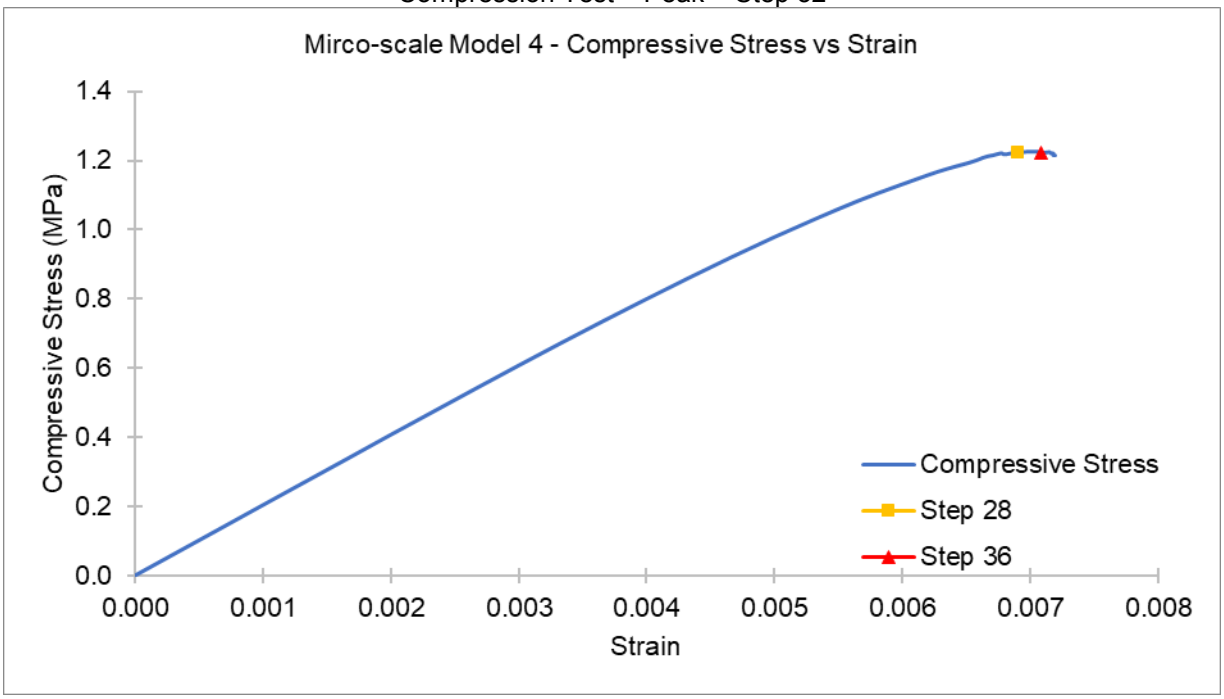

Crack Width

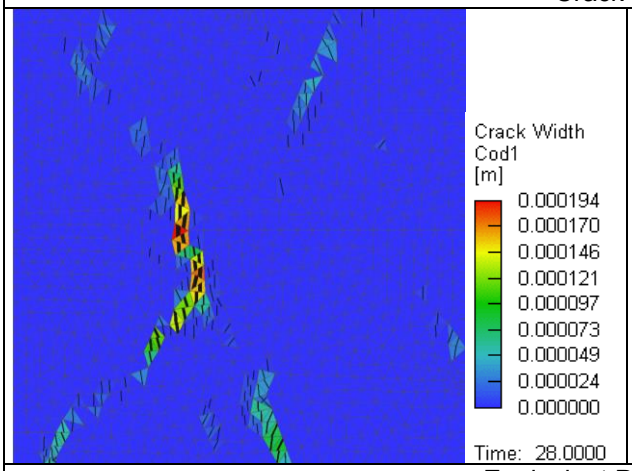

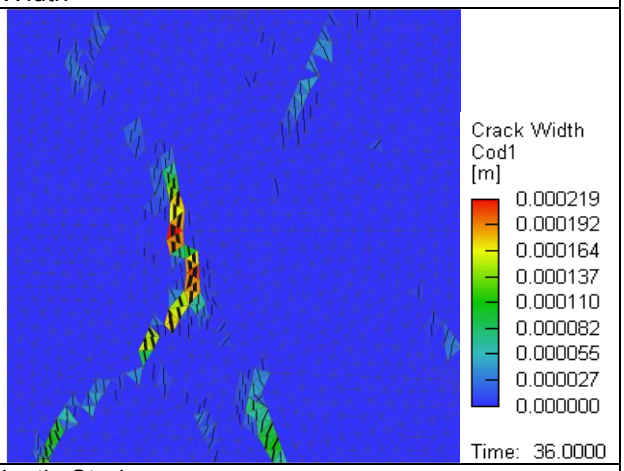

Equivalent Plastic Strain

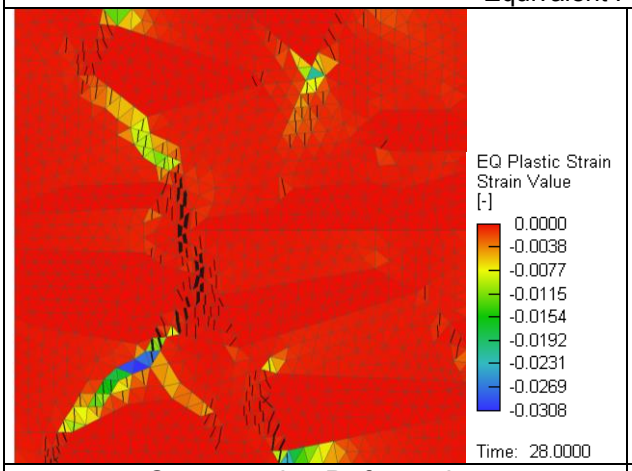

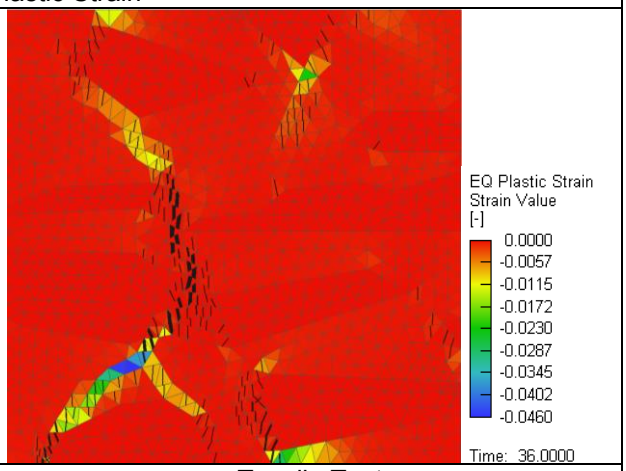

Compressive Deformation

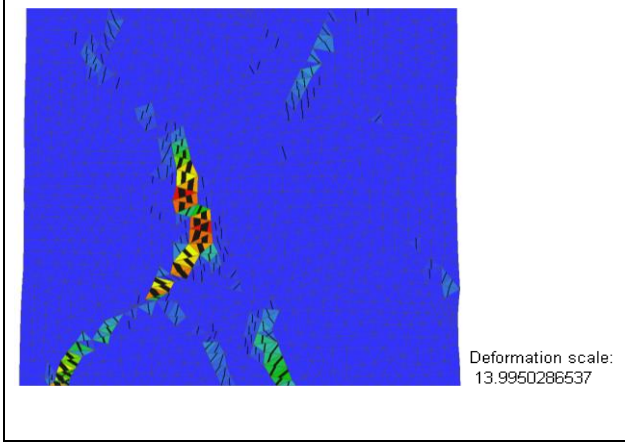

Tensile Test

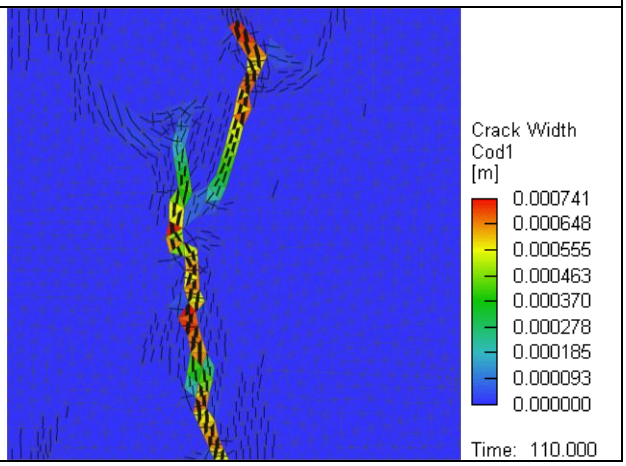

Mortar w/ Stone Range (m²):	0.002
Micro-scale Model #:	5

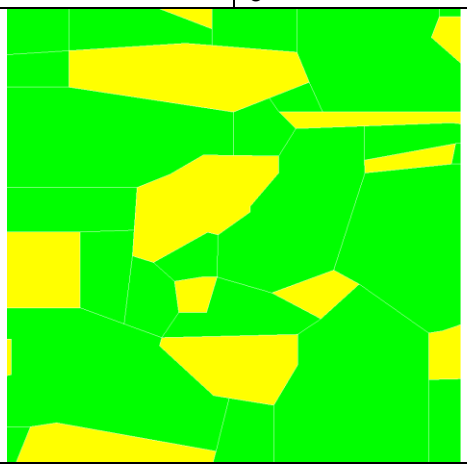

Compression Test – Peak = Step 55

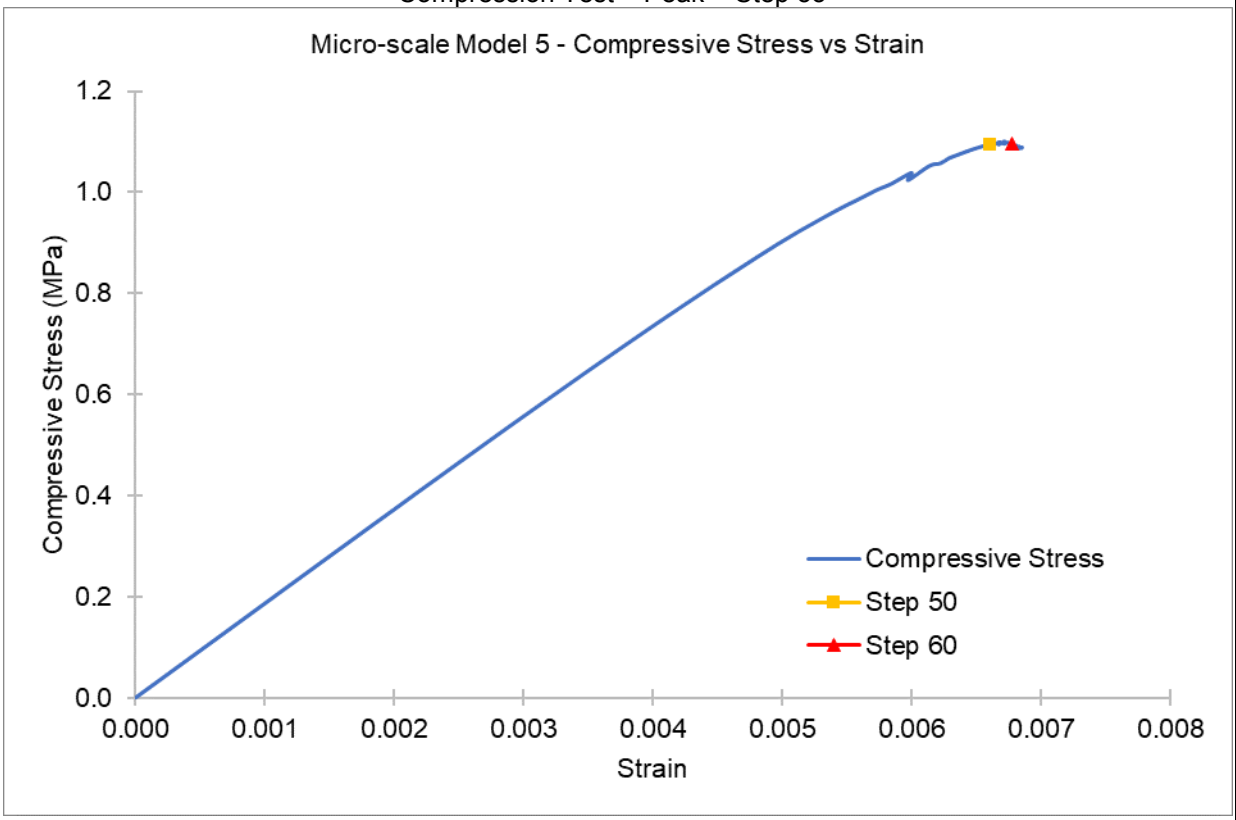

Crack Width

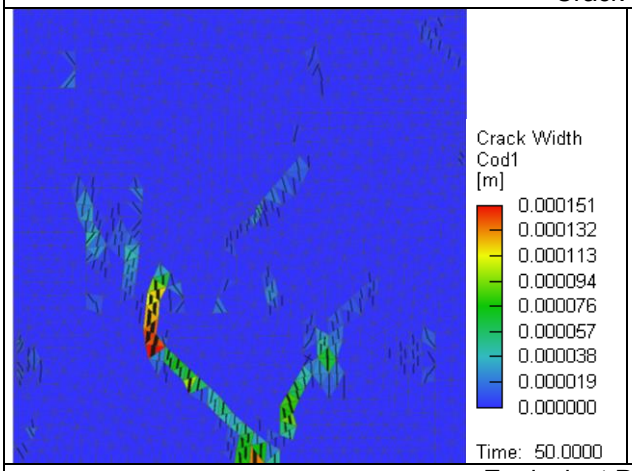

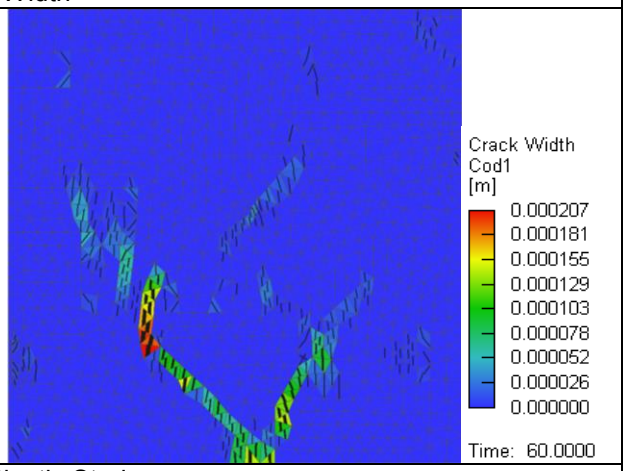

Equivalent Plastic Strain

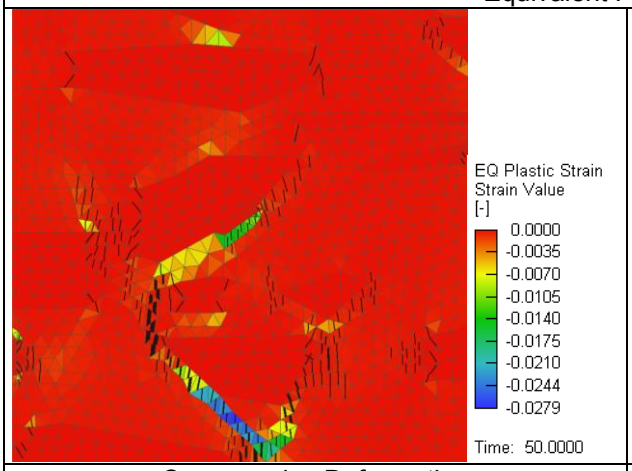

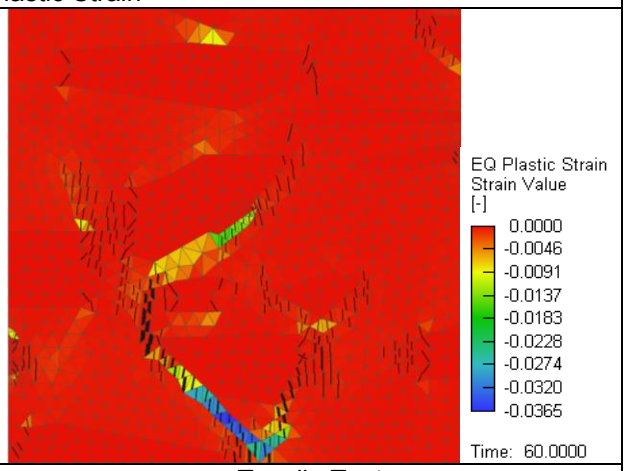

Compressive Deformation

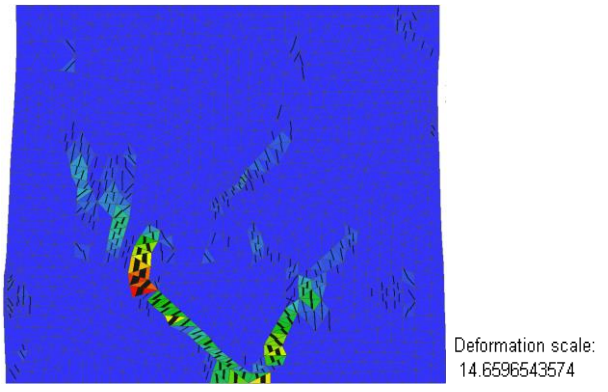

Tensile Test

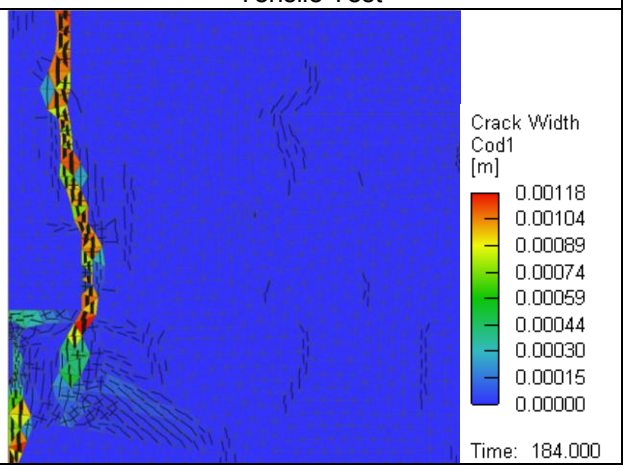

Appendix D: Detailed Meso-scale Model Results

Matrix w/ Stone Range (m²):	0.001
Meso-scale Model #:	1

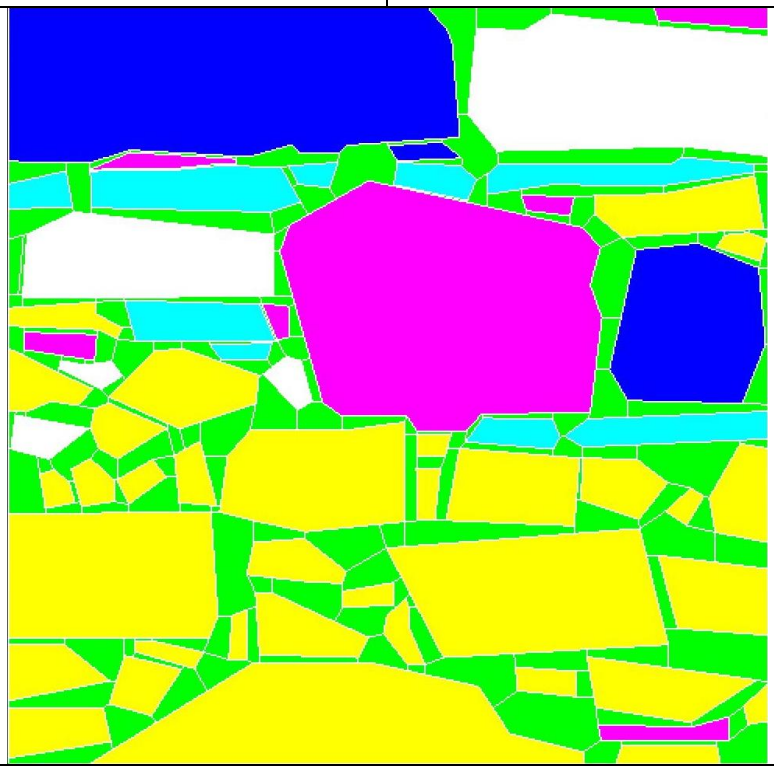

Compression Test – Peak = Step 72

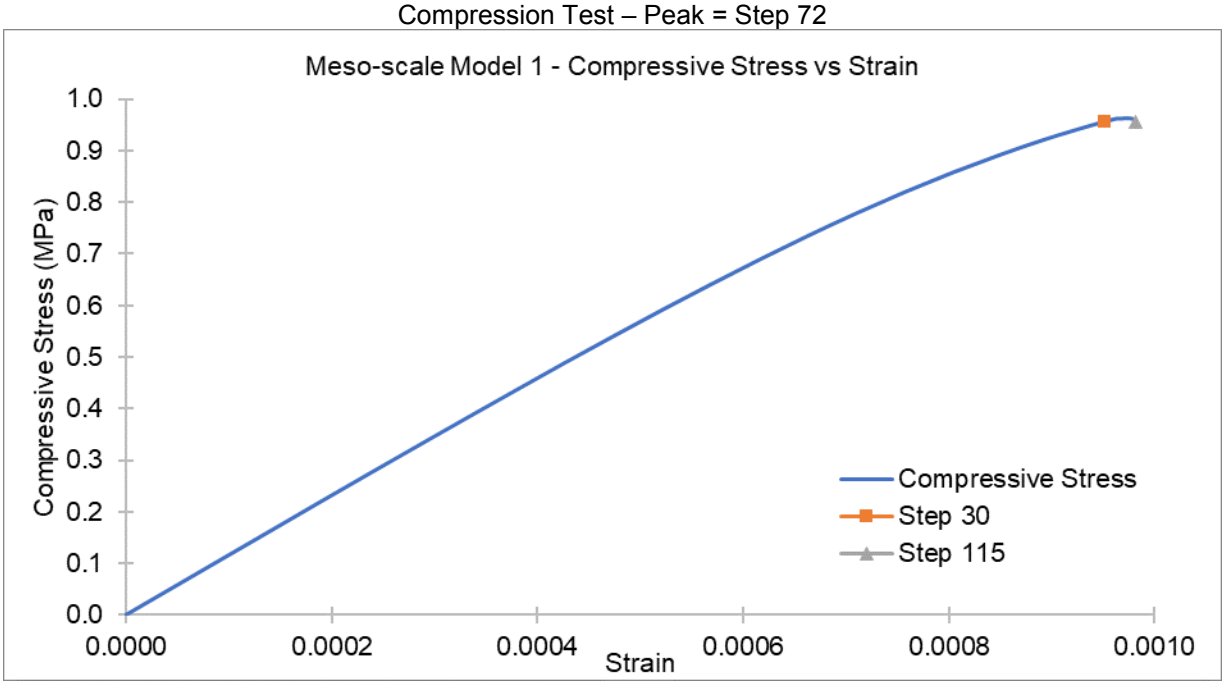

Crack Width

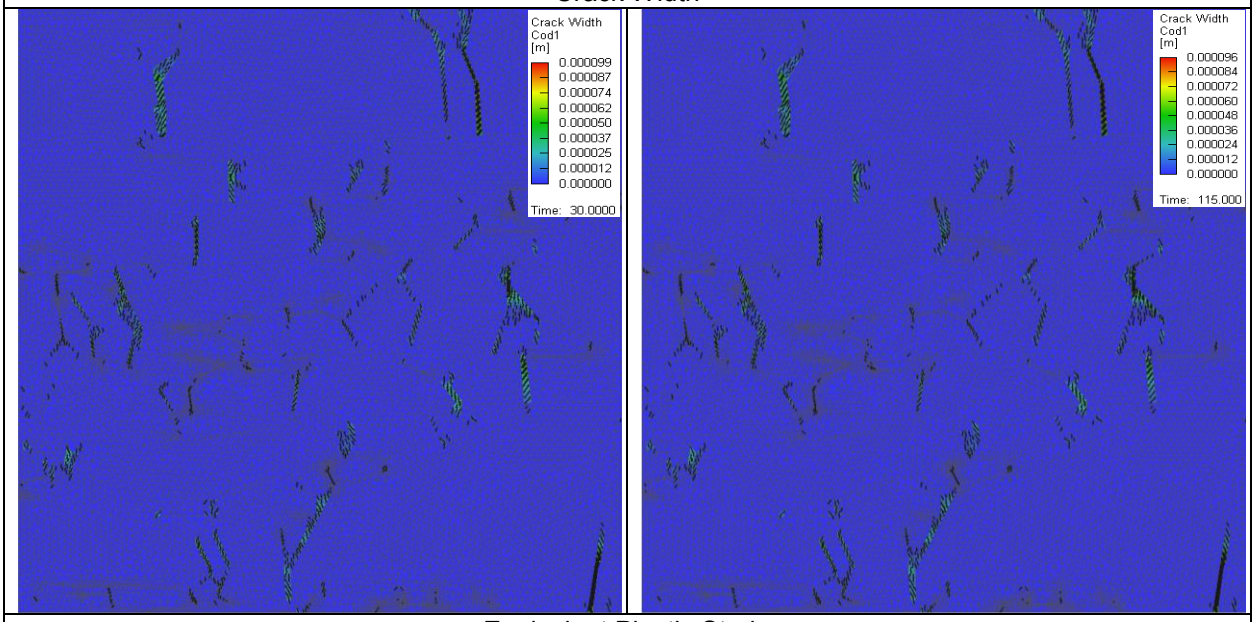

Equivalent Plastic Strain

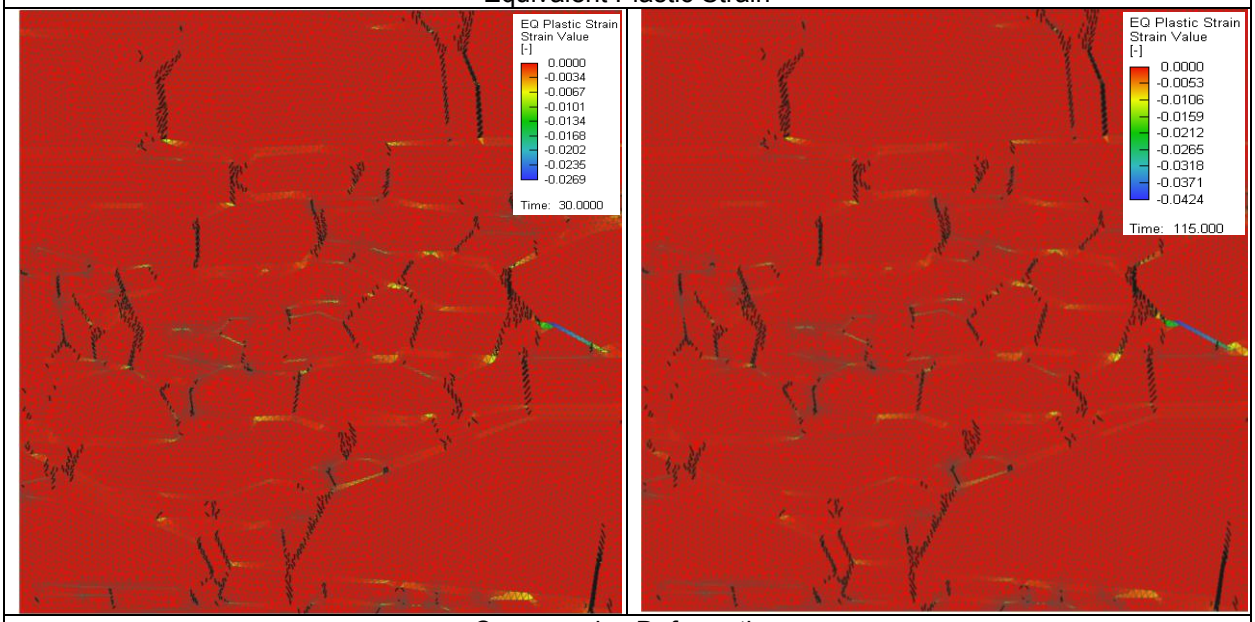

Compressive Deformation

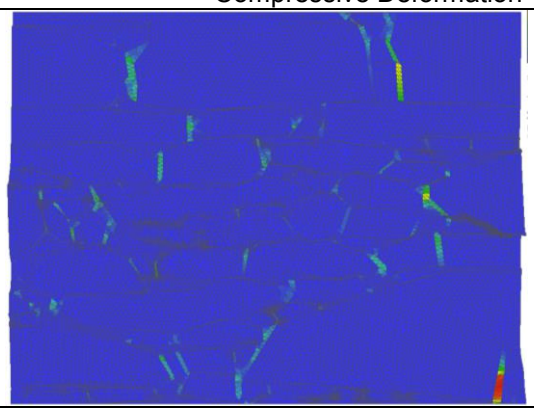

Matrix w/ Stone Range (m²):	0.002
Meso-scale Model #:	1

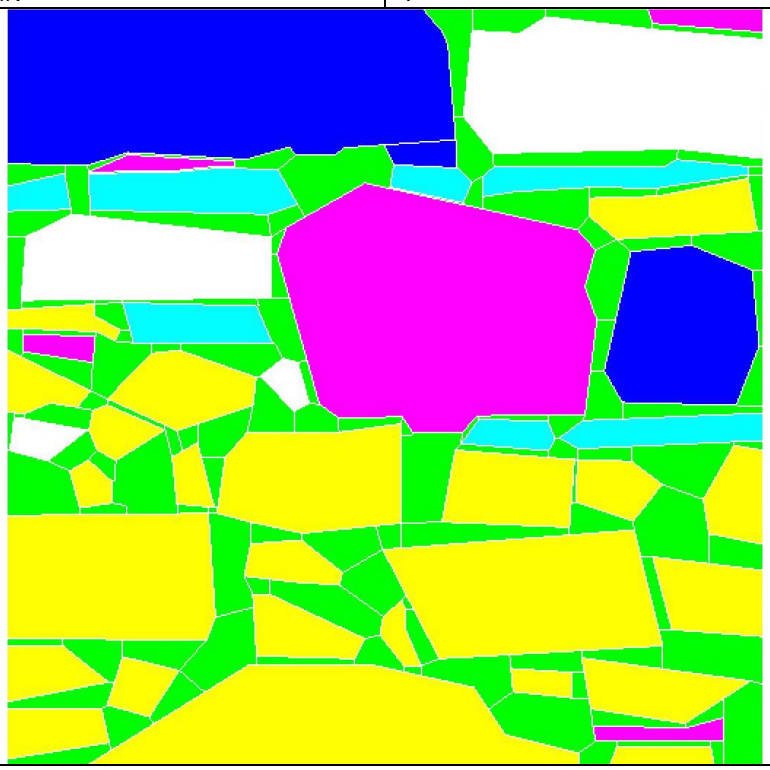

Compression Test – Peak = Step 37

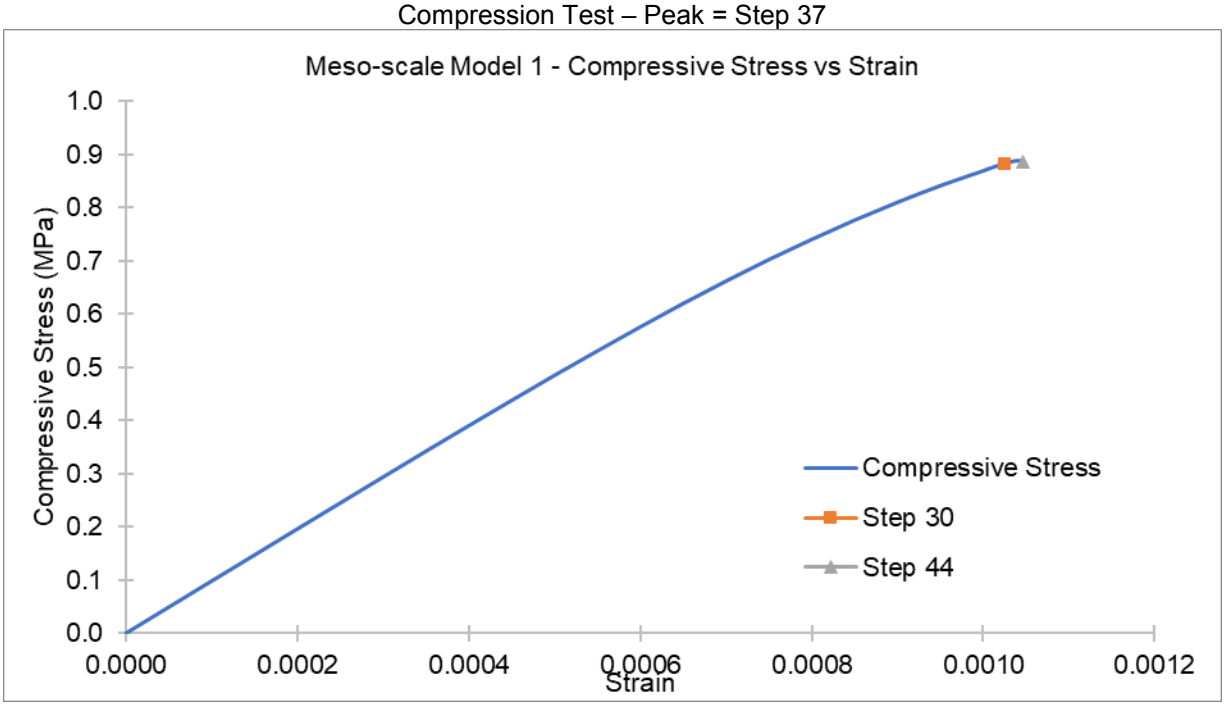

Crack Width

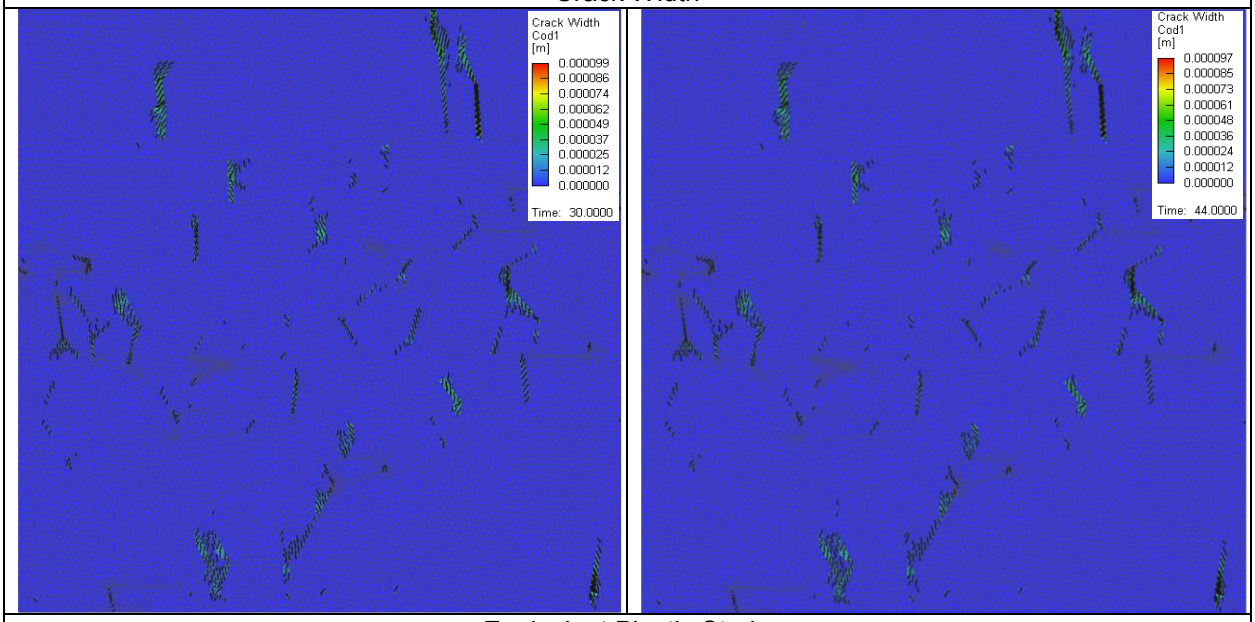

Equivalent Plastic Strain

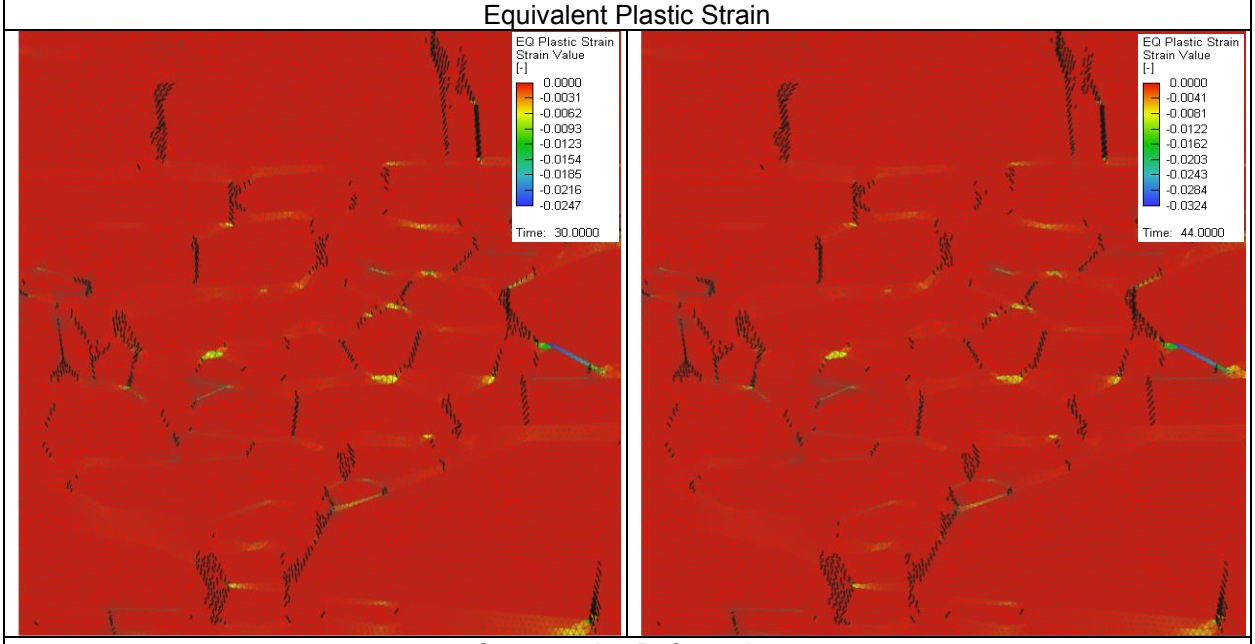

Compressive Deformation

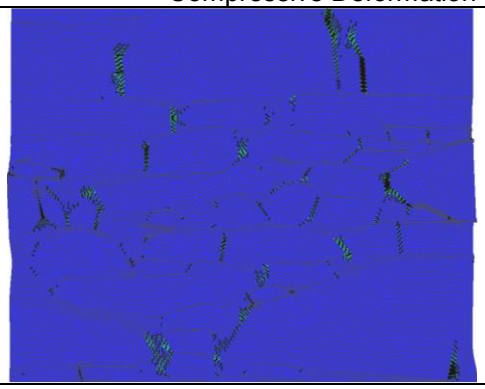

Matrix w/ Stone Range (m²):	0.001
Meso-scale Model #:	2

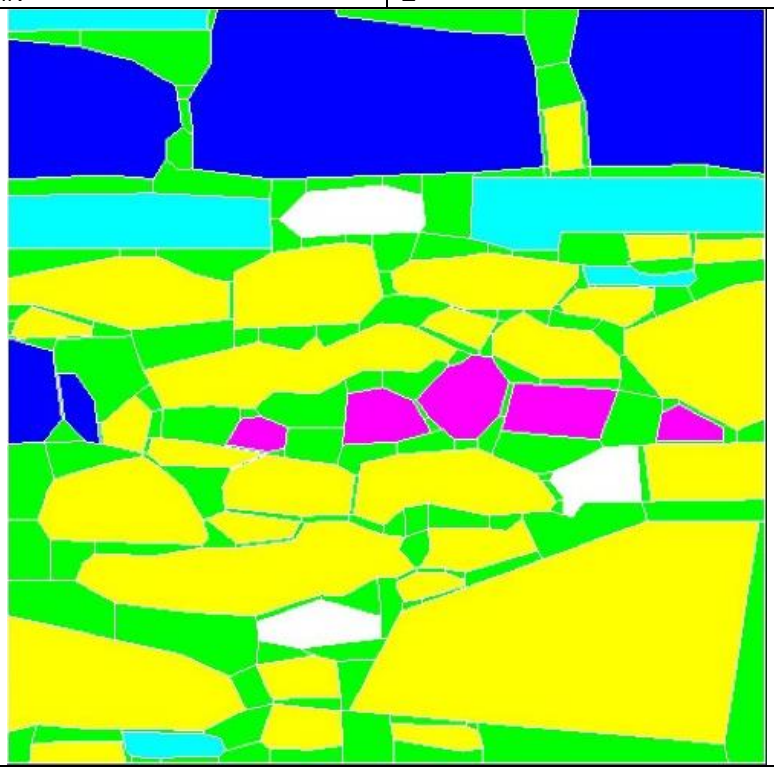

Compression Test – Peak = Step 25

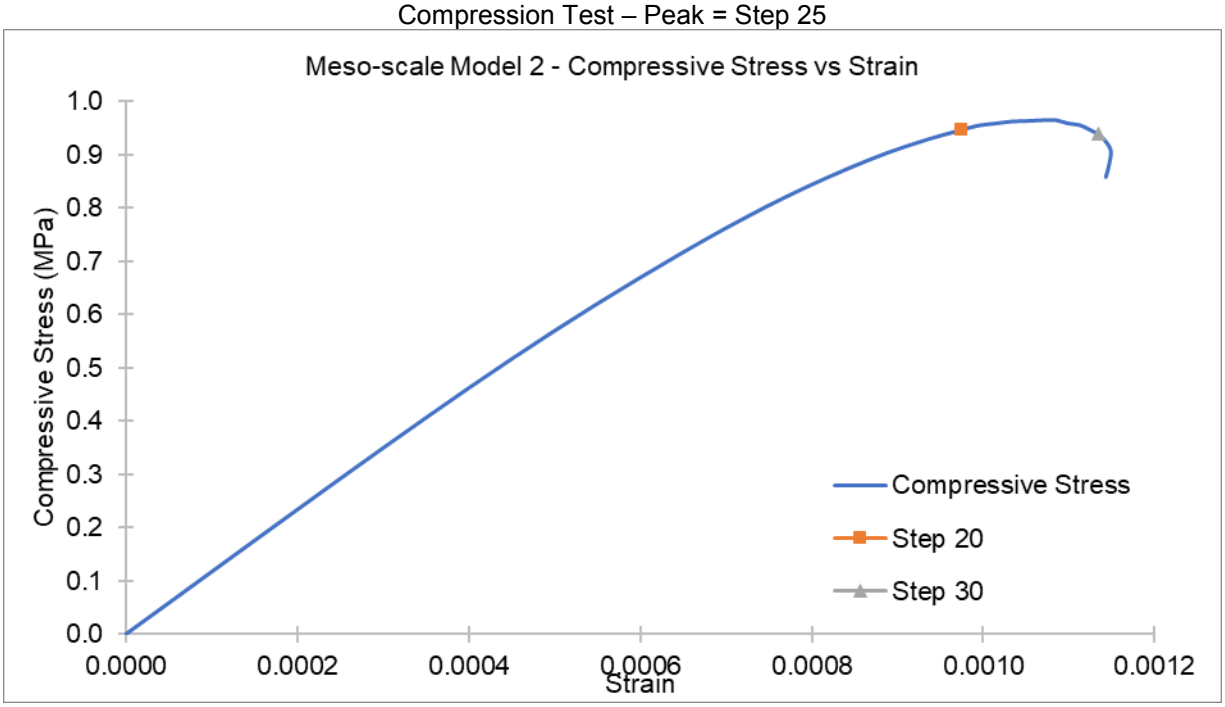

Crack Width

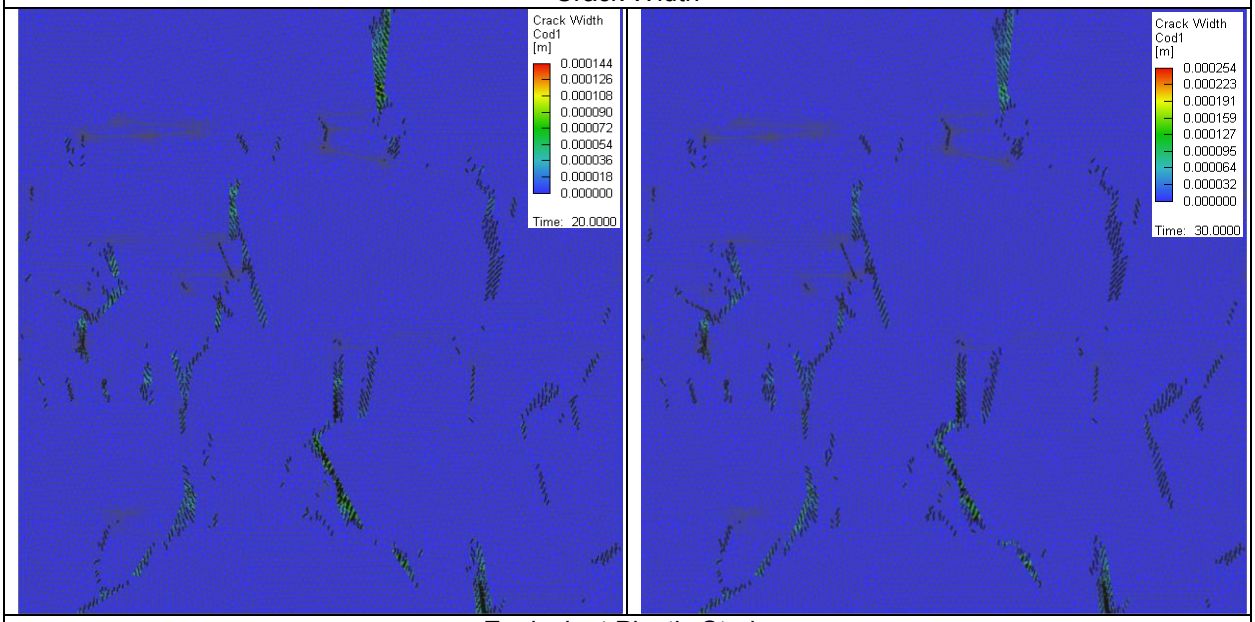

Equivalent Plastic Strain

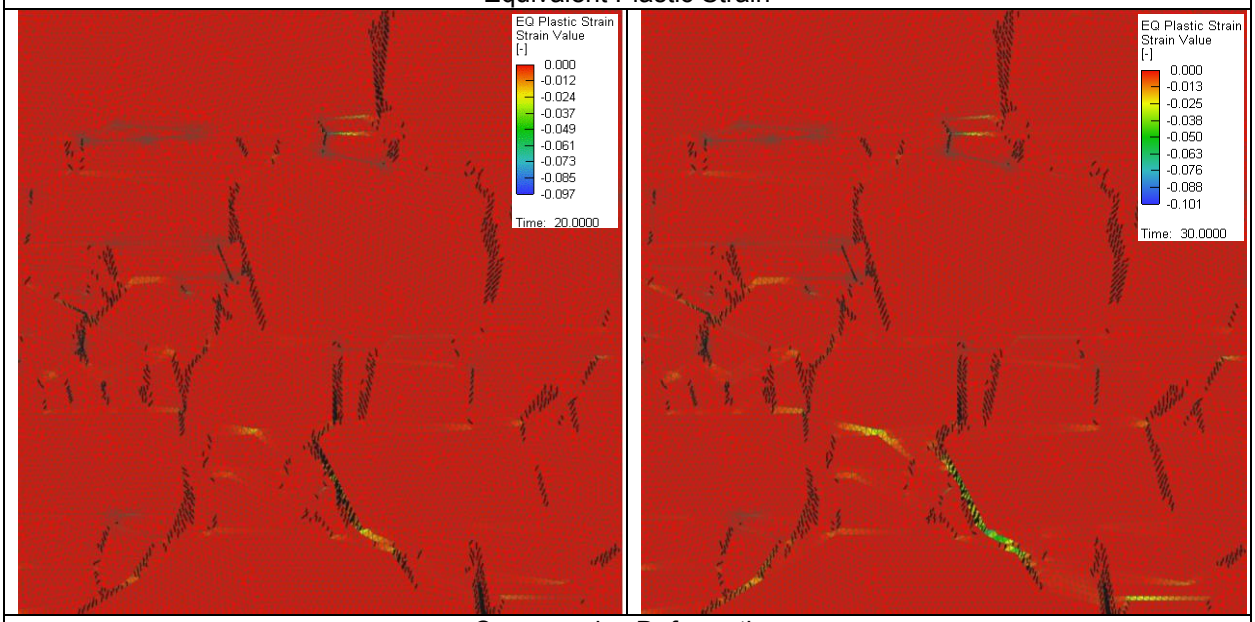

Compressive Deformation

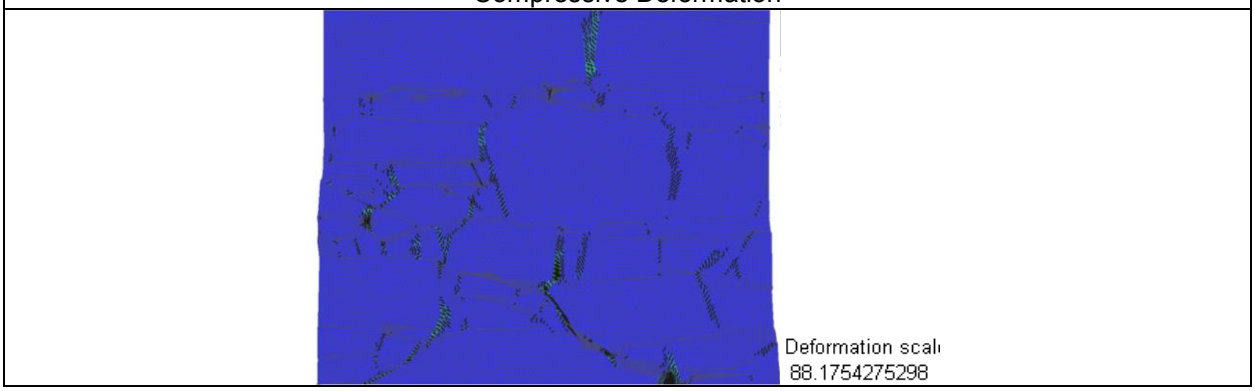

Matrix w/ Stone Range (m²):	0.002
Meso-scale Model #:	2

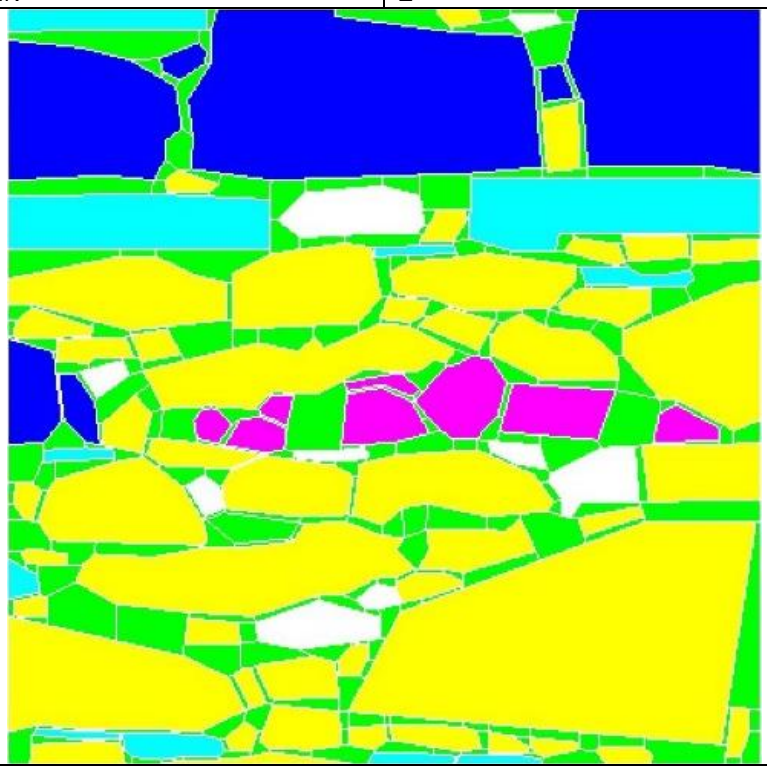

Compression Test – Peak = Step 27

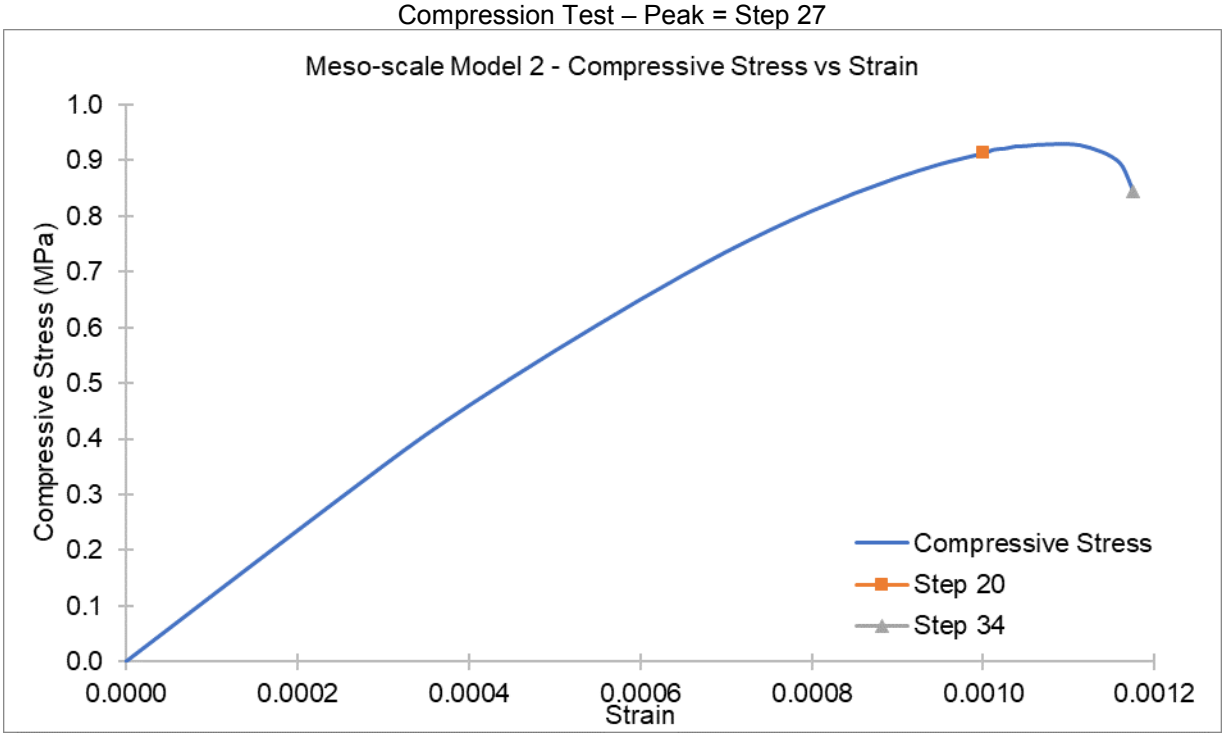

Crack Width

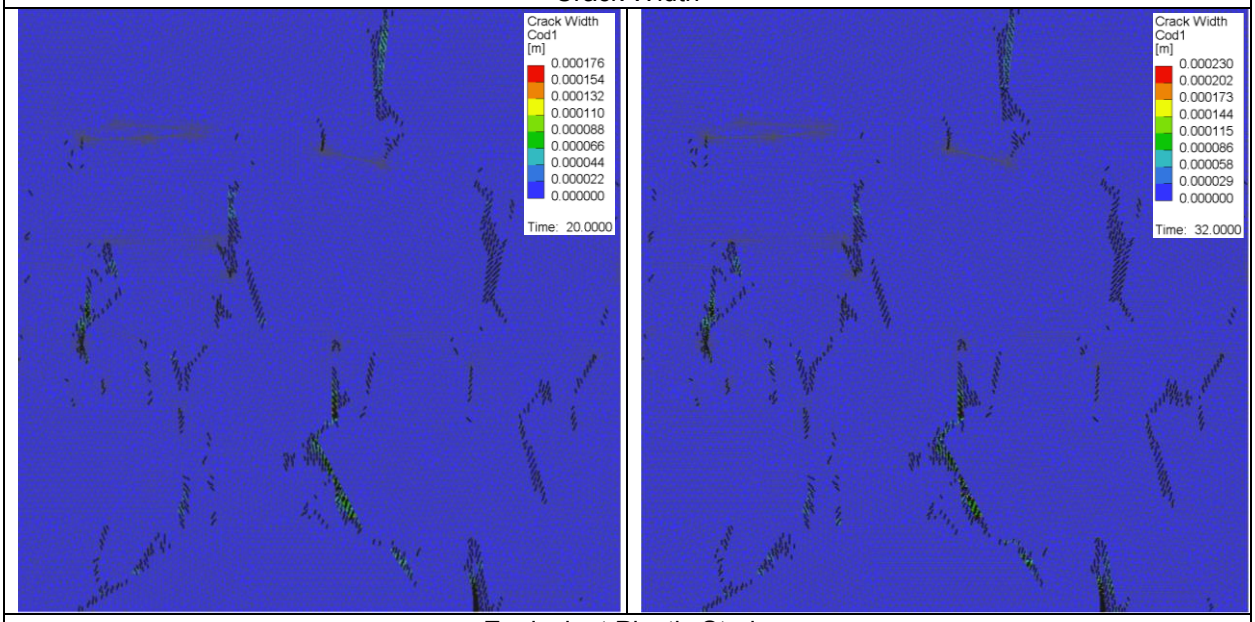

Equivalent Plastic Strain

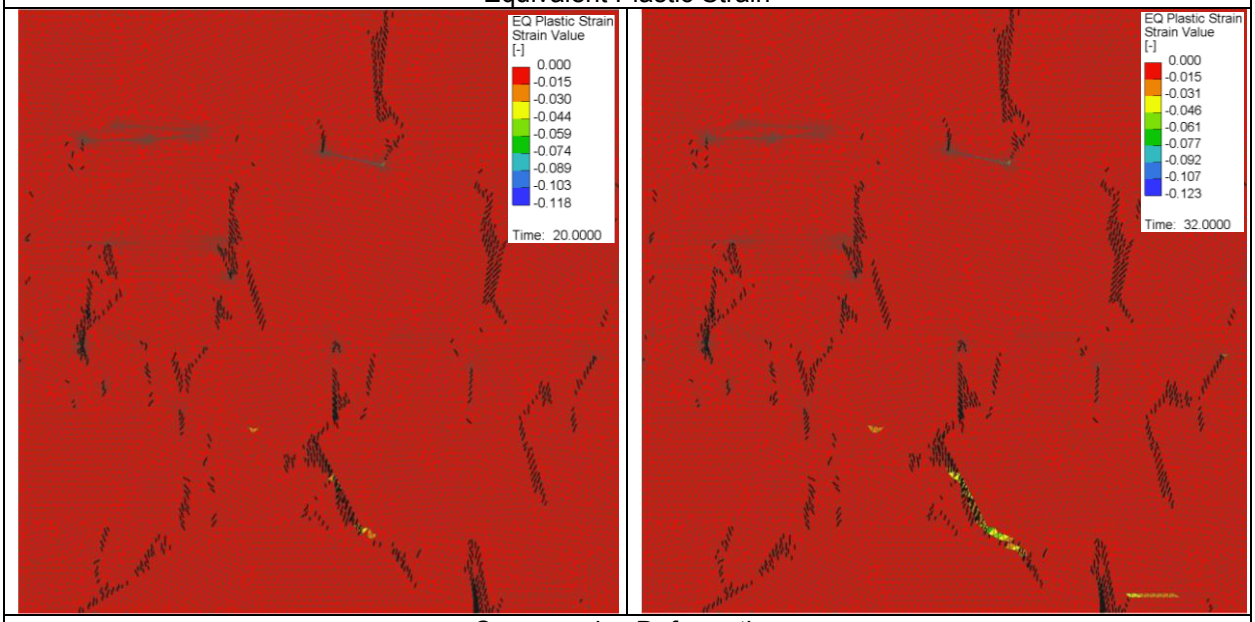

Compressive Deformation

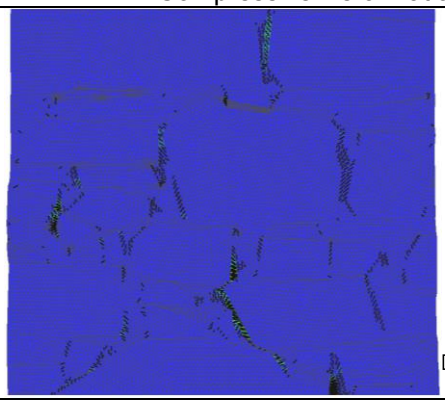

Deformation scale:
80.

Matrix w/ Stone Range (m²):	0.001
Meso-scale Model #:	3

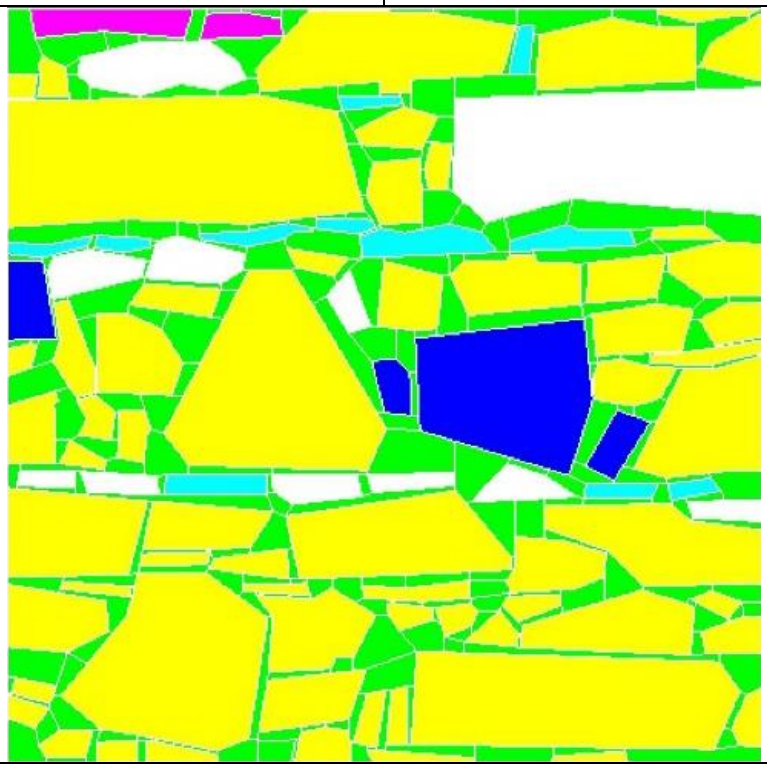

Compression Test – Peak = Step 28

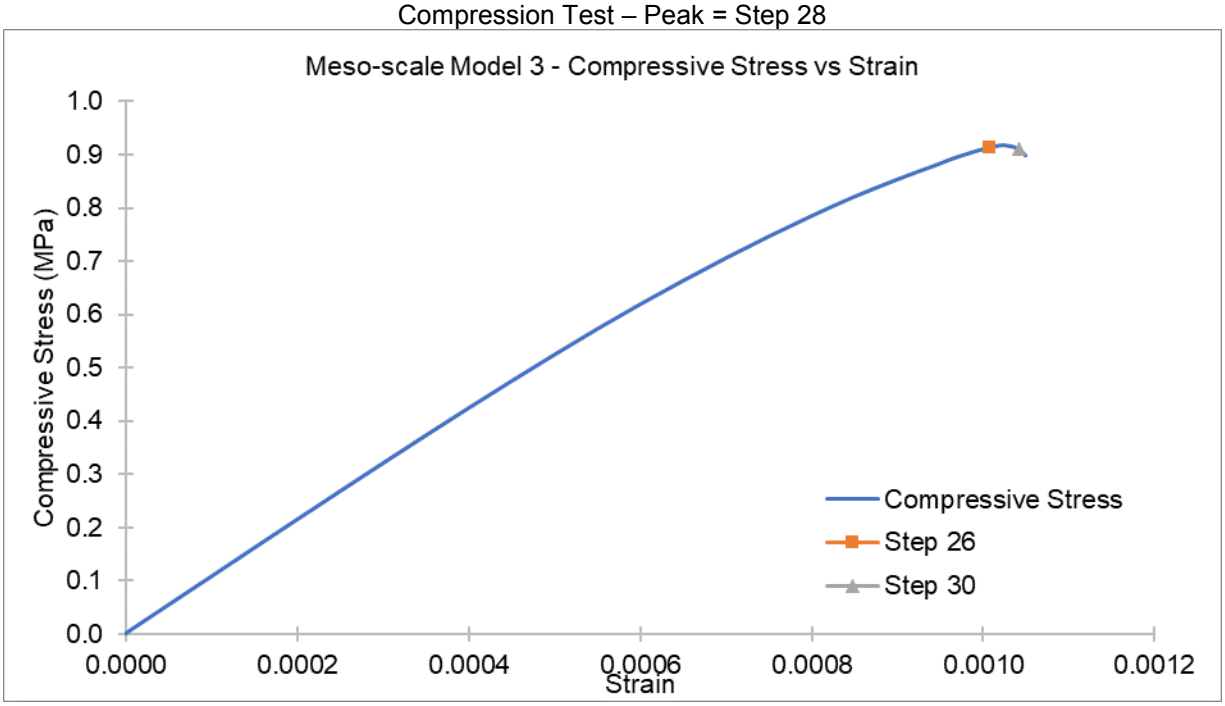

Crack Width

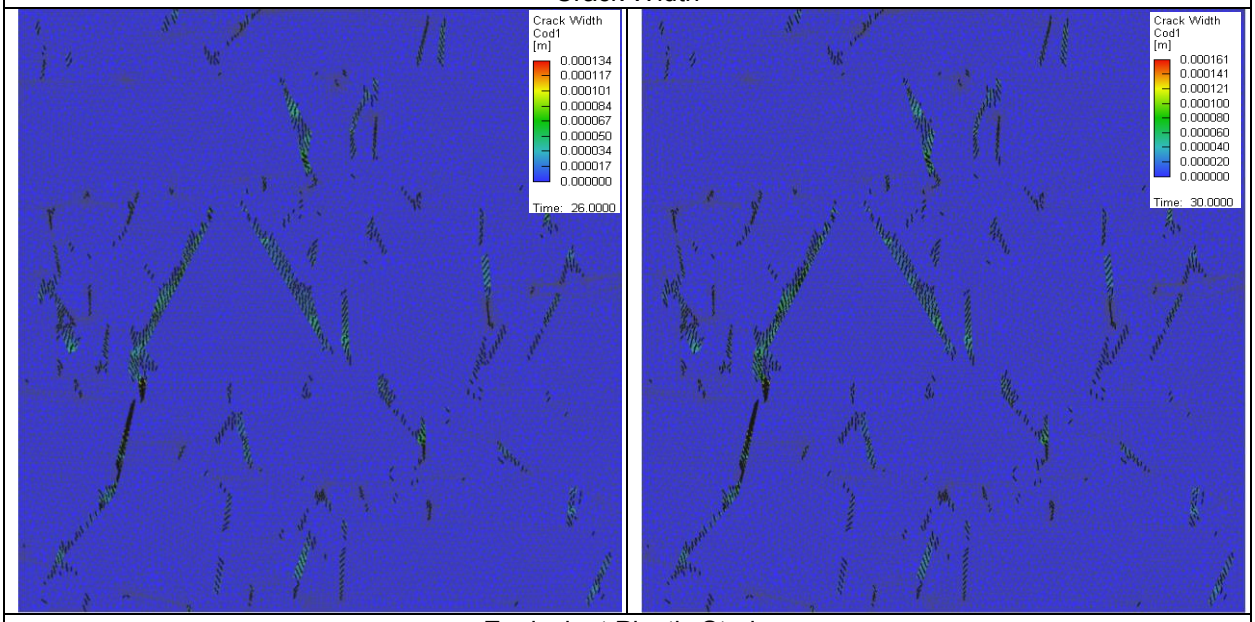

Equivalent Plastic Strain

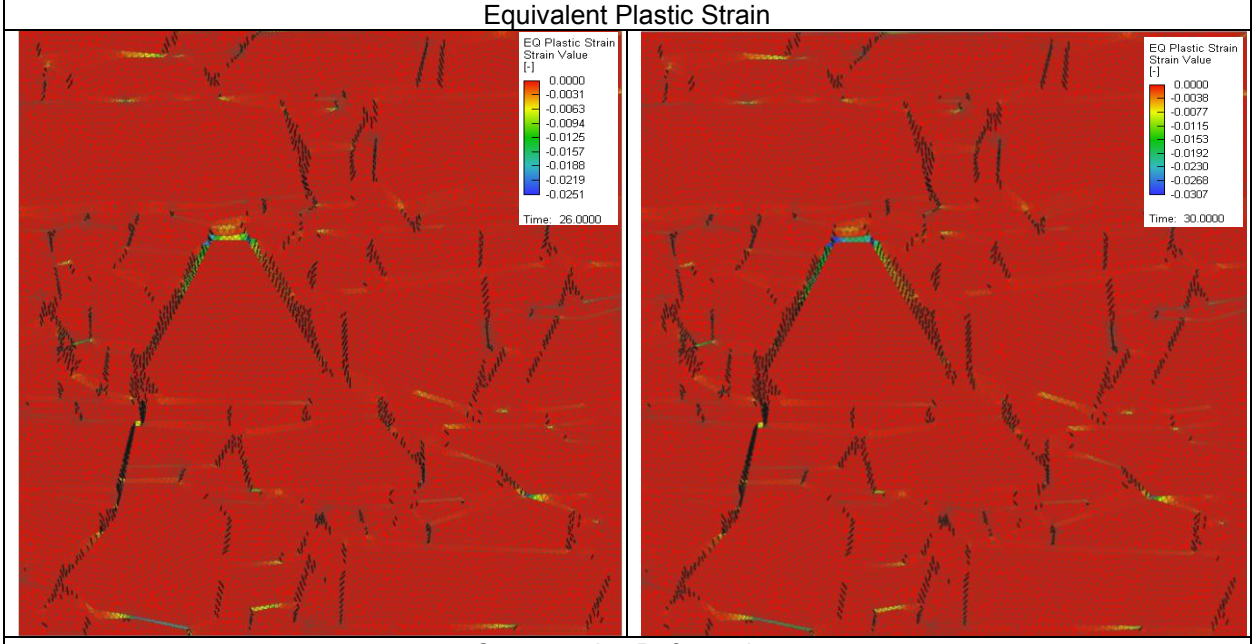

Compressive Deformation

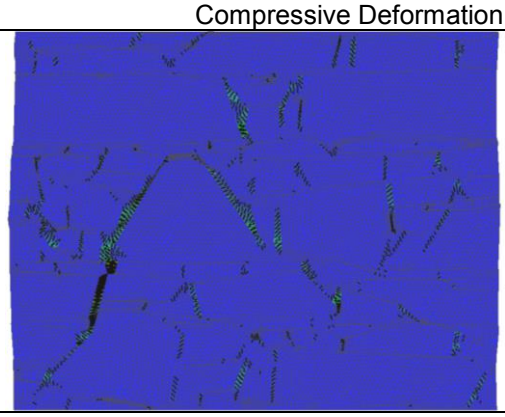

Matrix w/ Stone Range (m²):	0.002
Meso-scale Model #:	3

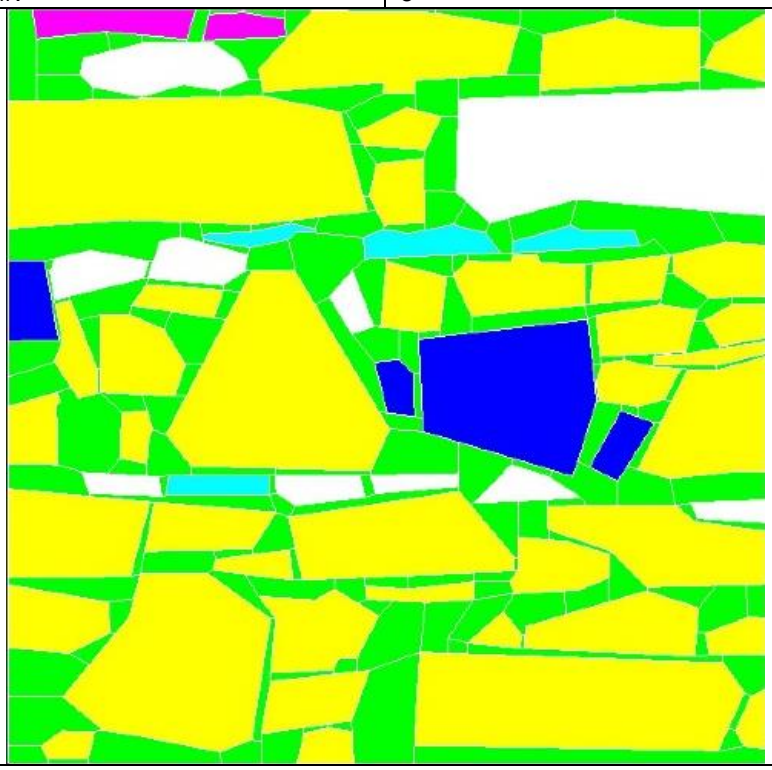

Compression Test – Peak = Step 64

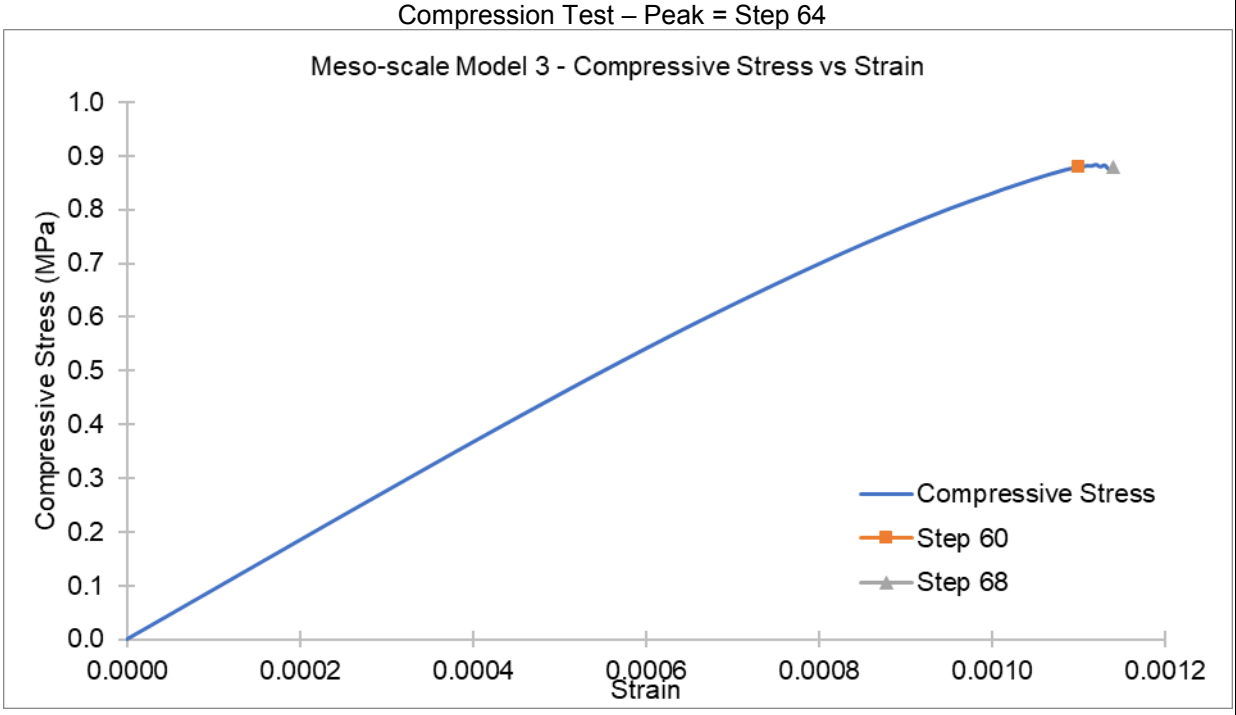

Crack Width

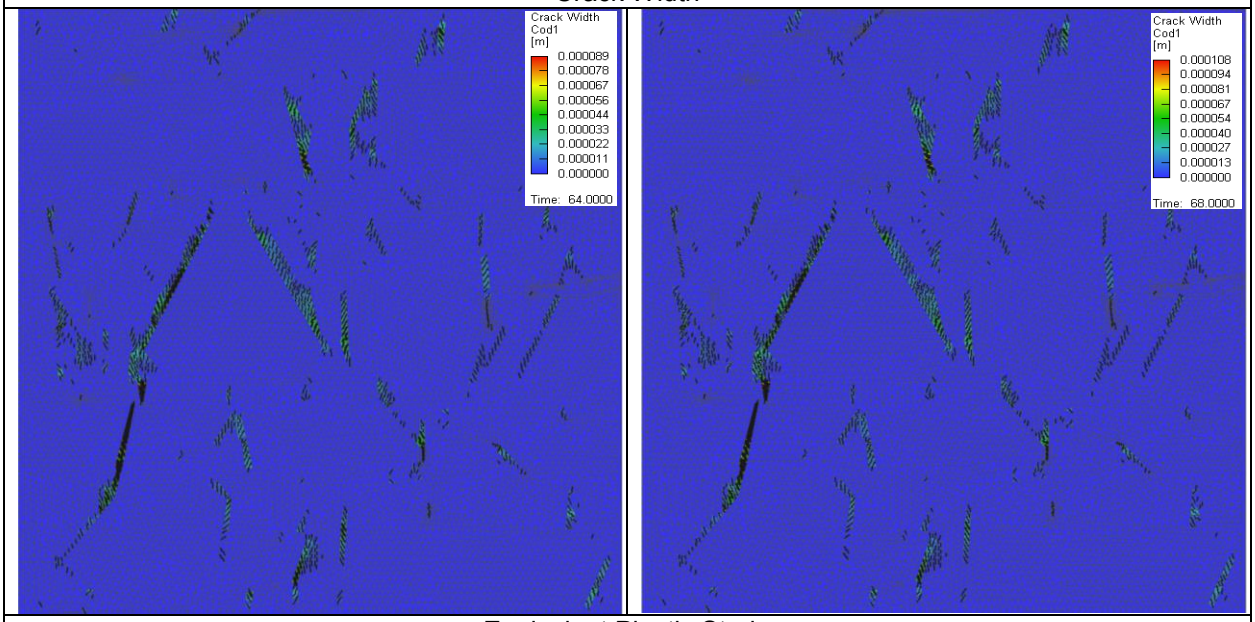

Equivalent Plastic Strain

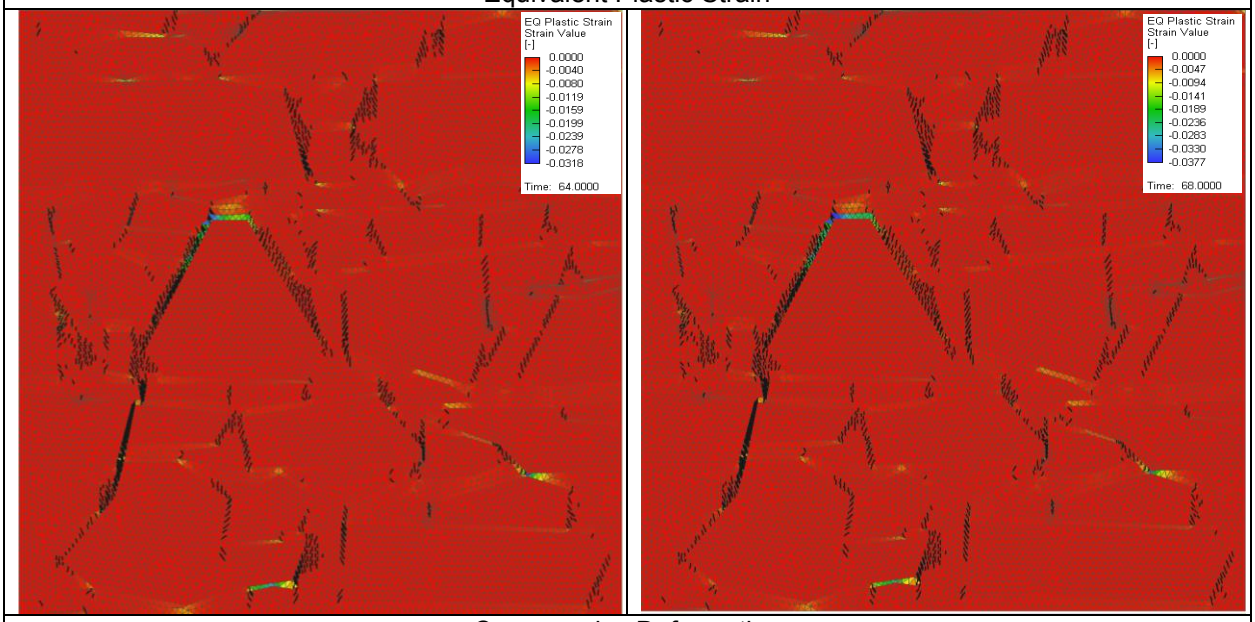

Compressive Deformation

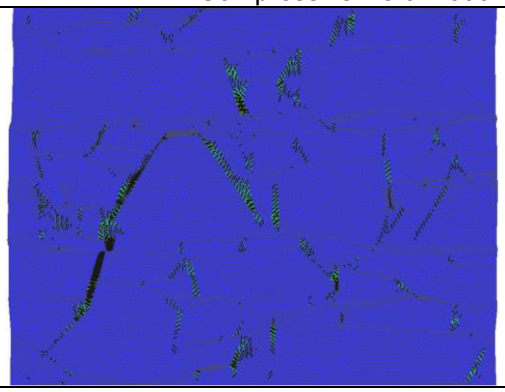

Appendix E: Random Field Simulations

Matrix w/ Stone Range (m²):	0.001
Meso-scale Model #:	2
Random Field Simulation	2
f_c	E
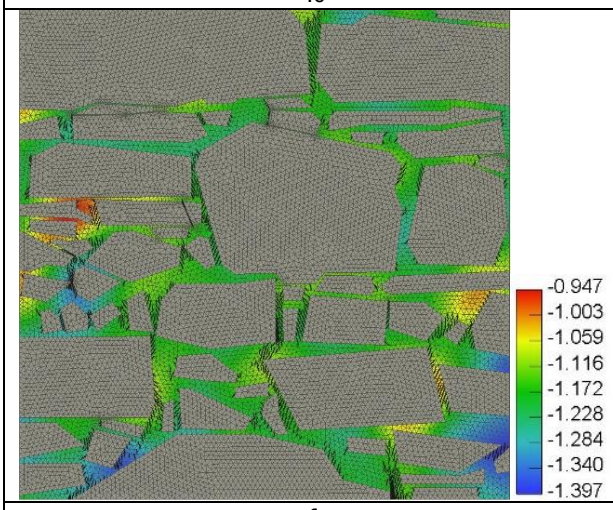	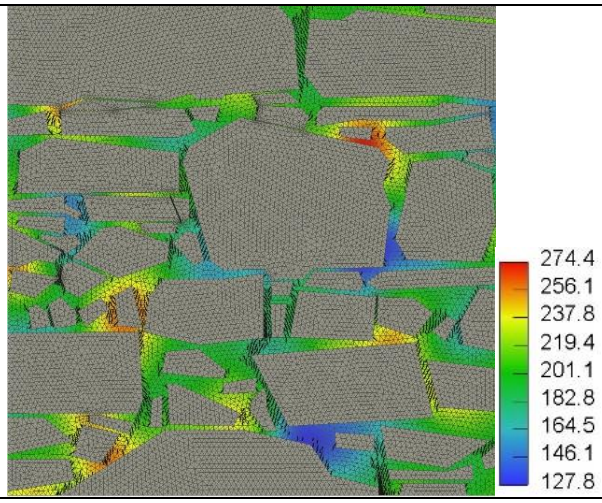
f_t	Gf
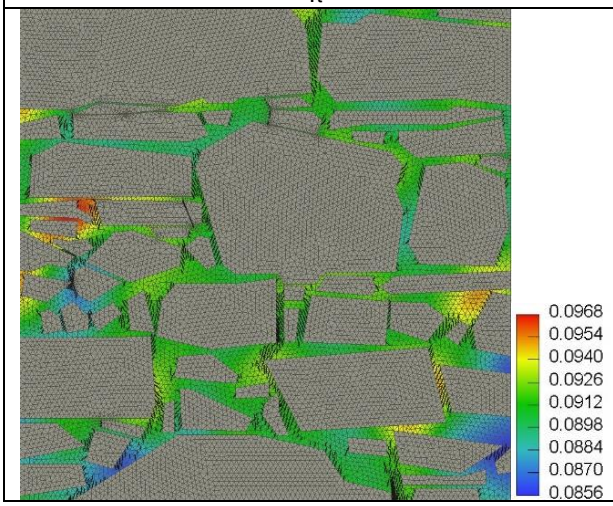	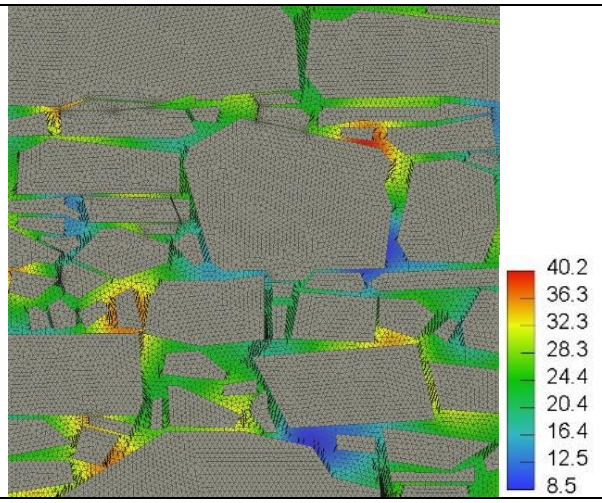

Matrix w/ Stone Range (m²):	0.001
Meso-scale Model #:	2
Random Field Simulation	3
f_c	E
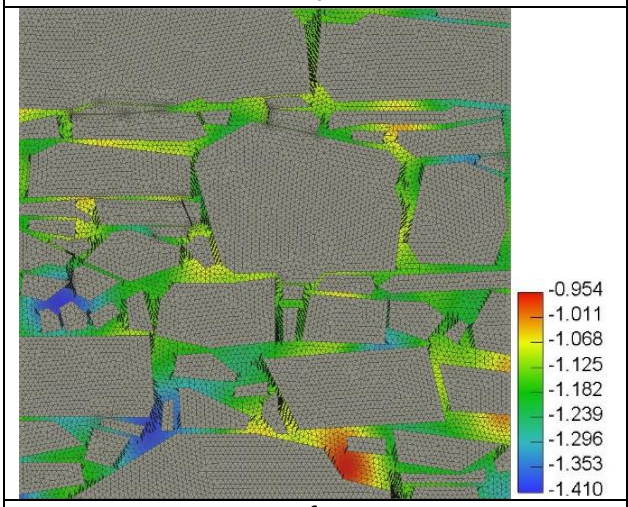	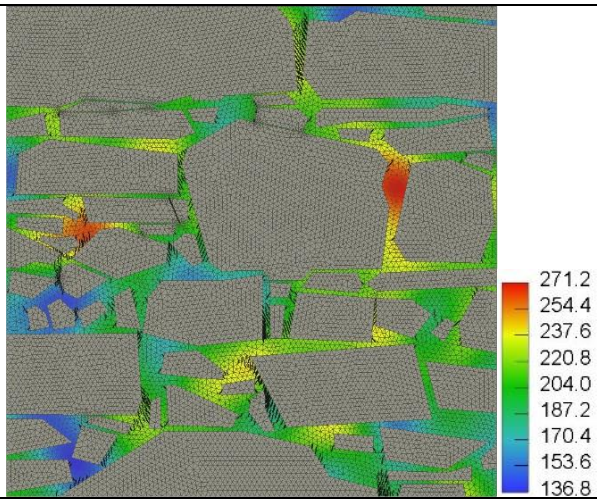
f_t	G_f
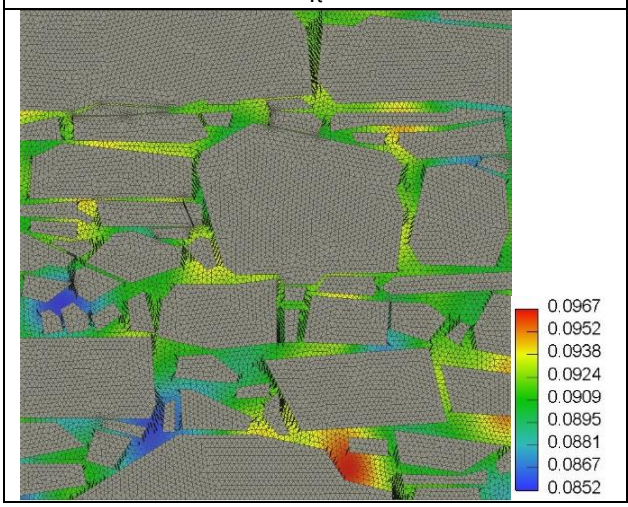	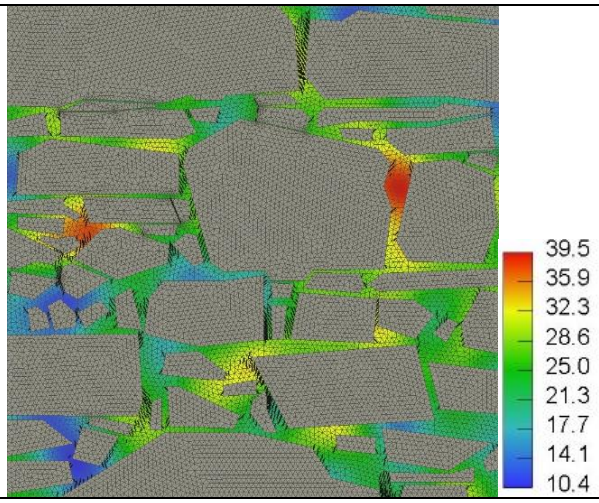

Matrix w/ Stone Range (m²):	0.002
Meso-scale Model #:	2
Random Field Simulation	2
f_c	E
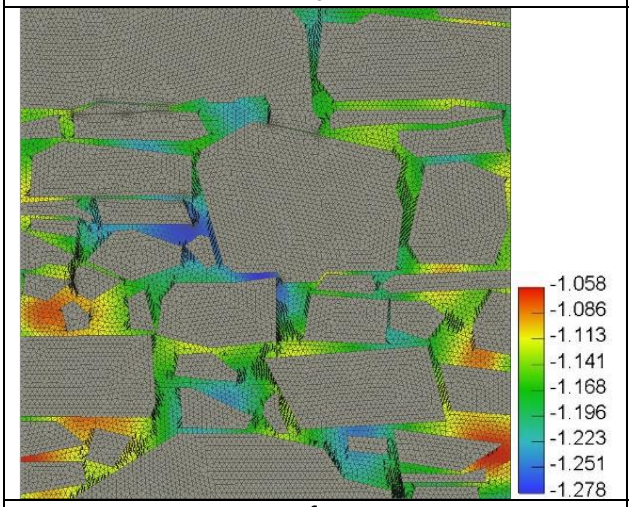	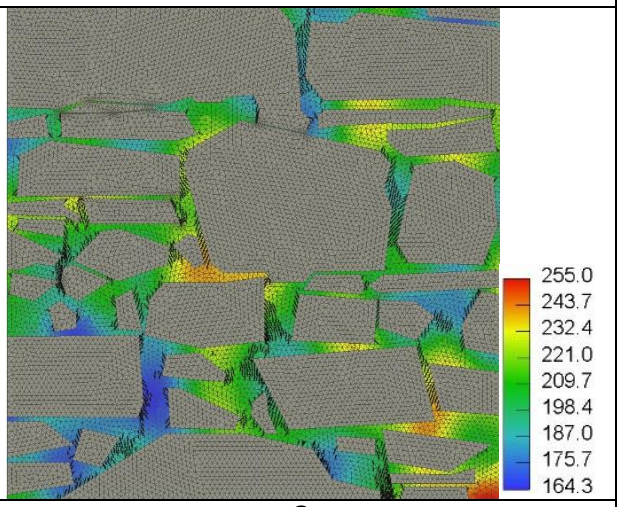
f_t	G_f
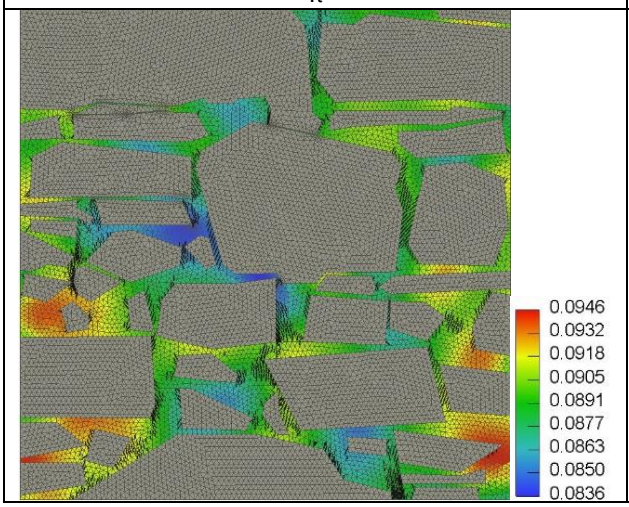	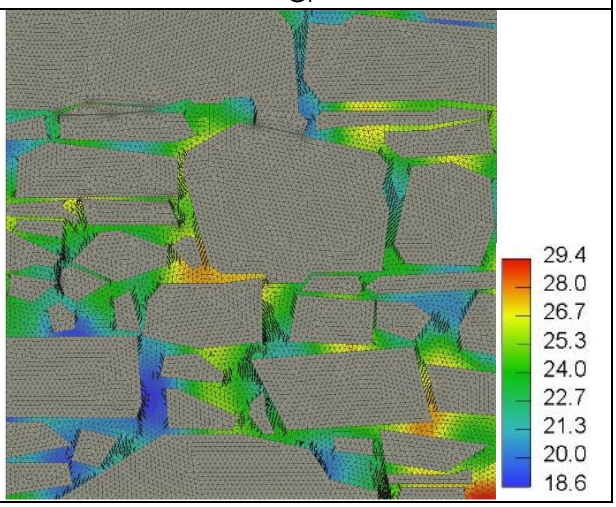

Matrix w/ Stone Range (m²):	0.002
Meso-scale Model #:	2
Random Field Simulation	3

f_c	E
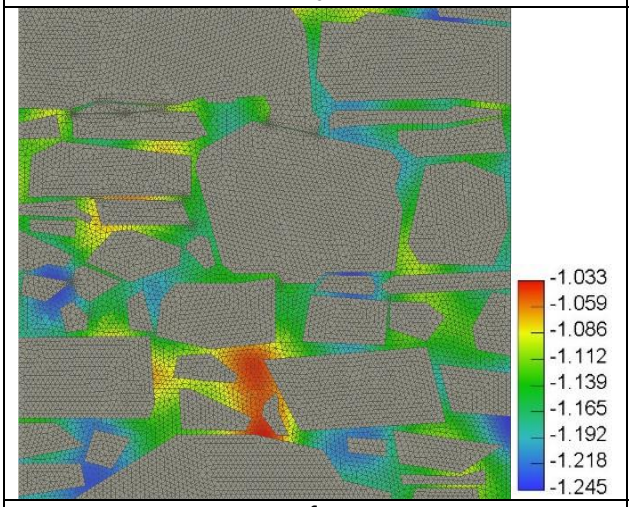	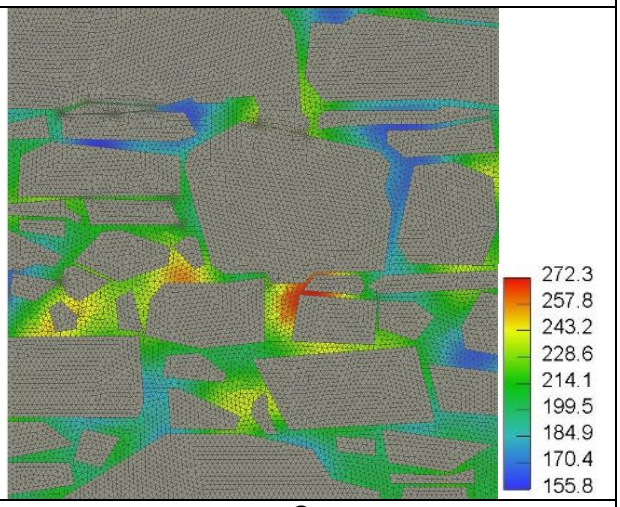
f_t	G_f